UNIVERSITY OF TRENTO

Doctoral School in Civil, Environmental and Mechanical Engineering

Curriculum 3. Modelling and Simulation

Nicola Bordignon

Bifurcations and instability in non-linear elastic solids with interfaces

2018- Doctoral thesis

University of Trento

Department of Civil, Environmental and Mechanical Engineering

PhD in Civil, Environmental and Mechanical Engineering

Nicola Bordignon

Bifurcations and instability in non-linear elastic solids with interfaces

Advisors:

Prof. Davide Bigoni - University of Trento

Prof. Andrea Piccolroaz - University of Trento

Academic Year 2017/2018

First revision: 31/01/2018
Referee:
Prof. Dennis M. Kochmann - ETH Zurich
Prof. Alberto Salvadori - UNIBS

Once, a person told me...
"It's worth it, the World is flattening..."
..he was right...

Acknowledgments

This thesis collects the reaserch I carried out during the three years as Ph.D. student in Civil, Environmental and Mechanical Engineering at the University of Trento.
I would like to thank my advisors, Prof. Davide Bigoni and Prof. Andrea Piccolroaz, for theirs suggestions and remarks regarding the topics of my thesis and especially for the constructive discussions on subjects not strictly related to the university area. I would like to thank Prof. Stanislaw Stupkiewicz for the help in the development of numerical applications. I am indebted to Dr Diego Misseroni for his cooperation during the experimental phases in the Instability Lab of the University of Trento.

Trento, April 2018

Nicola Bordignon

Abstract

The study of local and global instability and bifurcation phenomena is crucial for many engineering applications in the field of solid mechanics. In particular, interfaces within solid bodies are of great importance in the bifurcation analysis, as they constitute localized zones in which discontinuities or jumps in displacement, strain or stress may occur. Different instability phenomena, heavily conditioned by the presence of interfaces, were analyzed in the present thesis.

The first phenomenon that has been considered is the propagation of a shear band, which is a localized shear deformation developing in a ductile material. This shear band, assumed to be already present inside of a ductile matrix material (obeying von Mises plasticity with linear hardening), is modelled as a discontinuity interface following two different approaches.

In the first approach, the conditions describing the behavior of a layer of material in which localized strain develop are introduced and implemented in a finite element computer code. A shear deformation is simulated by imposing appropriate displacement conditions on the boundaries of the matrix material, in which the shear band is present and modelled through an imperfect interface, having null thickness.

The second approach is based on a perturbative technique, developed for a J_2-deformation theory material, in which the shear band is modeled as the emergence of a discontinuity surface for displacements at a certain stage of a uniform deformation process, restricted to plane strain conditions.

Both the approaches concur in showing that shear bands (differently from cracks) propagate rectilinearly under shear loading and that a strong stress concentration is expected to be present at the tip of the shear band, two key features in the understanding of failure mechanisms of ductile

materials [results of this study have been reported in (Bordignon et al. 2015)].

The second type of interface analyzed in the present thesis is a perfectly frictionless sliding interface, subject to large deformations and assumed to be present within a uniformly strained nonlinear elastic solid. This type of interface may model lubricated sliding contact between soft solids, a topic of interest in biomechanics and for the design of small-scale engineering devices.

The analyzed problem is posed as follows. Two elastic nonlinear solids are considered jointed through a frictionless and bilateral surface, so that continuity of the normal component of the Cauchy traction holds across the surface, but the tangential component is null. Moreover, the displacement can develop only in a way that the bodies in contact do neither detach, nor overlap. Surprisingly, this finite strain problem has not been correctly formulated until now, so that this formulation has been developed in the thesis. The incremental equations are shown to be non-trivial and different from previously (and erroneously) employed conditions. In particular, an exclusion condition for bifurcation is derived to show that previous formulations based on frictionless contact or 'spring-type' interfacial conditions are not able to predict bifurcations in tension, while experiments (one of which, ad hoc designed, is reported) show that these bifurcations are a reality and can be predicted when the correct sliding interface model is used. Therefore, the presented approach introduces a methodology for the determination of bifurcations and instabilities occurring during lubricated sliding between soft bodies in contact [results of this study have been reported in (Bigoni et al. 2018)].

Funding The author gratefully acknowledges financial support from the ERC Advanced Grant 'Instabilities and nonlocal multiscale modelling of materials' ERC-2013-ADG-340561-INSTABILITIES.

Articles

The results reported in the present research thesis have been summarized in the following papers:

- Bordignon N, Piccolroaz A, Dal Corso F and Bigoni D (2015) Strain localization and shear band propagation in ductile materials. *Frontiers in Materials* **2**:22. doi: 10.3389/fmats.2015.00022

- Bigoni, D., Bordignon, N., Piccolroaz, A., Stupkiewicz, S. (2018) Bifurcation of elastic solids with sliding interfaces. *Proceedings of the Royal Society of London A: Mathematical, Physical and Engineering Sciences*, **474**, 20170681. doi: 10.1098/rspa.2017.0681 [Open access]

Contents

List of Figures

List of Tables

Chapter 1

Mechanics of solids

1.1 Introduction

The basic concepts related to the solid body are introduced. In particular, the kinematics, the stress and strain concepts are provided with the theories and the rules that govern the changes of field quantities during the motion of the solid body from the reference configuration to the current configuration underlining the difference between the spatial and the material fields.

1.2 Kinematics

The kinematics of the bodies describe and study the configurations that the bodies occupy during a motion in the three dimensional Euclidean point space. A body is treated as a closed set of points occupying a regular region $\boldsymbol{B}$, called 'current' configuration, of the three dimensional Euclidean point space. The displacement of the points in the $\boldsymbol{B}$ region, indicated with vector $\boldsymbol{u}$, may be measured only with respect to reference configuration $\boldsymbol{B}_0$. As reported in Bigoni (2012) "*the choise of the reference configuration is arbitrary, so even a configuration which has never been occupied by the body can be chosen as reference. Obviously, the resulting description of all fields must be independent of this choise*". Points $\boldsymbol{x}$ ($\boldsymbol{x}_0$) defined in reference or current configurations are called 'spatial'(material).

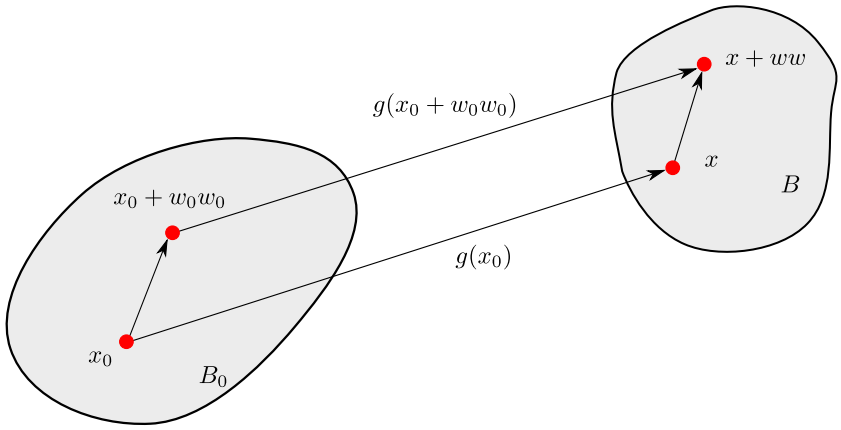

Figure 1.1: Deformation of a general body and in particular, deformation of an embedded oriented line element from reference configuration $\boldsymbol{B}_0$ to the current configuration $\boldsymbol{B}$.

The displacement is defined as

$$\boldsymbol{u} = \boldsymbol{x} - \boldsymbol{x}_0 \tag{1.1}$$

or, using the function $\boldsymbol{g}$ that represent a bijection mapping relating material points to spatial points

$$\boldsymbol{u} = \boldsymbol{g}(\boldsymbol{x}_0) - \boldsymbol{x}_0. \tag{1.2}$$

Considering two material points, $\boldsymbol{x}_0$ and $\boldsymbol{x}_0 + w_0\boldsymbol{w}_0$, as shown in Fig. 1.1 in which $\boldsymbol{w}_0$ is a unit vector and w_0 is a simple scalar multiplier, in spatial configuration they are mapped forward to

$$\boldsymbol{x} = \boldsymbol{g}(\boldsymbol{x}_0) \tag{1.3}$$

and

$$\boldsymbol{x} + w\boldsymbol{w} = \boldsymbol{g}(\boldsymbol{x}_0 + w_0\boldsymbol{w}_0) \tag{1.4}$$

Taking the Taylor series expansions of the function $\boldsymbol{g}$, and its inverse $\boldsymbol{g}^-1$, around $\boldsymbol{x}_0$ and $\boldsymbol{x}$ yield

$$w\boldsymbol{w} = \boldsymbol{g}(\boldsymbol{x}_0 + w_0\boldsymbol{w}_0) - \boldsymbol{g}(\boldsymbol{x}_0) = \boldsymbol{F}(w_0\boldsymbol{w}_0) + \boldsymbol{O}(w_0^2), \tag{1.5}$$

$$w_0\boldsymbol{w}_0 = \boldsymbol{g}^{-1}(\boldsymbol{x} + w\boldsymbol{w}) - \boldsymbol{g}^{-1}(\boldsymbol{x}) = \boldsymbol{F}^{-1}(w\boldsymbol{w}) + \boldsymbol{O}(w^2), \tag{1.6}$$

where $\boldsymbol{F}$ is the deformation gradient and $\boldsymbol{F}^{-1}$ its inverse. In other words, $\boldsymbol{F}$ represents a gradient of a material field, whereas $\boldsymbol{F}^{-1}$ is the gradient of a spatial field

$$\boldsymbol{F} = \frac{\partial \boldsymbol{g}(\boldsymbol{x}_0)}{\partial \boldsymbol{x}_0} \qquad \boldsymbol{F}^{-1} = \frac{\partial \boldsymbol{g}^{-1}(\boldsymbol{x})}{\partial \boldsymbol{x}}. \tag{1.7}$$

1.2.1 Trasformation of oriented line elements

It is clear that the gradient $\boldsymbol{F}$ transforms the embedded material oriented line element into a corresponding embedded spatial oriented line element and viceversa. Immediatly, the transformation of oriented liene elements can be derived in the modulus and in the orientation as follow

$$\lambda(\boldsymbol{x}_0, \boldsymbol{w}_0) = |\boldsymbol{F}\boldsymbol{w}_0| \qquad \frac{1}{\lambda(\boldsymbol{x}, \boldsymbol{w})} = |\boldsymbol{F}^{-1}\boldsymbol{w}|, \tag{1.8}$$

$$\boldsymbol{w}_0 = \lambda(\boldsymbol{x}, \boldsymbol{w})\boldsymbol{F}^{-1}\boldsymbol{w} \qquad \boldsymbol{w} = \frac{\boldsymbol{F}\boldsymbol{w}_0}{\lambda(\boldsymbol{x}_0, \boldsymbol{w}_0)}, \tag{1.9}$$

where λ represents the stretch at the material or spatial point relative to the material or spatial direction.

1.2.2 Trasformation of oriented area elements

An element area A_0 with normal n_0 and described by the two vectors $\boldsymbol{v}_0$ and $\boldsymbol{w}_0$ can be expressed in the material configuration

$$A_0\boldsymbol{n}_0 = \boldsymbol{v}_0 \times \boldsymbol{w}_0. \tag{1.10}$$

Applying the gradient of the material field the area element is transformed in the spatial configuration as

$$A\boldsymbol{n} = \boldsymbol{F}\boldsymbol{v}_0 \times \boldsymbol{F}\boldsymbol{w}_0. \tag{1.11}$$

At this point, introducing the property related to the tensors and vectors the Nanson's rule of area transformation is derived

$$A\boldsymbol{n} = A_0 J \boldsymbol{F}^{-T}\boldsymbol{n}_0 \tag{1.12}$$

where $J = det\boldsymbol{F}$. Furthermore, Eq. (1.12) provides the transformation laws of unit normal embedded surfaces and area elements shown in Fig. 1.2

$$\boldsymbol{n} = \frac{\boldsymbol{F}^{-T}\boldsymbol{n}_0}{|\boldsymbol{F}^{-T}\boldsymbol{n}_0|}, \qquad \boldsymbol{n}_0 = \frac{\boldsymbol{F}^{T}\boldsymbol{n}}{|\boldsymbol{F}^{T}\boldsymbol{n}|} \tag{1.13}$$

and

$$A = J|\boldsymbol{F}^{-T}\boldsymbol{n}_0|A_0, \qquad A_0 = J^{-1}|\boldsymbol{F}^{T}\boldsymbol{n}|A. \tag{1.14}$$

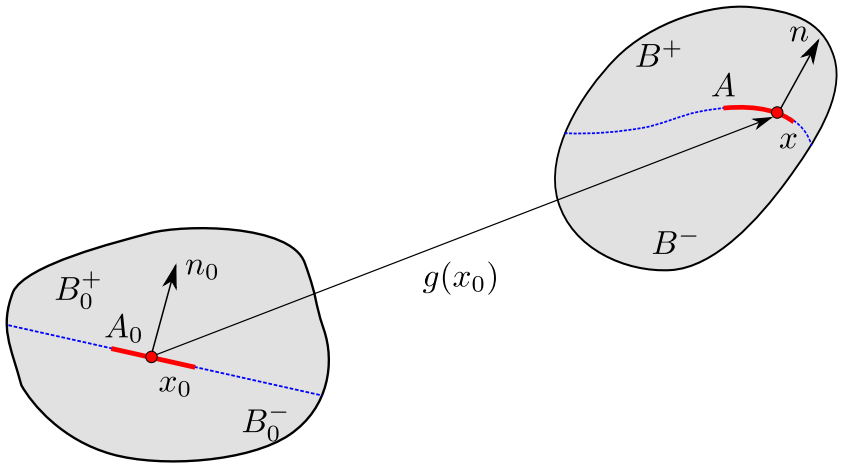

Figure 1.2: Deformation of a general area element A (straight red line) with normal $\boldsymbol{n}_0$ to a general surface (dashed blue line) from reference configuration $\boldsymbol{B}_0^{\pm}$ to the current configuration $\boldsymbol{B}^{\pm}$.

1.2.3 Trasformation of volume elements

Volume element V_0 at a generic material point is transformed by the deformation as

$$V_0 = \boldsymbol{t}_0 \cdot \boldsymbol{v}_0 \times \boldsymbol{w}_0 \rightarrow \boldsymbol{F} \rightarrow V = \boldsymbol{F}\boldsymbol{t}_0 \cdot \boldsymbol{F}\boldsymbol{v}_0 \times \boldsymbol{F}\boldsymbol{w}_0 \tag{1.15}$$

in which the vectors $\boldsymbol{t}_0$,$\boldsymbol{v}_0$ and $\boldsymbol{w}_0$ describe the volume element in the reference configuration $\boldsymbol{B}_0$.

1.3 Stress and motion in finite strain

1.3.1 Stress

The concepts of stress are introduced to complete the treatment of physical quantities that describe the mechanics of a generic solid body or part of it, called P. In current configuration, the body part P and external

forces σ interact each other to achive an equilibrium state. These external forces may act on surface Σ or at internal body points $\boldsymbol{b}$.

This interaction leads to the creation of a contact forces distribution inside the body part P, generating a stress field $\boldsymbol{s}$. In detail, assuming the so-called Cauchy hypothesis, traction $\boldsymbol{s}$ depends only on the position $\boldsymbol{x}$ and on the unit normal $\boldsymbol{n}$ to the surface inside P at $\boldsymbol{x}$ in the spatial configuration, namely

$$\boldsymbol{s} = \boldsymbol{s}(\boldsymbol{x}, \boldsymbol{n}). \tag{1.16}$$

At this point, not taking into account the inertial body force but only the volume forces $\boldsymbol{b}$, the balance laws

$$\int_{\partial P} \boldsymbol{s} + \int_{\partial P} \boldsymbol{b} = 0, \tag{1.17}$$

$$\int_{\partial P} (\boldsymbol{x} - \boldsymbol{o}) \times \boldsymbol{s} + \int_{\partial P} (\boldsymbol{x} - \boldsymbol{o}) \times \boldsymbol{b} = 0, \tag{1.18}$$

must be satisfied in body P and for any choice of the origin $\boldsymbol{o}$. The Cauchy theorem states that if σ and $\boldsymbol{b}$ are a system of forces for the body during a motion, a necessary and sufficient condition to test the balance laws to hold for any part of the body P is the existence of a spatial tensorial field $\boldsymbol{T}$, Cauchy stress tensor, such that

- The traction is a linear function of the unit normal $\boldsymbol{n}$ through the Cauchy stress:
$$\boldsymbol{s}(\boldsymbol{n}) = \boldsymbol{T}\boldsymbol{n}. \tag{1.19}$$

- $\boldsymbol{T}$ satisfies the local equations of motion:
$$\operatorname{div} \boldsymbol{T} + \boldsymbol{b} = 0. \tag{1.20}$$

- The Cauchy stress tensor is symmetric:
$$\boldsymbol{T} \in Sym. \tag{1.21}$$

Stress represents the internal counterpart to forces applied by the external environment to the body in its actual configuration and therefore, is a spatial quantity. Using the Nanson's formula it has been possible to derive the following identity

$$\boldsymbol{T}\boldsymbol{n}da = \boldsymbol{S}\boldsymbol{n}_0 da_0 \tag{1.22}$$

where

$$\boldsymbol{S} = J\boldsymbol{T}\boldsymbol{F}^{-T} \tag{1.23}$$

is the first Piola-Kirchhoff stress tensor, while $\boldsymbol{S}\boldsymbol{n}_0$ is the nominal traction. Introducing the so-called Kirchhoff stress, Eq. (1.23) can be rewritten in this form

$$\boldsymbol{S} = \boldsymbol{K}\boldsymbol{F}^{-T}, \tag{1.24}$$

in which is assumed

$$\boldsymbol{K} = J\boldsymbol{T}. \tag{1.25}$$

The first Piola-Kirchhoff stress tensor is the transpose of the nominal stress tensor

$$\boldsymbol{t} = \boldsymbol{S}^T = \boldsymbol{F}^{-1}\boldsymbol{K} \tag{1.26}$$

the main feature of the first Piola-Kirchhoff stress is that $\boldsymbol{S}\boldsymbol{n}_0$ is a measure of the surface force per unit area in the reference configuration. This means that the first Piola-Kirchhoff stress satisfies

$$\int_{\partial P} \boldsymbol{T}\boldsymbol{n} = \int_{\partial P_0} \boldsymbol{S}\boldsymbol{n}_0 \tag{1.27}$$

Introducing, in the reference configuration, the body forces $\boldsymbol{b}_0 = J\boldsymbol{b}$ and neglecting the inertial forces, the balance laws become

$$\int_{\partial P_0} \boldsymbol{S}\boldsymbol{n}_0 + \int_{P_0} \boldsymbol{b}_0 = 0, \tag{1.28}$$

and

$$\int_{\partial P_0} (\boldsymbol{x} - \boldsymbol{o}) \times \boldsymbol{S}\boldsymbol{n}_0 + \int_{P_0} (\boldsymbol{x} - \boldsymbol{o}) \times \boldsymbol{b}_0 = 0, \tag{1.29}$$

so, neglecting the inertia, the translational equilibrium of spatial element imposed on reference configuration is expressed in the following classical way

$$\operatorname{Div} \boldsymbol{S} + \boldsymbol{b}_0 = 0. \tag{1.30}$$

1.3.2 Motion

The definition of motion can be found in Bigoni (2012), in which the motion is described as an ordered sequence of mappings of a reference configuration into current configurations, ordered by the time t

$$\boldsymbol{x} = \boldsymbol{g}(\boldsymbol{x}_0, t) \tag{1.31}$$

and

$$\boldsymbol{x}_0 = \boldsymbol{g}^{-1}(\boldsymbol{x}, t). \tag{1.32}$$

Therefore, it is possible to introduce the material $\dot{\boldsymbol{x}}$ and spatial $\boldsymbol{v}$ descriptions of the velocity

$$\dot{\boldsymbol{x}}(\boldsymbol{x}_0, t) = \frac{\partial \boldsymbol{g}(\boldsymbol{x}_0, t)}{\partial t} \tag{1.33}$$

and

$$\boldsymbol{v}(\boldsymbol{x}, t) = \dot{\boldsymbol{x}}(\boldsymbol{g}^{-1}(\boldsymbol{x}, t), t). \tag{1.34}$$

The material $\ddot{\boldsymbol{x}}$ and spatial $\boldsymbol{a}$ descriptions of the acceleration

$$\ddot{\boldsymbol{x}}(\boldsymbol{x}_0, t) = \frac{\partial^2 \boldsymbol{g}(\boldsymbol{x}_0, t)}{\partial^2 t} \tag{1.35}$$

and

$$\boldsymbol{a}(\boldsymbol{x}, t) = \ddot{\boldsymbol{x}}(\boldsymbol{g}^{-1}(\boldsymbol{x}, t), t). \tag{1.36}$$

Now, it is possible to introduced the following three time derivatives useful in the following treatments

- The material time derivative of a material field $\boldsymbol{A}(\boldsymbol{x}_0, t)$, holding $\boldsymbol{x}_0$ fixed:

$$\dot{\boldsymbol{A}}(\boldsymbol{x}_0, t) = \frac{\partial \boldsymbol{A}(\boldsymbol{x}_0, t)}{\partial t}. \tag{1.37}$$

- The material time derivative of spatial field $\boldsymbol{A}(\boldsymbol{x}, t)$:

$$\dot{\boldsymbol{A}}(\boldsymbol{x}, t) = \left.\frac{\partial \boldsymbol{A}(\boldsymbol{g}(\boldsymbol{x}_0, t), t)}{\partial t}\right|_{\boldsymbol{x}_0 = \boldsymbol{g}^{-1}(\boldsymbol{x}, t)}. \tag{1.38}$$

  so that $\boldsymbol{x}_0$ is held fixed.

- The spatial time derivative of a spatial field $\boldsymbol{A}(\boldsymbol{x}, t)$, holding $\boldsymbol{x}$ fixed:

$$\boldsymbol{A}'(\boldsymbol{x}, t) = \frac{\partial \boldsymbol{A}(\boldsymbol{x}, t)}{\partial t}. \tag{1.39}$$

Others important and usefull definition is the gradient of the material and spatial description of the velocity

$$\dot{\boldsymbol{F}} = \operatorname{Grad} \dot{\boldsymbol{x}}(\boldsymbol{x}_0, t), \qquad \boldsymbol{L}(\boldsymbol{x}, t) = \operatorname{grad} \boldsymbol{v}. \tag{1.40}$$

Observing that

$$\dot{\boldsymbol{x}}(\boldsymbol{x}_0, t) = \boldsymbol{v}(\boldsymbol{g}(\boldsymbol{x}_0, t), t) \tag{1.41}$$

taking the gradient with respect $\boldsymbol{x}_0$ and using the chian rule of differentiation, the relation between the gradient of the material and spatial description of the velocity is obtained

$$\dot{\boldsymbol{F}} = \boldsymbol{L}\boldsymbol{F}. \tag{1.42}$$

For every material fibre, denoted by $w_0\boldsymbol{w}_0$, employing Eq. (1.42) and recalling that $(w_0\boldsymbol{w}_0)^{\cdot} = 0$ because $w_0\boldsymbol{w}_0$ is fixed, the rate of change of the line element

$$(w\boldsymbol{w})^{\cdot} = \dot{\boldsymbol{F}}(w_0\boldsymbol{w}_0) = \boldsymbol{L}(w\boldsymbol{w}). \tag{1.43}$$

Starting from this equation, it may obtained

$$\dot{\boldsymbol{w}} = (\boldsymbol{I} - \boldsymbol{w} \otimes \boldsymbol{w})\boldsymbol{L}^T\boldsymbol{w} \tag{1.44}$$

that provide the rate of change of a spatial oriented direction $\boldsymbol{w}$. Analogously, the rate of change of the unit normal and tangent vectors to an embedded area element

$$\dot{\boldsymbol{t}} = (\boldsymbol{I} - \boldsymbol{t} \otimes \boldsymbol{t})\boldsymbol{L}^T\boldsymbol{t} \tag{1.45}$$

and

$$\dot{\boldsymbol{n}} = -(\boldsymbol{I} - \boldsymbol{n} \otimes \boldsymbol{n})\boldsymbol{L}^T\boldsymbol{n} \tag{1.46}$$

in which the symbol $\otimes$ is the dyadic product.

1.4 Constitutive equations

In this section some useful material models are introduced to describe the constitutive behaviors of the elastic and elasto-plastic materials like rubbers and metals. The Neo-Hookean model will be describe introducing the concept of incompressibility, it is a hyperelastic material model that it is used for predicting the nonlinear stress-strain behavior of materials undergoing large deformations. Another important constitutive model is the Von Mises Criterion that permit to describe the relation between stress and strain in ductile materials including the plasticity phenomena.

1.4.1 Incompressible isotropic elasticity and general formulation of the constitutive equations

Incompressible isotropic elasticity represents one of the most important constraint for the material model in the finite strain. The incompressibility constraint in terms of the principal stretches can be define as

$$\lambda_1 \lambda_2 \lambda_3 = 1. \tag{1.47}$$

The formulation of the constitutive equation can be expressed using the strain energy concept as reported in Bigoni (2012) to obtain the stresses

$$\boldsymbol{T}_i = -\pi + \lambda_i \frac{\partial W(\lambda_1, \lambda_2, \lambda_3)}{\partial \lambda_i}, \qquad i = 1, 2, 3 \tag{1.48}$$

in which π is a Lagrangean multiplier and W is the strain energy density that relates the stress/strain measures. Several models are developed, the Neo-Hookean elasticity and J2-Deformation theory of plasticity will be analyzed.

1.4.2 Neo-Hookean materials

The strain energy density for the Neo-Hookean material is

$$W(\lambda_i) = \frac{\mu_0}{2} \left(\lambda_1^2 + \lambda_2^2 + \lambda_3^2 - 3 \right) \tag{1.49}$$

where μ_0 is a material parameter that represents the shear stiffness in unstressed configuration.

Adding the incompressibility constraint, the Cauchy stress tensor becomes

$$\boldsymbol{T} = -\pi \boldsymbol{I} + \mu_0 (\boldsymbol{B} - \boldsymbol{I}). \tag{1.50}$$

where $\boldsymbol{B}$ is the left Cauchy-Green strain tensor and $\boldsymbol{I}$ is the identity matrix. Starting from Eq. (1.47), in case of plane strain condition $\lambda_3 = 1$ for an incompressible material

$$\lambda_1 = \frac{1}{\lambda_2} = \lambda \tag{1.51}$$

so, the left Cauchy-Green strain tensor $\boldsymbol{B}$ takes the following form

$$\boldsymbol{B} = \lambda^2 v_1 \otimes v_1 + \frac{1}{\lambda^2} v_2 \otimes v_2 + v_3 \otimes v_3. \tag{1.52}$$

1.4.3 J2 Deformation theory of plasticity model

In this case a generalization of the hyperelastic finite strain model is assumed as proposed by Hutchinson and Neale (1978). Its importance stems from the fact that it can serve as Hill's linear compariso solid for elastc-plastic solids.

In particular, Hill (1958) has shown that for elastic-plastic solids and for a pre-bifurcation state corrisponding to continued plastic loading, the first possible bifurcation can be investigated for a solid, the so-called linear comparison solid, having moduli independent of rate quantities and corresponding to the active moduli in the pre-bifurcation state.

The corresponding strain energy density in terms of logarithmic strains is taken to be

$$W(\varepsilon_i) = \frac{K}{N+1}\left[\frac{2}{3}(\varepsilon_1^2 + \varepsilon_2^2 + \varepsilon_3^2)\right]^{\frac{N+1}{2}} \tag{1.53}$$

and remembering for the incompressibility constraint that

$$\varepsilon_1 + \varepsilon_2 + \varepsilon_3 = 0. \tag{1.54}$$

where K is a constitutive stiffness parameter and N is an hardening exponent, subject to the restriction $0 < N < 1$.

Chapter 2

Imperfect interface model for a thin soft layer

2.1 Introduction

A thin soft adhesive interphase is considered between dissimilar elastic media. The material of the intermediate layer is modelled by elasto-plastic pressure-sensitive constitutive law. An asymptotic procedure, together with a novel formulation of the deformation theory of plasticity for pressure-sensitive materials, is used in order to derive nonlinear transmission conditions for the corresponding imperfect zero-thickness interface. Here, Von Mises criterion is applied for the ductile material that is present in the thin layer, as shown in Fig. 2.1. Therefore, a non-classical formulation of this constitutive model is derived. The thickness of the layer is small in comparison with the characteristic size of the all mechanical system. The ductile material is assumed to be soft in comparison with the two adherents and may exhibit a very general non-linear constitutive behaviour, including compressible plastic deformations, the only assumption being that the material is isotropic. In general, employing an asymptotic procedure, the ductile thin layer is replaced by an imperfect interface of zero-thickness equipped with non-linear transmission conditions, Sonato et al. (2015) for details. The transmission conditions, in plane strain, are given by the continuity of tractions across the interface.

The imperfect interface model will be useful in Chapter 4 to describe the behaviour of a shear band inside a ductile matrix from the point of

view of the incremental state of stresses. In fact, the incremental form of the transmission conditions through the imperfect interface will result to be equal to the classical incremental conditions that described the propagation of a shear band.

2.2 Definition of the problem

The problem is formulated through mathematical laws that describe the behavior of the materials that make up the structural system. In par-

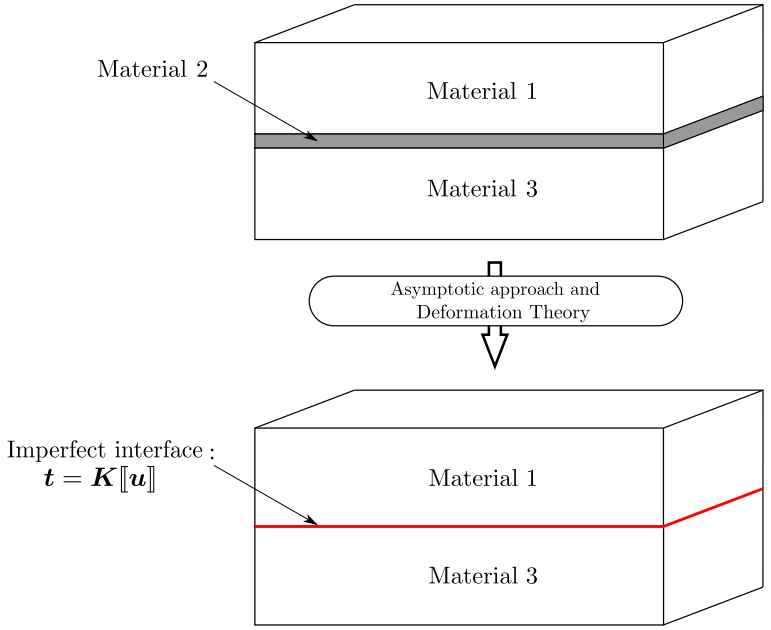

Figure 2.1: A thin soft interphase is considered between dissimilar elastic media in the real mechanic system and its transformation in an imperfect interface equipped by the transmission conditions laws derived by the asymptotic procedure.

ticular, three different materials are considered that have a linear elastic behavior described through the following laws of Hooke:

$$\sigma_{ij}^{(l)} = 2\mu^{(l)}\varepsilon_{ij}^{(l)} + \lambda^{(l)}\varepsilon_{kk}^{(l)}\delta_{ij} \qquad \boldsymbol{x} \in \Omega_l \qquad l = 1, 2, 3 \tag{2.1}$$

where σ_{ij}, ε_{ij} are the components of the stress and the deformation tensors, while μ and λ represent the parameters of Lamé for the materials ($l =$

$1, 2, 3$). It is possible to refer to the parameters E, ν, G and K because they depend on the parameters of Lamé through the following relations

$$E = \frac{\mu(3\lambda + 2\mu)}{\lambda + \mu} \qquad \nu = \frac{\lambda}{2(\lambda + \mu)} \qquad G = \mu, \qquad K = \lambda + \frac{2\mu}{3} \tag{2.2}$$

The analysis of the problem is carried out assuming that the materials adjacent to the imperfect interface are homogeneous, while the material with which the imperfect interface is formed is non-homogeneous and therefore the parameters μ and λ are a function of the vector position:

$$\mu^{(2)} = \mu^{(2)}(\boldsymbol{x}) \qquad \lambda^{(2)} = \lambda^{(2)}(\boldsymbol{x}) \tag{2.3}$$

The equations of equilibrium and congruence for the system, neglecting the forces of volume, are:

$$\operatorname{div} \boldsymbol{\sigma}^{(l)} = 0 \qquad \boldsymbol{x} \in \Omega_l \qquad l = 1, 2, 3 \tag{2.4}$$

$$\varepsilon_{ij} = \frac{1}{2}\left(\frac{\partial u_i}{\partial x_j} + \frac{\partial u_j}{\partial u_i}\right) \tag{2.5}$$

where $\boldsymbol{\sigma}$ represents the stress tensor, $\boldsymbol{\varepsilon}$ represents the strain tensor and u_j, $(j = 1, 2, 3)$, represent the components of the displacement vector. Now, inserting the congruence equations (2.5) in the law of Hooke (2.1) and then in the classical equilibrium equations we obtain the equations of Navier-Lamé:

$$\operatorname{grad}\left((\lambda^{(l)} + \mu^{(l)}) \operatorname{div}\right) \boldsymbol{u}^{(l)} + (\nabla \cdot \mu^{(l)} \nabla)\boldsymbol{u}^{(l)} = 0 \qquad \boldsymbol{x} \in \Omega_l \tag{2.6}$$

In the formulation under examination the parameters of Lamé are constant for the materials adjacent to the interface and therefore can be taken out of the operators in the (2.6). Let's assume that the imperfect interface has a constant thickness of $2h$ on the $x_1 - x_3$ plane. The plans in which the boundary conditions of the interface are defined are at $x_2 = \pm h$ and the following Transmission Conditions are satisfied along these planes

$$\boldsymbol{u}^{(2)} = \boldsymbol{u}^{(1)} \qquad \boldsymbol{\sigma}_y^{(2)} = \boldsymbol{\sigma}_y^{(1)} \qquad y = h \tag{2.7}$$

$$\boldsymbol{u}^{(2)} = \boldsymbol{u}^{(3)} \qquad \boldsymbol{\sigma}_y^{(2)} = \boldsymbol{\sigma}_y^{(3)} \qquad y = -h \tag{2.8}$$

A parameter ϵ is introduced that allows to rescale the geometric and mechanical characteristics of the interface:

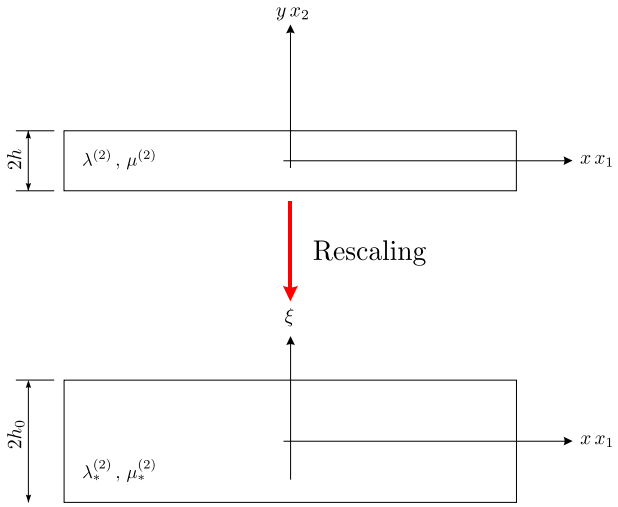

Figure 2.2: Rescaling operation of the variables of the real problem.

$$\epsilon \ll 1 \tag{2.9}$$

$$h = \epsilon h_* \tag{2.10}$$

$$E^{(2)}(\boldsymbol{x}) = \epsilon E_*(\boldsymbol{x}) \tag{2.11}$$

Furthermore, it is assumed that the parameters describing the behavior of the various materials $E_*(\boldsymbol{x})$ and $E^{(l)}$, $(l = 1, 3)$ are of the same order of magnitude and independent from the position vector within the interface and that the following relation is valid for the Poisson module:

$$\nu^{(2)} = \nu_* < \frac{1}{2} \tag{2.12}$$

The parameters of Lamé take on an asymptotic behavior due to the ϵ parameter:

$$\mu(x, \epsilon\xi) = \epsilon\mu_*(x, \xi) \tag{2.13}$$

$$\lambda(x, \xi) = \epsilon\lambda_*(x, \xi) \tag{2.14}$$

$$0 < \mu^{(2)}(\boldsymbol{x}) = \epsilon\mu_*(\boldsymbol{x}), \qquad 0 < \lambda^{(2)}(\boldsymbol{x}) = \epsilon\lambda_*(\boldsymbol{x}) \tag{2.15}$$

2.2.1 Derivation of the Transmission Conditions for the imperfect interface model

The Transmission Conditions are derived from the asymptotic analysis through the introduction of the parameter ϵ, which rediscovers the independent variable x_2 and the variables related to it. Let's consider a flat problem for a solid formed by two elastic materials joined by a constant thickness intermediate polymeric adhesive $\Omega_h = \Omega_+ \cup \Omega_- \cup \Omega$, where $\Omega_\pm = \{(x, y), \pm y \geq h\}$, $\Omega = \{(x, y), |y| \leq h\}$. We assume that the intermediate interface is non-homogeneous and isotropic, while the two elastic materials are homogeneous and isotropic. For a solid body, neglecting the

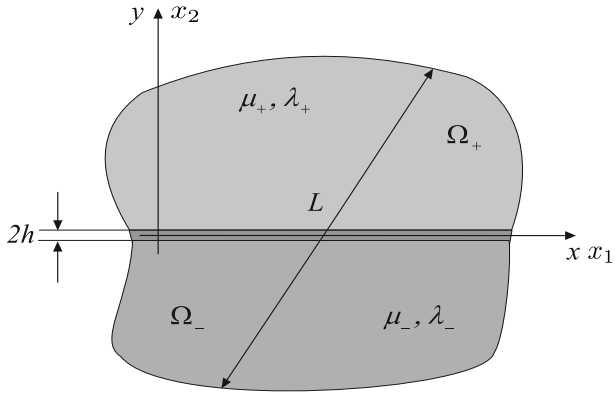

Figure 2.3: Generic 2D solid body with an imperfect interface inside.

volume forces, the following relationships are valid

$$\operatorname{div} \sigma_{ij} = 0 \tag{2.16}$$

$$\varepsilon_{ij} = \frac{1}{2}\left(\frac{\partial u_i}{\partial x_j} + \frac{\partial u_j}{\partial x_i}\right) \tag{2.17}$$

$$\sigma_{ij} = \lambda(tr\varepsilon_{ij})I_{ij} + 2\mu\varepsilon_{ij} \tag{2.18}$$

Considering the Plane Strain problem the (2.16) becomes

$$\frac{\partial \sigma_{xx}}{\partial x} + \frac{\partial \sigma_{xy}}{\partial y} = 0$$

$$\frac{\partial \sigma_{yx}}{\partial x} + \frac{\partial \sigma_{yy}}{\partial y} = 0$$

Substituting the (2.17) in the (2.18) we get

$$\begin{pmatrix} \sigma_{xx} & \sigma_{xy} \\ \sigma_{yx} & \sigma_{yy} \end{pmatrix} = \begin{pmatrix} \lambda(\frac{\partial u_x}{\partial x} + \frac{\partial u_y}{\partial y}) + 2\mu(\frac{\partial u_x}{\partial x}) & \mu\frac{\partial u_x}{\partial y} + \frac{\partial u_y}{\partial x} \\ \mu(\frac{\partial u_x}{\partial y} + \frac{\partial u_y}{\partial x}) & \lambda(\frac{\partial u_x}{\partial x} + \frac{\partial u_y}{\partial y}) + 2\mu\frac{\partial u_y}{\partial y} \end{pmatrix} \tag{2.19}$$

Now the stress tensor σ_{ij} results from the displacements u_x, u_y and applying to it the operator divσ_{ij} determine

$$\frac{\partial}{\partial x}(\lambda\frac{\partial u_y}{\partial y} + \frac{\partial u_x}{\partial x}(\lambda + 2\mu)) + \frac{\partial}{\partial y}(\mu(\frac{\partial u_x}{\partial y} + \frac{\partial u_y}{\partial x})) = 0 \tag{2.20}$$

$$\frac{\partial}{\partial x}(\mu(\frac{\partial u_y}{\partial x} + \frac{\partial u_x}{\partial y})) + \frac{\partial}{\partial y}(\lambda\frac{\partial u_x}{\partial x} + \frac{\partial u_y}{\partial y}(\lambda + 2\mu)) = 0 \tag{2.21}$$

Collecting common factors and rewriting everything in matrix form yield

$$\begin{pmatrix} (\lambda + 2\mu)D_x^2 + \mu D_y^2 & (\lambda + \mu)D_x D_y \\ (\lambda + \mu)D_x D_y & (\lambda + 2\mu)D_y^2 + \mu D_x^2 \end{pmatrix} \begin{pmatrix} u_x \\ u_y \end{pmatrix} = \begin{pmatrix} 0 \\ 0 \end{pmatrix} \tag{2.22}$$

where

$$D_x^2 = \frac{\partial\partial}{\partial x \partial x}, \qquad D_x = \frac{\partial}{\partial x}, \qquad D_y^2 = \frac{\partial\partial}{\partial y \partial y}, \qquad D_y = \frac{\partial}{\partial y}$$

Defining the operator $\mathcal{L}$

$$\mathcal{L} = \begin{pmatrix} (\lambda + 2\mu)D_x^2 + \mu D_y^2 & (\lambda + \mu)D_x D_y \\ (\lambda + \mu)D_x D_y & (\lambda + 2\mu)D_y^2 + \mu D_x^2 \end{pmatrix} \tag{2.23}$$

the equation of Navier-Lamé can be rewrite in the following way

$$\begin{pmatrix} \mathcal{L}_{xx} & \mathcal{L}_{yx} \\ \mathcal{L}_{yx} & \mathcal{L}_{yy} \end{pmatrix} \begin{pmatrix} u_x \\ u_y \end{pmatrix} = \begin{pmatrix} 0 \\ 0 \end{pmatrix} \tag{2.24}$$

Now, remembering the formulation of the problem and referring to the Eq. (2.14) and the Eq. (2.13), it is possible through the asymptotic calculation to define the new operator $\mathcal{L}_*$

$$\mathcal{L}_* = \begin{pmatrix} (\epsilon\lambda_* + 2\epsilon\mu_*)D_x^2 + \frac{\mu_*}{\epsilon}D_\xi^2 & (\lambda_* + \mu_*)D_x D_\xi \\ (\lambda_* + \mu_*)D_x D_\xi & (\frac{\lambda_*}{\epsilon} + 2\frac{\mu_*}{\epsilon})D_\xi^2 + \epsilon\mu_* D_x^2 \end{pmatrix} \tag{2.25}$$

This operator can be rewritten as the sum of differential operators

$$\mathcal{L}_* = \epsilon^{-1}\mathcal{L}_0 + \mathcal{L}_1 + \epsilon\mathcal{L}_2 \tag{2.26}$$

in which

$$\mathcal{L}_0 = \begin{pmatrix} \frac{\partial}{\partial\xi}\mu_*\frac{\partial}{\partial\xi} & 0 \\ 0 & \frac{\partial}{\partial\xi}(\lambda_* + 2\mu_*)\frac{\partial}{\partial\xi} \end{pmatrix} \tag{2.27}$$

$$\mathcal{L}_1 = \begin{pmatrix} 0 & \frac{\partial}{\partial x}(\lambda_* + \mu_*)\frac{\partial}{\partial\xi} \\ \frac{\partial}{\partial x}(\lambda_* + \mu_*)\frac{\partial}{\partial\xi} & 0 \end{pmatrix} \tag{2.28}$$

$$\mathcal{L}_2 = \begin{pmatrix} \frac{\partial}{\partial x}(\lambda_* + 2\mu_*)\frac{\partial}{\partial x} & 0 \\ 0 & \frac{\partial}{\partial x}\mu_*\frac{\partial}{\partial x} \end{pmatrix} \tag{2.29}$$

Through mathematical passages similar to those just carried out, the relationship between the stress vector and the displacement vector can be written as follows

$$\boldsymbol{\sigma}_y(x, y) = \mathcal{M}\boldsymbol{u}(x, y) \tag{2.30}$$

The $\mathcal{M}$ operator can be rewritten, always referring to the Eqs. (2.14) and (2.13), through the asymptotic calculation as the sum of differential operators in the following way

$$\mathcal{M}_* = \epsilon^{-1}\mathcal{M}_0 + \mathcal{M}_1 \tag{2.31}$$

in which

$$\mathcal{M}_0 = \begin{pmatrix} \mu_*\frac{\partial}{\partial\xi} & 0 \\ 0 & (\lambda_* + 2\mu_*)\frac{\partial}{\partial\xi} \end{pmatrix} \tag{2.32}$$

$$\mathcal{M}_1 = \begin{pmatrix} 0 & \mu_*\frac{\partial}{\partial x} \\ \lambda_*\frac{\partial}{\partial x} & 0 \end{pmatrix} \tag{2.33}$$

Considering the relationship between carrier displacements in the real problem and rescaled

$$\boldsymbol{w}(x, \xi) = \boldsymbol{u}_\pm(x, y) \tag{2.34}$$

the solution is determined within the domain in the form of asymptotic series

$$\boldsymbol{w}(x, \xi) = \sum_{k=0}^{\infty} \epsilon^k \boldsymbol{w}_k(x, \xi) \tag{2.35}$$

$$\boldsymbol{u}_\pm(x, y) = \sum_{k=0}^{\infty} \epsilon^k \boldsymbol{u}_k^\pm(x, y) \tag{2.36}$$

$$\boldsymbol{\sigma}_{\pm}(x,\xi) = \sum_{k=0}^{\infty} \epsilon^k \boldsymbol{\sigma}_k^{\pm}(x,\xi) \tag{2.37}$$

the following mathematical system is defined

$$(\epsilon^{-1}\mathcal{L}_0 + \mathcal{L}_1 + \epsilon\mathcal{L}_2)\epsilon \begin{pmatrix} w_{1x} + \epsilon^{-1}w_{0x} \\ w_{1y} + \epsilon^{-1}w_{0y} \end{pmatrix} = \begin{pmatrix} 0 \\ 0 \end{pmatrix} \tag{2.38}$$

At this point, the following equations can be obtained by developing the components of the vector $\boldsymbol{w}_0$:

$$\frac{\mathcal{L}_0}{\epsilon} \begin{pmatrix} w_{0x} \\ w_{0y} \end{pmatrix} = \begin{pmatrix} 0 \\ 0 \end{pmatrix} \tag{2.39}$$

$$\boldsymbol{u}_0^{\pm}(x,\pm 0) = \boldsymbol{w}_0(x,\pm h_0) \tag{2.40}$$

From Eqs. (2.40) and (2.39) it is possible to determine the components of the vector directly $\boldsymbol{w}_0$, indicating with:

$$\mathbb{A} = \begin{pmatrix} \mu_* & 0 \\ 0 & \lambda_* + 2\mu_* \end{pmatrix} \tag{2.41}$$

$$\frac{\partial}{\partial\xi}\mathbb{A}(x,\xi)\frac{\partial}{\partial\xi}\boldsymbol{w}_0(x,\xi) = 0 \tag{2.42}$$

integrating a first time

$$\mathbb{A}(x,\xi)\frac{\partial}{\partial\xi}\boldsymbol{w}_0(x,\xi) = \boldsymbol{a}(x) \tag{2.43}$$

and then a second one gets:

$$\boldsymbol{w}_0(x,\xi) = \int_{-h_0}^{\xi} \mathbb{A}^{-1}(x,t)\,\boldsymbol{a}(x)\,dt + \boldsymbol{b}(x) \tag{2.44}$$

From Eq. (2.44) it is noted that the tensile stress in the thin layer is independent of ξ

$$\sigma_y^{(2)} = \mathbb{A}(x,\xi)\frac{\partial}{\partial\xi}\boldsymbol{w}_0(x,\xi) \tag{2.45}$$

with $\sigma_y^{(2)}$ constant along the vertical direction. It can therefore be concluded that:

$$\boldsymbol{\sigma}_y^{(2)} = \boldsymbol{\sigma}_y^{(1)} = \boldsymbol{\sigma}_y^{(3)} \tag{2.46}$$

The vectors $\boldsymbol{a}(x)$ e $\boldsymbol{b}(x)$ can be easily determined by the boundary conditions expressed in Eqs. (2.8) and considering the Eq. (2.30):

$$\boldsymbol{b}(x) = \boldsymbol{u}^{(3)}(x) \qquad \boldsymbol{a}(x) = \boldsymbol{\sigma}_y^{(3)}(x) \tag{2.47}$$

from which we can see that the vector $\boldsymbol{\sigma}_y^{(3)}(x)$ does not depend on the variable ξ and therefore on the variable y in the real problem. Then:

$$\boldsymbol{w}_0(x,\xi) = \int_{-h_0}^{\xi} \mathbb{A}^{-1}(x,t)\,dt\,\boldsymbol{a}(x) + \boldsymbol{b}(x) \tag{2.48}$$

It can be seen now that the $\mathbb{A}$ array contains constant terms that do not vary within the thickness of the adhesive layer and are therefore independent of the ξ variable. Integrating on the whole thickness and taking into account the boundary conditions on the equalities of the displacements in the real problem determine:

$$\boldsymbol{u}^{(1)}(x) - \boldsymbol{u}^{(3)}(x) = \int_{-h}^{h} \mathbb{A}^{-1}(x,t)\,dt\,\boldsymbol{\sigma}_y^{(3)}(x) \tag{2.49}$$

At this point, it is possible to write the final conditions describing the transmission of the stresses through the imperfect interface indicating with the term jump the notation $[[f_x]] = f(y=h) - f(y=-h)$

$$\boldsymbol{\sigma}_y^{(1)}(x) = \boldsymbol{\sigma}_y^{(3)}(x) \tag{2.50}$$

so

$$[[\sigma_{xy}]] = 0 \qquad [[\sigma_{yy}]] = 0 \tag{2.51}$$

Assuming also that the thickness of the interface is constant

$$\begin{pmatrix} [[u_1]] \\ [[u_2]] \end{pmatrix} = \begin{pmatrix} \tau_1 & 0 \\ 0 & \tau_2 \end{pmatrix} \begin{pmatrix} \sigma_{xy} \\ \sigma_{yy} \end{pmatrix} \tag{2.52}$$

in which

$$\tau_1 = 2h\frac{1}{\mu} \tag{2.53}$$

$$\tau_2 = 2h\frac{1}{\lambda + 2\mu} \tag{2.54}$$

and finally, in plane strain conditions,

$$\begin{pmatrix} \sigma_{xy} \\ \sigma_{yy} \end{pmatrix} = \frac{1}{2h} \begin{pmatrix} \mu & 0 \\ 0 & \lambda + 2\mu \end{pmatrix} \begin{pmatrix} [[u_1]] \\ [[u_2]] \end{pmatrix} \tag{2.55}$$

2.3 Deformation Theory

Focusing on the parameters of Lamé it is possible to notice how these are in function of the deformation field that affects the imperfect interface. In particular, the following dependencies can be highlighted:

$$\lambda = \lambda(J_1^\varepsilon, J_2^e) \tag{2.56}$$

$$\mu = \mu(J_1^\varepsilon, J_2^e) \tag{2.57}$$

where J_1^ε and J_2^e respectively represent the invariant of the first order of the deformation tensor and the second invariant of the tensor representing the deviatoric part of the tensor of the deformations. In fact, the deformation tensor can be written by adding together the volumetric part and the deviatoric part in the following way:

$$\begin{pmatrix} \varepsilon_{11} & \varepsilon_{12} & \varepsilon_{13} \\ \varepsilon_{21} & \varepsilon_{22} & \varepsilon_{23} \\ \varepsilon_{31} & \varepsilon_{32} & \varepsilon_{33} \end{pmatrix} = \begin{pmatrix} \varepsilon_m & 0 & 0 \\ 0 & \varepsilon_m & 0 \\ 0 & 0 & \varepsilon_m \end{pmatrix} + \begin{pmatrix} \varepsilon_{11} - \varepsilon_m & \varepsilon_{12} & \varepsilon_{13} \\ \varepsilon_{21} & \varepsilon_{22} - \varepsilon_m & \varepsilon_{23} \\ \varepsilon_{31} & \varepsilon_{32} & \varepsilon_{33} - \varepsilon_m \end{pmatrix} \tag{2.58}$$

$$\varepsilon_{ij} = \varepsilon_m I + e_{ij} \tag{2.59}$$

where

$$\varepsilon_m = \frac{1}{3}(\varepsilon_{11} + \varepsilon_{22} + \varepsilon_{33}) \tag{2.60}$$

$$I = \begin{pmatrix} 1 & 0 & 0 \\ 0 & 1 & 0 \\ 0 & 0 & 1 \end{pmatrix} \tag{2.61}$$

In the same way the stress tensor can also be written adding together the volumetric part and the deviatoric part

$$\begin{pmatrix} \sigma_{11} & \sigma_{12} & \sigma_{13} \\ \sigma_{21} & \sigma_{22} & \sigma_{23} \\ \sigma_{31} & \sigma_{32} & \sigma_{33} \end{pmatrix} = \begin{pmatrix} \sigma_m & 0 & 0 \\ 0 & \sigma_m & 0 \\ 0 & 0 & \sigma_m \end{pmatrix} + \begin{pmatrix} \sigma_{11} - \sigma_m & \sigma_{12} & \sigma_{13} \\ \sigma_{21} & \sigma_{22} - \sigma_m & \sigma_{23} \\ \sigma_{31} & \sigma_{32} & \sigma_{33} - \sigma_m \end{pmatrix} \tag{2.62}$$

$$\sigma_{ij} = \sigma_m I + s_{ij} \tag{2.63}$$

where I always represents the identity matrix, while

$$\sigma_m = \frac{1}{3}(\sigma_{11} + \sigma_{22} + \sigma_{33}) \tag{2.64}$$

Applying asymptotic calculation

$$\varepsilon_{ij} = O_1 \qquad \varepsilon_{i2} = \frac{1}{2}\frac{\partial u_i}{\partial x_2} + O_1 \qquad i,j = 1,3 \qquad \varepsilon_{22} = \frac{\partial u_2}{\partial x_2} \tag{2.65}$$

and define the invariants

$$J_1^{\varepsilon} = \varepsilon_{22}, \tag{2.66}$$

$$J_2^{e} = \frac{1}{3}\varepsilon_{22}^2 + \varepsilon_{12}^2 + \varepsilon_{23}^2. \tag{2.67}$$

Using the Transmission Condition (2.55) is possible to write invariants in terms of jump displacement components

$$J_1^{\varepsilon} = \frac{1}{2h}[[u_2]], \tag{2.68}$$

$$J_2^{e} = \frac{1}{12h^2}[[u_2]]^2 + \frac{1}{16h^2}[[u_1]]^2 + \frac{1}{16h^2}[[u_3]]^2. \tag{2.69}$$

Let us now introduce the following hypotheses in order to identify the plastic component that influences the parameters of Lamé and then adapt them in the case of elasto-plastic constitutive models that describe the behavior of the imperfect interface:

- Initially isotropic material
- The main axes of the plastic deformation tensor ϵ_{ij}^p are always coincident with the stress tensor axes σ_{ij}^p
- The tensor constituted by the deviatoric part e_{ij}^p of the deformation tensor is proportional to the tensor constituted by the deviatoric part s_{ij} of the stress tensor.

It is possible to write

$$\varepsilon_{ij} = \varepsilon_{ij}^e + \varepsilon_{ij}^p = (\varepsilon_m^e + \varepsilon_m^p)I + e_{ij}^e + e_{ij}^p, \tag{2.70}$$

$$\varepsilon_{ij}^e = \varepsilon_m^e I + e_{ij}^e. \tag{2.71}$$

The plastic deformation can be rewritten by introducing two functions ϕ_1, ϕ_2 that allow to describe the hardening behavior of the material composing the interface:

$$\varepsilon_{ij}^p = \phi_1 \sigma_m I + \phi_2 s_{ij}, \tag{2.72}$$

$$\varepsilon_{ij}^{e} = \frac{s_{ij}}{2G} \qquad \varepsilon_{m}^{e} = \frac{\sigma_m}{3K} \tag{2.73}$$

Replacing the Eqs. (2.72) and (2.73) in the Eq. (2.70), and remembering the Eq. (2.2) relationship determines

$$\varepsilon_{ij} = \left(\frac{1+\nu}{E} + \phi_2\right) s_{ij} + \left(\frac{1-2\nu}{E} + \phi_1\right) \sigma_m I \tag{2.74}$$

Using the Eqs. (2.63), (2.70), (2.72) and (2.73) yield

$$\varepsilon_{ij} = \left(\frac{1+\nu}{E} + \phi_2\right) \sigma_{ij} - \left(\frac{3\nu}{E} + \phi_2 - \phi_1\right) \frac{E}{1-2\nu+\phi_{1E}} \varepsilon_m I \tag{2.75}$$

then

$$\sigma_{ij} = \left(\frac{E}{1+\nu+E\phi_2}\right) \varepsilon_{ij} + \left(\frac{E}{1+\nu+E\phi_2}\right) \left(\frac{3\nu + (\phi_2 - \phi_1)E}{1-2\nu+E\phi_1}\right) \varepsilon_m I. \tag{2.76}$$

At this point, it is easy to determine the parameters of Lamé as a function of ϕ_1 and ϕ_2

$$\mu(\phi_2) = \frac{E}{2(1+\nu+\phi_2 E)}, \tag{2.77}$$

$$\lambda(\phi_1, \phi_2) = E \frac{3\nu + (\phi_2 - \phi_1)E}{3(1+\nu+E\phi_2)(1-2\nu+E\phi_1)}, \tag{2.78}$$

$$\lambda(\phi_1, \phi_2) + 2\mu(\phi_2) = E \frac{3(1-\nu) + (\phi_2 + 2\phi_1)E}{3(1+\nu+E\phi_2)(1-2\nu+E\phi_1)}. \tag{2.79}$$

By imposing the necessary conditions for the developed deformation theory to be valid within the imperfect interface

$$E > 0 \qquad -1 < \nu < 0.5, \tag{2.80}$$

so

$$\phi_2 > 0 \qquad \phi_1 > -\frac{1-2\nu}{E} \qquad (\phi_2 - \phi_1) > -\frac{3\nu}{E}. \tag{2.81}$$

We now define the functions ϕ_1 and ϕ_2 and to do this the relationships between the invariants of the stress tensor and strain tensor are considered

$$J_1^{\varepsilon^p} = \varepsilon_{kk}^{p} \qquad J_1^{\sigma} = \sigma_{kk} \tag{2.82}$$

$$J_2^{e^p} = \frac{1}{2} e_{ij}^p e_{ij}^p \qquad J_2^s = \frac{1}{2} s_{ij} s_{ij} \tag{2.83}$$

from Eq. (2.72)

$$J_1^{\varepsilon^p} = 3\phi_1 \sigma_m = J_1^\sigma \phi_1, \tag{2.84}$$

$$J_2^{e^p} = \frac{1}{2} \phi_2^2 s_{ij} s_{ij} = \phi_2^2 J_2^s. \tag{2.85}$$

Therefore, in the case of multiaxial state of stress

$$\phi_1 = \frac{J_1^{\varepsilon^p}}{J_1^\sigma}, \tag{2.86}$$

$$\phi_2 = \sqrt{\frac{J_2^{e^p}}{J_2^s}}. \tag{2.87}$$

2.3.1 Von Mises yield criterion

Suppose the imperfect interface behaves according to the Von Mises criterion, the yield surface is described in the following relation

$$F(J_2^s) = \sqrt{J_2^s} - k_s \tag{2.88}$$

According to the developed deformation theory, the tensor of plastic deformations can be written in the following form

$$\varepsilon_{ij}^p = \phi_2 s_{ij} \tag{2.89}$$

Furthermore, in the case of Von Mises material, $\phi_1 = 0$ and

$$\phi_2 = \phi_2(J_2^e) \tag{2.90}$$

while the parameters of Lamé and the elastic constants take the following form:

$$\mu(\phi_2) = \frac{E}{2(1 + \nu + \phi_2 E)}, \tag{2.91}$$

$$\lambda(\phi_2) = E \frac{3\nu + \phi_2 E}{3(1 + \nu + E\phi_2)(1 - 2\nu)}, \tag{2.92}$$

$$\lambda(\phi_2) + 2\mu(\phi_2) = E \frac{3(1 - \nu) + \phi_2 E}{3(1 + \nu + E\phi_2)(1 - 2\nu)}, \tag{2.93}$$

$$G(\phi_2) = \frac{E}{2(1+\nu+\phi_2 E)}, \tag{2.94}$$

$$E(\phi_2) = \frac{3E}{3+2E\phi_2}, \tag{2.95}$$

$$\nu(\phi_2) = \frac{3\nu+\phi_2 E}{3+2E\phi_2}, \tag{2.96}$$

$$K = \frac{E}{3(1-2\nu)}. \tag{2.97}$$

For a material that has a linear hardening, the function k_s in the Eq. (2.88) is

$$k_s = \sqrt{J_2^s} = \frac{\sigma_x}{\sqrt{3}} = \frac{E^p \varepsilon_x^p + \sigma_s}{\sqrt{3}} \tag{2.98}$$

Substituting ε_x^p with the equivalent plastic deformation, which is defined for a material at Von Mises as

$$\varepsilon_x^p = \frac{2}{\sqrt{3}}\sqrt{J_2^{e^p}} \tag{2.99}$$

yields

$$k_s = \frac{2}{3}E^p\sqrt{J_2^{e^p}} + \frac{\sigma_s}{\sqrt{3}} \tag{2.100}$$

The function ϕ_2 in the case of multiaxial stress state can be obtained by rewriting the second invariant of the deviatoric part of the stress and the strain and of the plastic deformation tensor according to the second invariant of the deviatoric part of the total strain tensor

$$\sqrt{J_2^s} = \frac{E(2E^p\sqrt{J_2^e} + \sqrt{3}\sigma_s)}{3E + 2(1\nu)E^p}, \tag{2.101}$$

$$\sqrt{J_2^{e^p}} = \frac{3E\sqrt{J_2^e} - \sqrt{3}(1+\nu)\sigma_s}{3E + 2(1\nu)E^p}. \tag{2.102}$$

The functions ϕ_1 e ϕ_2 are

$$\phi_1 = 0 \tag{2.103}$$

$$\phi_2 = \frac{3E\sqrt{J_2^e} - \sqrt{3}(1+\nu)\sigma_s}{E(2E^p\sqrt{J_2^e} + \sqrt{3}\sigma_s)} \tag{2.104}$$

Chapter 3

Incremental deformation theory

3.1 Introduction

The mechanics of incremental deformations superimposed upon a given strain allows the investigation of the response of a solid body subject to a pre-stress different direction. Essentially, a boundary-value problem and a set of solving incremental relationships have to be introduced. All the equations take into account the presence of a given pre-stress state. As pointed out by Biot, if we restrict attention to incremental deformation, the circustances that lead to a specific distribution of pre-stress within the body are not required to be known. Therefore, equations valid for any material model are established. Biot developed the corresponding theory in the monograph *Mechanics of Incremental Deformation*(1965). In the following sections we will focus on elastic material, isotropic in the initial state, for which explicit expressions for the stress are available at every stage of deformation and incremental equationscan be obtained directly from relative to finite strain. The mechanics of incremental deformations received much attention in relation to the developments of numerical techniques designed to solve nonlinear problems. On the other hand, from the theoretical point of view, several works have been published concerning criteria of stability and uniqueness of incremental boundary-value problems (Hill, 1957, 1978; Rice 1977) that provide useful tools in understanding the effective behaviour of loaded structures.

3.2 Incremental constitutive equations for incompressible, plane strain elasticity

Biot has provided a general procedure for incremental elastic incompressible constitutive equations. Starting from the relation between the Cauchy stress $\boldsymbol{T}$ and the left Cauchy-Green strain tensor $\boldsymbol{B}$ for a isotropic elastic solid the Biot constitutive equations can be obtain and in particular for the case of Neo-Hookean material. Taking the material time derivative of the Eq. (1.50), for the case of Mooney-Rivlin incompressible material as reported in Bigoni (2012), that is a generalization of the Neo-Hookean material model, yields

$$\dot{\boldsymbol{T}} = -\dot{\Pi}\boldsymbol{I} + \beta_0\dot{\boldsymbol{B}} + \beta_1(\dot{\boldsymbol{B}^{-1}}) + \dot{\beta}_0\boldsymbol{B} + \dot{\beta}_1\boldsymbol{B}^{-1} \tag{3.1}$$

in which

$$\dot{\boldsymbol{B}} = \boldsymbol{D}\boldsymbol{B} + \boldsymbol{B}\boldsymbol{D} + \boldsymbol{W}\boldsymbol{B} - \boldsymbol{B}\boldsymbol{W} \tag{3.2}$$

and

$$\dot{\boldsymbol{B}^{-1}} = -\boldsymbol{B}^{-1}\boldsymbol{D} - \boldsymbol{D}\boldsymbol{B}^{-1} + \boldsymbol{W}\boldsymbol{B}^{-1} - \boldsymbol{B}^{-1}\boldsymbol{W} \tag{3.3}$$

where $\boldsymbol{W}$ is the spin tensor and $\boldsymbol{D}$ is the Eulerian strain rate, while β_0 and β_1 are

$$\beta_0 = \frac{1}{\lambda_1^2 - \lambda_2^2}\left[\frac{(T_1 - T_3)\lambda_1^2}{\lambda_1^2 - \lambda_3^2} - \frac{(T_2 - T_3)\lambda_2^2}{\lambda_2^2 - \lambda_3^2}\right] \tag{3.4}$$

and

$$\beta_1 = \frac{1}{\lambda_1^2 - \lambda_2^2}\left[\frac{T_1 - T_3}{\lambda_1^2 - \lambda_3^2} - \frac{T_2 - T_3}{\lambda_2^2 - \lambda_3^2}\right] \tag{3.5}$$

Following the derivation in Bigoni (2012) and using the definition of Jaumann derivative the incremental costitutive equation valid for three-dimensional, incompressible Cauchy elasticity become

$$\begin{aligned}\widehat{\boldsymbol{T}} + \dot{\Pi}\boldsymbol{I} = \beta_0(\boldsymbol{D}\boldsymbol{B} + \boldsymbol{B}\boldsymbol{D}) - \beta_1(\boldsymbol{B}^{-1}\boldsymbol{D} + \boldsymbol{D}\boldsymbol{B}^{-1}) + \\ \left(\frac{\partial\overline{\beta}_0}{\partial\lambda_1}\dot{\lambda}_1 + \frac{\partial\overline{\beta}_0}{\partial\lambda_2}\dot{\lambda}_2\right)\boldsymbol{B} + \left(\frac{\partial\overline{\beta}_1}{\partial\lambda_1}\dot{\lambda}_1 + \frac{\partial\overline{\beta}_1}{\partial\lambda_2}\dot{\lambda}_2\right)\boldsymbol{B}^{-1}\end{aligned} \tag{3.6}$$

in which $\overline{\beta}_i$ are expressed as function of the principal stretches. Specialized these formulations for the case of incremental plane strain deformations

superimposed on a generic state of homogeneous deformation means

$$\operatorname{diag} \boldsymbol{B} = \left(\lambda_1^2, \lambda_2^2, \frac{1}{\lambda_1^2\lambda_2^2}\right), \qquad D_{i3} = D_{3i} = 0, \qquad i = 1, 2, 3, \tag{3.7}$$

so the out-of-plane stress rate components can be derived as

$$\widehat{T}_{33} = -\dot{\Pi} + \left[\frac{1}{\lambda_1^2\lambda_2^2}\left(\lambda_1^2\frac{\partial\overline{\beta}_0}{\partial\lambda_1} - \lambda_2^2\frac{\partial\overline{\beta}_0}{\partial\lambda_2}\right) + \lambda_1^2\lambda_2^2\left(\lambda_1^2\frac{\partial\overline{\beta}_1}{\partial\lambda_1} - \lambda_2^2\frac{\partial\overline{\beta}_1}{\partial\lambda_2}\right)\right] \left(\frac{D_{11} + D_{22}}{2}\right). \tag{3.8}$$

The incremental constitutive equations for plane strain incremental isochoric deformation superimposed on a given state of stress are

$$\begin{aligned} \widehat{T}_{12} &= 2\mu D_{12} \\ \widehat{T}_{11} - \widehat{T}_{22} &= 2\mu_*(D_{11} - D_{22}) \\ D_{11} &= -D_{22}. \end{aligned} \tag{3.9}$$

in which μ and μ_* are two incremental moduli corresponding to shearing parallel to and at 45° to the Eulerian principal axes. In detail, they can expressed as functions of the principal stretches

$$\mu = \frac{\lambda_1^2 + \lambda_2^2}{2}\left(\overline{\beta}_0 - \frac{\overline{\beta}_1}{\lambda_1^2\lambda_2^2}\right), \tag{3.10}$$

and

$$\mu_* = \frac{\lambda_1^2 + \lambda_2^2}{2}\overline{\beta}_0 + \frac{\lambda_1^2 - \lambda_2^2}{4}\left(\lambda_1^2\frac{\partial\overline{\beta}_0}{\partial\lambda_1} - \lambda_2^2\frac{\partial\overline{\beta}_0}{\partial\lambda_2}\right) - \frac{1}{\lambda_1^2\lambda_2^2}\left[\frac{\lambda_1^2 + \lambda_2^2}{2}\overline{\beta}_1 + \frac{\lambda_1^2 - \lambda_2^2}{4}\left(\lambda_1^2\frac{\partial\overline{\beta}_1}{\partial\lambda_1} - \lambda_2^2\frac{\partial\overline{\beta}_1}{\partial\lambda_2}\right)\right]. \tag{3.11}$$

Furthermore, from the elastic energy of an elastic solid isotropic and deformed in plane strain conditions, $\lambda_3 = 1$ and $\lambda_1 = 1/\lambda_2 > 1$, expressed as a function of principal stretches it is possible to obtain

$$T_1 - T_2 = \lambda_1\frac{\partial W}{\partial\lambda_1} - \lambda_2\frac{\partial W}{\partial\lambda_2} \tag{3.12}$$

and renaming $\lambda = \lambda_1 = 1/\lambda_2$ the following important and useful formulation valid for plane strain incompressible hyperelasticity is obtained

$$T_1 - T_2 = \lambda \frac{\partial W}{\partial \lambda}. \tag{3.13}$$

Using the definition of Jaumann derivative in the principal reference system and taking the material-time derivative of the spectral representation of the Cauchy stress, we have

$$\widehat{T}_{11} - \widehat{T}_{22} = \dot{T}_{11} - \dot{T}_{22}, \qquad \widehat{T}_{12} = \dot{T}_{12} + (T_1 - T_2)W_{12} \tag{3.14}$$

and introducing the incremental representation of the unit vectors v_1 and v_2 in the $1-2$ plane in terms of the incremental azimuthal angle θ

$$\widehat{T}_{11} - \widehat{T}_{22} = \frac{\lambda}{2}\frac{d(T_1 - T_2)}{d\lambda}(D_{11} - D_{22}), \qquad \widehat{T}_{12} = (T_1 - T_2)\frac{\lambda^4 + 1}{\lambda^4 - 1}D_{12}. \tag{3.15}$$

Comparing the Eqs. (3.15) and Eq. (3.9) another useful description for the two incremental moduli can be found

$$\mu = \frac{\lambda^4 + 1}{\lambda^4 - 1}\frac{T_1 - T_2}{2}, \qquad \mu_* = \frac{\lambda}{4}\frac{d(T_1 - T_2)}{d\lambda}. \tag{3.16}$$

At this point, assuming that the difference of the stress components $T_1 - T_2$ can be represented in a Taylor series expansion near the condition of the unstressed state

$$T_1 - T_2 \sim \frac{d(T_1 - T_2)}{d\lambda}|_{\lambda=1}(\lambda - 1) \tag{3.17}$$

that yields

$$\frac{\mu_*}{\mu} \sim \lambda, \tag{3.18}$$

showing that the material is incrementally isotropic at the unstressed state λ_1. The incremental constitutive equations for plane strain can be rewritten as

$$\dot{S}_{ji} = \dot{t}_{ij} = \mathbb{G}_{ijkl} v_{j,k} + \dot{p}\delta_{ij}, \qquad v_{i,i} = 0, \tag{3.19}$$

where v_i is the velocity and δ_{ij} is the Kronecker delta, and

$$\dot{p} = \frac{\dot{T}_1 + \dot{T}_2}{2} \tag{3.20}$$

measures the in-plane hydrostatic stress rate as related to the Cauchy stress rate. Tensor $\mathbb{G}$ is the elastic tensor

$$\mathbb{G}_{1111} = \mu_* - \frac{\sigma}{2} - p, \qquad \mathbb{G}_{1122} = -\mu_*, \qquad \mathbb{G}_{1112} = \mathbb{G}_{1121} = 0, \tag{3.21}$$

$$\mathbb{G}_{2211} = -\mu_*, \qquad \mathbb{G}_{2222} = \mu_* + \frac{\sigma}{2} - p, \qquad \mathbb{G}_{2212} = \mathbb{G}_{2221} = 0, \tag{3.22}$$

$$\mathbb{G}_{1212} = \mu + \frac{\sigma}{2}, \qquad \mathbb{G}_{1221} = \mathbb{G}_{2112} = \mu - p, \qquad \mathbb{G}_{2121} = \mu - \frac{\sigma}{2}, \tag{3.23}$$

with

$$\sigma = T_1 - T_2 \tag{3.24}$$

and

$$p = \frac{T_1 + T_2}{2}. \tag{3.25}$$

At the end, the final form of the incremental constitutive equations are derived in the useful form

$$\dot{t}_{11} = \mu(2\xi - k - \eta)v_{1,1} + \dot{p}, \tag{3.26}$$

$$\dot{t}_{22} = \mu(2\xi + k - \eta)v_{2,2} + \dot{p}, \tag{3.27}$$

$$\dot{t}_{12} = \mu\left[(1+k)v_{2,1} + (1-\eta)v_{1,2}\right], \tag{3.28}$$

$$\dot{t}_{21} = \mu\left[(1-\eta)v_{2,1} + (1-k)v_{1,2}\right], \tag{3.29}$$

where

$$\xi = \frac{\mu_*}{\mu}, \qquad \eta = \frac{p}{\mu} = \frac{T_1 + T_2}{2\mu}, \qquad k = \frac{T_1 - T_2}{2\mu} \tag{3.30}$$

are non-dimensional parameters that represent the ratio between incremental shear moduli, the dimensionless in-plane hydrostatic stress and the in-plane deviatoric stress.

3.3 General solution for elastic layers

Following the procedure presented in Biot (1965) and Bigoni (2012) for the mechanical problem related to the bifurcation of simple structures, the general solution of an incremental quasi-static problem can be expressed using a plane wave represetation

$$\psi = -\frac{1}{ic_1}\left[b_1 e^{ic_1\Omega_1 x_2} + b_2 e^{ic_1\Omega_2 x_2} + b_3 e^{ic_1\Omega_3 x_2} + b_4 e^{ic_1\Omega_4 x_2}\right] f(c_1 x_1) \tag{3.31}$$

where

- c_1 is the wavenumber of the bifurcated mode,
- Ω_i are the four roots of the general solution that depend on the regime in which the material is in terms of stress,
- $f(c_1 x_1)$ can be choose between:

$$e^{ic_1 x_i} \qquad cos(c_1 x_1) \qquad sin(c_1 x_1). \tag{3.32}$$

Furthermore, always starting from the definition of the stream function, the components of the incremental displacement are defined as

$$v_1 = \psi_{,2} \qquad v_2 = \psi_{,1}\,. \tag{3.33}$$

In this way, they assume the following form

$$v_1 = (-b_1\Omega_1 e^{ic_1\Omega_1 x_2} - b_2\Omega_2 e^{ic_1\Omega_2 x_2} - b_3\Omega_3 e^{ic_1\Omega_3 x_2} - b_4\Omega_4 e^{ic_1\Omega_4 x_2}) f(c_1, x_1) \tag{3.34}$$

$$v_2 = -i\left[b_1 e^{ic_1\Omega_1 x_2} + b_2 e^{ic_1\Omega_2 x_2} + b_3 e^{ic_1\Omega_3 x_2} + b_4 e^{ic_1\Omega_4 x_2}\right] f'(c_1, x_1) \tag{3.35}$$

where a prime denotes differentiation with respect to the argument. For example, if $f(c_1, x_1)$ is assumed equal to $e^{ic_1 x_i}$, the $f'(c_1, x_1)$ would be equal to $if(c_1, x_1)$. At this point, the incremental nominal stress can be calculated using the constitutive equation to yield

$$\begin{aligned}
\dot{t}_{11} &= c_1\mu(2\xi - k - \eta)\widehat{v}_1 f' + \dot{p},\\
\dot{t}_{22} &= -c_1\mu(2\xi + k - \eta)\widehat{v}_1 f' + \dot{p},\\
\dot{t}_{12} &= \mu\left[-c_1(1+k)\widehat{v}_2 + (1-\eta)\widehat{v}_{1,2}\right] f,\\
\dot{t}_{21} &= \mu\left[-c_1(1-\eta)\widehat{v}_2 + (1-k)\widehat{v}_{1,2}\right] f,
\end{aligned} \tag{3.36}$$

where

$$\widehat{v}_1 = -b_1\Omega_1 e^{ic_1\Omega_1 x_2} - b_2\Omega_2 e^{ic_1\Omega_2 x_2} - b_3\Omega_3 e^{ic_1\Omega_3 x_2} - b_4\Omega_4 e^{ic_1\Omega_4 x_2} \tag{3.37}$$

$$\widehat{v}_2 = -i\left[b_1 e^{ic_1\Omega_1 x_2} + b_2 e^{ic_1\Omega_2 x_2} + b_3 e^{ic_1\Omega_3 x_2} + b_4 e^{ic_1\Omega_4 x_2}\right] \tag{3.38}$$

$$\widehat{v}_{1,2} = -ic_1\left[b_1\Omega_1^2 e^{ic_1\Omega_1 x_2} + b_2\Omega_2^2 e^{ic_1\Omega_2 x_2} + b_3\Omega_3^2 e^{ic_1\Omega_3 x_2} + b_4\Omega_4^2 e^{ic_1\Omega_4 x_2}\right] \tag{3.39}$$

and, using the derivation proposed by Bigoni (2012) the rate of in-plane mean stress

$$\dot{p} = -c_1\mu \Big[(k+\Lambda)(\Omega_1 b_1 e^{ic_1\Omega_1 x_2} + \Omega_3 b_3 e^{ic_1\Omega_3 x_2}) + (k-\Lambda)(\Omega_2 b_2 e^{ic_1\Omega_2 x_2} + \Omega_4 b_4 e^{ic_1\Omega_4 x_2})\Big] f'. \quad (3.40)$$

Remembering the relations between Ω_i, the incremental nominal stress become

$$\begin{aligned} \dot{t}_{11} =& -c_1\mu\{(2\xi-\eta+\Lambda)\left[\Omega_1 b_1 e^{ic_1\Omega_1 x_2} + \Omega_3 b_3 e^{ic_1\Omega_3 x_2}\right] \\ &+ (2\xi-\eta-\Lambda)\left[\Omega_2 b_2 e^{ic_1\Omega_2 x_2} + \Omega_4 b_4 e^{ic_1\Omega_4 x_2}\right]\}f' \end{aligned} \quad (3.41)$$

$$\begin{aligned} \dot{t}_{22} =& c_1\mu\{(2\xi-\eta-\Lambda)\left[\Omega_1 b_1 e^{ic_1\Omega_1 x_2} + \Omega_3 b_3 e^{ic_1\Omega_3 x_2}\right] \\ &+ (2\xi-\eta+\Lambda)\left[\Omega_2 b_2 e^{ic_1\Omega_2 x_2} + \Omega_4 b_4 e^{ic_1\Omega_4 x_2}\right] \end{aligned} \quad (3.42)$$

$$\begin{aligned} \dot{t}_{12} =& ic_1\mu\{(1+k-(1-\eta)\Omega_1^2)\left[b_1 e^{ic_1\Omega_1 x_2} + b_3 e^{ic_1\Omega_3 x_2}\right] \\ &+ (1+k-(1-\eta)\Omega_2^2)\left[b_2 e^{ic_1\Omega_2 x_2} + b_4 e^{ic_1\Omega_4 x_2}\right]\}f \end{aligned} \quad (3.43)$$

$$\begin{aligned} \dot{t}_{21} =& ic_1\mu\{(2\xi-\eta+\Lambda)\left[b_1 e^{ic_1\Omega_1 x_2} + b_3 e^{ic_1\Omega_3 x_2}\right] \\ &+ (2\xi-\eta-\Lambda)\left[b_2 e^{ic_1\Omega_2 x_2} + b_4 e^{ic_1\Omega_4 x_2}\right]\}f \end{aligned} \quad (3.44)$$

Now, analyzing the various mechanical problems and identifying the correct incremental boundary conditions through the Eqs. (3.44), it is always possible to determine the trivial response for b_i with $i = 1, 2, 3, 4$.

Moreover, as reported before, c_1 plays the role of the wave number of the bifurcated field , whereas $2\pi/c_1$ represents the wavelenght of the bifurcation field.

3.4 Uniqueness and stability criteria in plane strain conditions and for incompressible elasticity

This section summeraizes the basic relations that are used to describe and investigate the problem related tio the uniqueness of the static incremrntla boundary- vaklue problem explaine in the Hill'theory (1957). Taking the appropriate specialization of the incremental equations that governe the quasi-static incremental deformations and restricting the analysis to

the case where incremental tractions $\dot{\boldsymbol{s}}$ are independent of the incremental solutions of the incremtnal boundary-value problem

$$\mathrm{Div}\,\dot{\boldsymbol{S}} + \dot{\boldsymbol{b}} = \boldsymbol{0}, \tag{3.45}$$

$$\dot{\boldsymbol{x}} = \dot{\boldsymbol{\xi}} \qquad \text{on} \qquad \partial\mathbb{B}_0^x, \tag{3.46}$$

$$\dot{\boldsymbol{S}}\boldsymbol{n}_0 = \dot{\boldsymbol{s}}_0 \qquad \text{on} \qquad \partial\mathbb{B}_0^\sigma. \tag{3.47}$$

Suppose that there exist two different solutions for the same incremental boundary-value problem in terms of velocity fields , $\dot{\boldsymbol{x}}_1$ and $\dot{\boldsymbol{x}}_2$, and in terms of corresponding stresses, $\dot{\boldsymbol{S}}_1$ and $\dot{\boldsymbol{S}}_2$. If $\Delta(\cdot) = (\cdot)_1 - (\cdot)_2$ denotes a difference of fields, it follows, considering that the body forces are independent of the incremental solutions, that

$$\mathrm{Div}\,\Delta\dot{\boldsymbol{S}} = \boldsymbol{0}, \tag{3.48}$$

$$\Delta\dot{\boldsymbol{x}} = 0 \qquad \text{on} \qquad \partial B_0^x, \tag{3.49}$$

$$\Delta\dot{\boldsymbol{S}}\boldsymbol{n}_0 = 0 \qquad \text{on} \qquad \partial B_0^\sigma. \tag{3.50}$$

Multiplying Eq. (3.48) by $\Delta\dot{\boldsymbol{S}}$ through the scalar product, integrating on the total volume of the body $\mathbb{B}_0$ and applying the divergence theorem

$$\int_{\partial B_0} \Delta\dot{\boldsymbol{S}} \cdot \Delta\dot{\boldsymbol{F}} = 0. \tag{3.51}$$

Hence, a sufficient condition that ensures uniqueness of the incrementla problem is

$$\int_{\partial B_0} \Delta\dot{\boldsymbol{S}} \cdot \Delta\dot{\boldsymbol{F}} > 0, \tag{3.52}$$

for all pairs of distinct incremental displacement fields consistent with the incremental boundary conditions. Consider now a loading path starting from a configuration where the exclusion condition, derive in Eq. (3.52) holds true and assuming that the integral becomes semi-definite, this means not $>$ but $\geq$ than zero, with equality holding for some $\dot{\boldsymbol{x}} \neq 0$. A bifurcation or limit load point has been encountered for some $\dot{\boldsymbol{x}} \neq 0$. This $\dot{\boldsymbol{x}}$ is termed an eigenmode, while thecritical configuration is a primary eigenstate, representing a bifurcation point on the deformation path. Configurations that satisfy $\dot{\boldsymbol{S}} \cdot \Delta\dot{\boldsymbol{F}} = 0$ for some $\dot{\boldsymbol{x}} \neq 0$ are called simply eigenstates. In the following chapter, and in detail in the Appendix B, it will present the effect of the introduction of an imperfect interface inside an elastic solid at the point of view of the definition of the uniqueness and stability criteria.

Chapter 4

Models for a shear band in a ductile material

Abstract A model of a shear band as a zero-thickness non-linear interface is proposed and tested using finite element simulations. An imperfection approach is used in this model where a shear band that is assumed to lie in a ductile matrix material (obeying von Mises plasticity with linear hardening), is present from the beginning of loading and is considered to be a zone in which yielding occurs before the rest of the matrix. This approach is contrasted with a perturbative approach, developed for a J2-deformation theory material, in which the shear band is modeled to emerge at a certain stage of a uniform deformation. Both approaches concur in showing that the shear bands (differently from cracks) propagate rectilinearly under shear loading and that a strong stress concentration should be expected to be present at the tip of the shear band, two key features in the understanding of failure mechanisms of ductile materials.

4.1 Introduction

When a ductile material is brought to an extreme strain state through a uniform loading process, the deformation may start to localize into thin and planar bands, often arranged in regular lattice patterns. This phenomenon is quite common and occurs in many materials over a broad range of scales: from the kilometric scale in the earth crust (Kirby, 1985), down to the nanoscale in metallic glass (Yang, 2005), see the examples

reported in Fig. 4.1.

After localization, unloading typically[1] occurs in the material outside the bands, while strain quickly evolves inside, possibly leading to final fracture (as in the examples shown in Fig. 4.2, where the crack lattice is the signature of the initial shear band network[2]) or to a progressive accumulation of deformation bands (as for instance in the case of the drinking straws, or of the iron meteorite, or of the uPVC sample shown in Fig. 4.1, or in the well-known case of granular materials, where fracture is usually absent and localization bands are made up of material at a different relative density, Gajo et al. 2004).

It follows from the above discussion that as strain localization represents a prelude to failure of ductile materials, its mechanical understanding paves the way to the innovative use of materials in extreme mechanical conditions. For this reason shear bands have been the focus of a thorough research effort. In particular, research initiated with pioneering works by Hill (1962), Nadai (1950), Mandel (1962), Prager (1954) Rice (1977), Thomas (1961) and developed –from theoretical point of view– into two principal directions, namely, the dissection of the specific constitutive features responsible for strain localization in different materials (for instance as related to the microstructure, Bacigalupo and Gambarotta, 2013; Danas and Ponte Castaneda, 2012; Tvergaard, 2014) and the struggle for the overcoming of difficulties connected with numerical approaches (reviews have been given by Needleman and Tvergaard, 1983; Petryk, 1997). Although these problems are still not exhausted, surprisingly, the most important questions have only marginally been approached and are therefore still awaiting explanation. These are as follows:

i.) Why are shear bands a preferred mode of failure for ductile materials? ii.) Why do shear bands propagate rectilinearly under mode II, while cracks do not? iii.) How does a shear band interact with a crack or with a rigid inclusion? iv.) Does a stress concentration exist at a shear

[1]For granular materials, there are cases in which unloading occurs inside the shear band, as shown by Gajo et al. (2004).

[2]The proposed explanation for the crack patterns shown in Fig. 4.2 releases on the fact that the fracture network has formed during the plastic evolution of a ductile homogeneously deformed material. Other explanations may be related to bonding of an external layer to a rigid substrate (Peron et al. 2013), or to surface instability (Boulogne et al. 2015; Destrade and Merodio, 2011), or to instabilities occurring during shear (Ciarletta et al. 2013; Destrade et al. 2008).

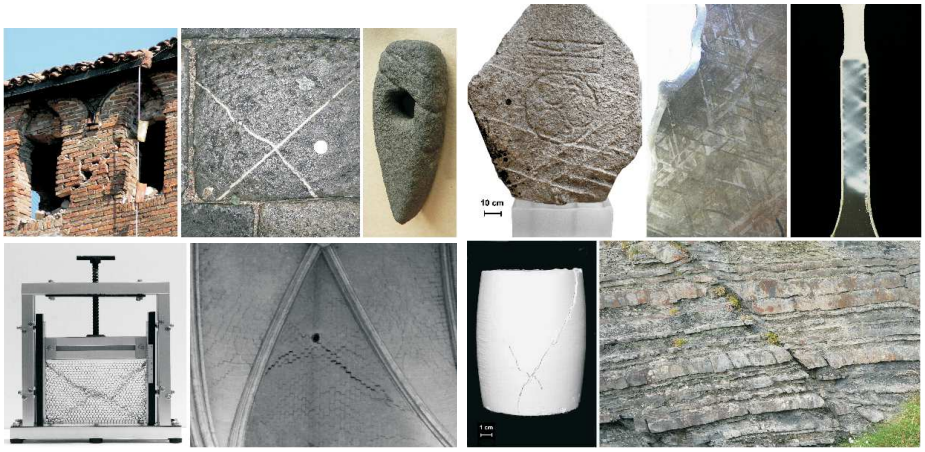

Figure 4.1: Examples of strain localization. From left to right, starting from the upper part: A merlon in the Finale Emilia castle failed (during the Emilia earthquake on May 20, 2012) in compression with a typical 'X-shaped' deformation band pattern (bricks are to be understood here as the microstructure of a composite material). A sedimentary rock with the signature of an 'X-shaped' localization band (infiltrated with a different mineral after formation). A stone axe from a British Island (Museum of Edinburgh) evidencing two parallel localization bands and another at a different orientation. A runestone (Museum of Edinburgh) with several localized deformation bands, forming angles of approximatively 45° between each other. A polished and etched section of an iron meteorite showing several alternate bands of kamacite and taenite. Deformation bands in a strip of unplasticized poly(vinyl chloride) (uPVC) pulled in tension and eventually evolving into a necking. An initially regular hexagonal disposition of drinking straws subject to uniform uniaxial strain has evolved into an 'X-shaped' localization pattern. A fracture prevails on a regularly distributed network of cracks in a vault of the Amiens dome. 'X-shaped' localization bands in a kaolin sample subject to vertical compression and lateral confining pressure. A thin, isolated localization band in a sedimentary layered rock (Silurian formation near Aberystwyth).

Figure 4.2: Regular patterns of localized cracks as the signature of strain localization lattices. From left to right: Dried mud; Lava cracked during solidification (near Amboy crater); Bark of a maritime pine (Pinus pinaster); Cracks in a detail of a painting by J. Provost ('Saint Jean-Baptiste', Valenciennes, Musée des Beaux Arts).

band tip? v.) How does a shear band behave under dynamic conditions?

The only systematic[3] attempt to solve these problems seems to have been a series of works by Bigoni and co-workers, based on the perturbative approach to shear bands (Argani et al. 2014; 2013; Bigoni and Capuani, 2002; 2005; Piccolroaz et al. 2006). In fact problems (i.), (ii.), and (iv.) were addressed in (Bigoni and Dal Corso, 2008 and Dal Corso and Bigoni, 2010), problem (iii.) in (Dal Corso et al. 2008; Bigoni et al. 2008; Dal Corso and Bigoni, 2009), and (v.) in (Bigoni and Capuani, 2005).

The purpose of the present article is to present a model of a shear band as a zero-thickness interface and to rigorously motivate this as the asymptotic behaviour of a thin layer of material, which is extremely compliant in shear (Section 4.2). Once the shear band model has been developed, it is used (in Section 4.3) to demonstrate two of the above-listed open problems, namely (ii.) that a shear band grows rectilinearly under mode II remote loading in a material deformed near to failure and (iv.) to estimate the stress concentration at the shear band tip. In particular, a pre-existing shear band is considered to lie in a matrix as a thin zone of material with properties identical to the matrix, but lower yield stress.

[3]Special problems of shear band propagation in geological materials have been addressed by Puzrin and Germanovich (2005) and Rice (1973).

This is an imperfection, which remains neutral until the yield is reached in the shear band.[4] The present model is based on an imperfection approach and shares similarities to that pursued by Abeyaratne and Triantafyllidis (1981) and Hutchinson and Tvergaard (1981), so that it is essentially different from a perturbative approach, in which the perturbation is imposed at a certain stage of a uniform deformation process.[5]

4.2 Asymptotic model for a thin layer of highly compliant material embedded in a solid

A shear band, inside a solid block of dimension H, is modeled as a thin layer of material (of semi-thickness h, with $h/H \ll 1$) yielding at a uniaxial stress $\sigma_Y^{(s)}$, which is lower than that of the surrounding matrix $\sigma_Y^{(m)}$, Fig. 4.3. Except for the yield stress, the material inside and outside the layer is described by the same elastoplastic model, namely, a von Mises plasticity with associated flow rule and linear hardening, defined through the elastic constants, denoted by the Young modulus E and Poisson's ratio ν, and the plastic modulus E_p, see Fig. 4.3b.

At the initial yielding, the material inside the layer (characterized by a low hardening modulus $E_{ep} = EE_p/(E + E_p)$) is much more compliant than the material outside (characterized by an elastic isotropic response E).

For $h/H \ll 1$, the transmission conditions across the layer imply the continuity of the tractions, $\boldsymbol{t} = [t_{21}, t_{22}]^T$, which can be expressed in the asymptotic form

$$[\![t_{21}]\!] = O(h), \quad [\![t_{22}]\!] = O(h), \tag{4.1}$$

where $[\![\cdot]\!]$ denotes the jump operator. The jump in displacements, $[\![\boldsymbol{u}]\!] = [[\![u_1]\!], [\![u_2]\!]]^T$, across the layer is related to the tractions at its boundaries through the asymptotic relations (Mishuris et al., 2013; Sonato et al.,

[4] A different approach to investigate shear band evolution is based on the exploitation of phase-field models (Zheng and Li, 2009), which has been often used for brittle fracture propagation (Miehe et al. 2010).

[5] To highlight the differences and the analogies between the two approaches, the incremental strain field induced by the emergence of a shear band of finite length (modelled as a sliding surface) is determined for a J_2-deformation theory material and compared with finite element simulations in which the shear band is modelled as a zero-thickness layer of compliant material.

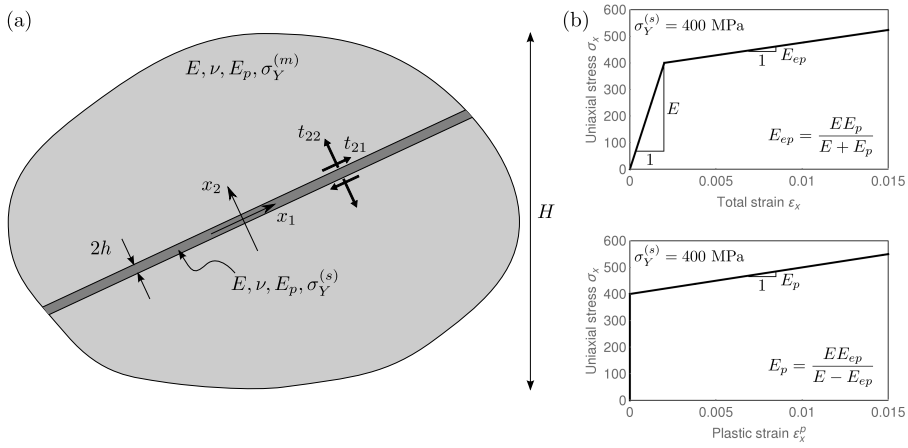

Figure 4.3: (a) A shear band inside a ductile material modeled as a thin layer of highly compliant material ($E_{ep}/E \ll 1$) embedded in a material block characterized by a dimension H, such that $h/H \ll 1$; both materials obey the same von Mises plasticity model represented by the uniaxial stress behaviour reported in (b), but having a different yield stress (lower inside than outside the shear band).

2015)

$$t_{21}(\llbracket u_1 \rrbracket, \llbracket u_2 \rrbracket) = \frac{E_p\sqrt{3\llbracket u_1 \rrbracket^2 + 4\llbracket u_2 \rrbracket^2} + 6h\sigma_Y^{(s)}}{(3E + 2(1+\nu)E_p)\sqrt{3\llbracket u_1 \rrbracket^2 + 4\llbracket u_2 \rrbracket^2}} \frac{E\llbracket u_1 \rrbracket}{2h} + O(h), \tag{4.2}$$

$$t_{22}(\llbracket u_1 \rrbracket, \llbracket u_2 \rrbracket) = \frac{(E + 2(1-\nu)E_p)\sqrt{3\llbracket u_1 \rrbracket^2 + 4\llbracket u_2 \rrbracket^2} + 8h(1-2\nu)\sigma_Y^{(s)}}{(1-2\nu)(3E + 2(1+\nu)E_p)\sqrt{3\llbracket u_1 \rrbracket^2 + 4\llbracket u_2 \rrbracket^2}} \frac{E\llbracket u_2 \rrbracket}{2h} + \\ + O(h), \tag{4.3}$$

involving the semi-thickness h of the shear band, which enters the formulation as a *constitutive parameter for the zero-thickness interface model* and introduces a *length scale*. Note that, by neglecting the remainder $O(h)$, Eqs. (4.2) and (4.3) define nonlinear relationships between tractions and jump in displacements.

The time derivative of Eqs. (4.2) and (4.3) yields the following asymptotic relation between incremental quantities

$$\dot{\boldsymbol{t}} \sim \left[\frac{1}{h}\boldsymbol{K}_{-1} + \boldsymbol{K}_0(\llbracket u_1 \rrbracket, \llbracket u_2 \rrbracket)\right] \llbracket \dot{\boldsymbol{u}} \rrbracket, \tag{4.4}$$

where the two stiffness matrices $\boldsymbol{K}_{-1}$ and $\boldsymbol{K}_0$ are given by

$$\boldsymbol{K}_{-1} = \frac{E}{2(3E + 2(1+\nu)E_p)} \begin{bmatrix} E_p & 0 \\ 0 & \dfrac{E + 2(1-\nu)E_p}{1-2\nu} \end{bmatrix}, \tag{4.5}$$

$$\boldsymbol{K}_0 = \frac{12E\sigma_Y^{(s)}}{(3E + 2(1+\nu)E_p)(3[\![u_1]\!]^2 + 4[\![u_2]\!]^2)^{3/2}} \begin{bmatrix} [\![u_2]\!]^2 & -[\![u_1]\!][\![u_2]\!] \\ -[\![u_1]\!][\![u_2]\!] & [\![u_1]\!]^2 \end{bmatrix}, \tag{4.6}$$

Assuming now a perfectly plastic behaviour, $E_p = 0$, in the limit $h/H \to 0$ the condition

$$[\![u_2]\!] = 0 \tag{4.7}$$

is obtained, so that the incremental transmission conditions (4.4) can be approximated to the leading order as

$$\dot{\boldsymbol{t}} \sim \frac{1}{h}\boldsymbol{K}_{-1}[\![\dot{\boldsymbol{u}}]\!]. \tag{4.8}$$

Therefore, when the material inside the layer is close to the perfect plasticity condition, the incremental conditions assume the limit value

$$\dot{t}_{21} = 0, \quad [\![\dot{u}_2]\!] = 0, \tag{4.9}$$

which, together with the incremental version of eq. $(4.1)_2$, namely,

$$[\![\dot{t}_{22}]\!] = 0, \tag{4.10}$$

correspond to the incremental boundary conditions proposed in Bigoni and Dal Corso (2008) to define a pre-existing shear band of null thickness.

The limit relations (4.9) and (4.10) motivate the use of the imperfect interface approach (Mishuris, 2004; 2001; Mishuris and Ochsner, 2005; 2007; Mishuris and Kuhn, 2001; Antipov et al. 2001; Bigoni et al., 1998) for the modelling of shear band growth in a ductile material. A computational model, in which the shear bands are modelled as interfaces, is presented in the next section.

4.3 Numerical simulations

Two-dimensional plane-strain finite element simulations are presented to show the effectiveness of the above-described asymptotic model for a

thin and highly compliant layer in modelling a shear band embedded in a ductile material. Specifically, we will show that the model predicts rectilinear propagation of a shear band under simple shear boundary conditions and it allows the investigation of the stress concentration at the shear band tip.

The geometry and material properties of the model are shown in Fig. 4.4, where a rectangular block of edges H and $L \geq H$ is subject to boundary conditions consistent with a simple shear deformation, so that the lower edge of the square domain is clamped, the vertical displacements are constrained along the vertical edges and along the upper edge, where a constant horizontal displacement u_1 is prescribed. The domain is made of a ductile material and contains a thin ($h/H \ll 1$) and highly compliant ($E_{ep}/E \ll 1$) layer of length $H/2$ and thickness $2h = 0.01$ mm, which models a shear band. The material constitutive behaviour is described by an elastoplastic model based on linear isotropic elasticity ($E = 200000$ MPa, $\nu = 0.3$) and von Mises plasticity with linear hardening (the plastic modulus is denoted by E_p). The uniaxial yield stress $\sigma_Y^{(m)}$ for the matrix material is equal to 500 MPa, whereas the layer is characterized by a lower yield stress, namely, $\sigma_Y^{(s)} = 400$ MPa.

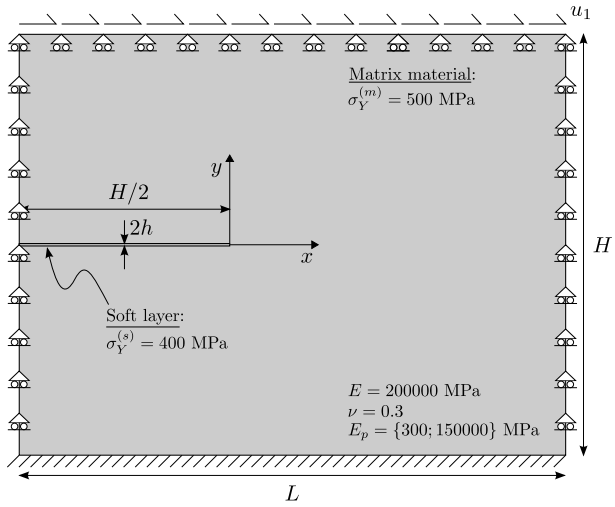

Figure 4.4: Geometry of the model, material properties and boundary conditions (that would correspond to a simple shear deformation in the absence of the shear band). The horizontal displacement u_1 is prescribed at the upper edge of the domain.

The layer remains neutral until yielding, but, starting from that stress level, it becomes a material inhomogeneity, being more compliant (because its response is characterized by E_{ep}) than the matrix (still in the elastic regime and thus characterized by E). The layer can be representative of a pre-existing shear band and can be treated with the zero-thickness interface model, Eqs. (4.2) and (4.3). This zero-thickness interface was implemented in the ABAQUS finite element software[6] through cohesive elements, equipped with the traction-separation laws, Eqs. (4.2) and (4.3), by means of the user subroutine UMAT. An interface, embedded into the cohesive elements, is characterized by two dimensions: a geometrical and a constitutive thickness. The latter, $2h$, exactly corresponds to the constitutive thickness involved in the model for the interface (4.2) and (4.3), while the former, denoted by $2h_g$, is related to the mesh dimension in a way that the results become independent of this parameter, in the sense that a mesh refinement yields results converging to a well-defined solution.

We consider two situations. In the first, we assume that the plastic modulus is $E_p = 150000$ MPa (both inside and outside the shear band), so that the material is in a state far from a shear band instability (represented by loss of ellipticity of the tangent constitutive operator, occurring at $E_p = 0$) when at yield. In the second, we assume that the material is prone to a shear band instability, though still in the elliptic regime, so that E_p (both inside and outside the shear band) is selected to be 'sufficiently small', namely, $E_p = 300$ MPa. The pre-existing shear band is therefore employed as an imperfection triggering shear strain localization when the material is still inside the region, but close to the boundary, of ellipticity.

4.3.1 Description of the numerical model

With reference to a square block ($L = H = 10$ mm) containing a pre-existing shear band with constitutive thickness $h = 0.005$ mm, three different meshes were used, differing in the geometrical thickness of the interface representing the pre-existing shear band (see Fig. 4.5 where the shear band is highlighted with a black line), namely, $h_g = \{0.05; 0.005; 0.0005\}$ mm corresponding to coarse, fine, and ultra-fine meshes.

[6] ABAQUS Standard Ver. 6.13 has been used, available on the AMD Opteron cluster Stimulus at UniTN.

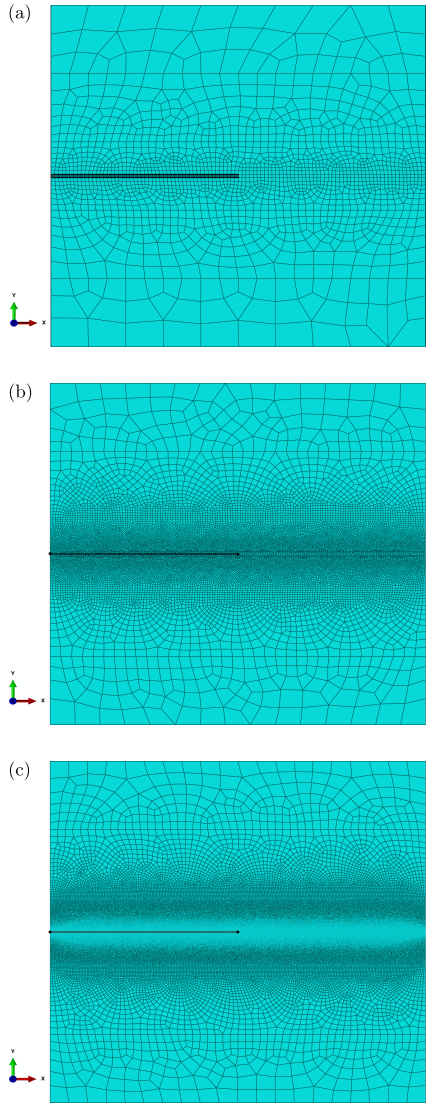

Figure 4.5: The three meshes used in the analysis to simulate a shear band (highlighted in black) in a square solid block ($L = H = 10$ mm). The shear band is represented in the three cases as an interface with the same constitutive thickness $h = 0.005$ mm, but with decreasing geometric thickness h_g; (a) coarse mesh (1918 nodes, 1874 elements, $h_g = 0.05$ mm); (b) fine mesh (32079 nodes, 31973 elements, $h_g = 0.005$ mm); (c) ultra-fine mesh (1488156 nodes, 1487866 elements, $h_g = 0.0005$ mm)

The three meshes were generated automatically using the mesh generator available in ABAQUS. In order to have increasing mesh refinement from the exterior (upper and lower parts) to the interior (central part) of the domain, where the shear band is located, and to ensure the appropriate element shape and size according to the geometrical thickness $2h_g$, the domain was partitioned into rectangular subdomains with increasing mesh seeding from the exterior to the interior. Afterwards, the meshes were generated by employing a free meshing technique with quadrilateral elements and the advancing front algorithm.

The interface that models the shear band is discretized using 4-node two-dimensional cohesive elements (COH2D4), while the matrix material is modelled using 4-node bilinear, reduced integration with hourglass control (CPE4R).

It is important to note that the constitutive thickness used for traction-separation response is always equal to the actual size of the shear band $h = 0.005$ mm, whereas the geometric thickness h_g, defining the height of the cohesive elements, is different for the three different meshes. Consequently, all the three meshes used in the simulations correspond to the same problem in terms of both material properties and geometrical dimensions (although the geometric size of the interface is different), so that the results have to be, and indeed will be shown to be, mesh independent.[7]

4.3.2 Numerical results

Results (obtained using the fine mesh, Fig. 4.5b) in terms of the shear stress component σ_{12} at different stages of a deformation process for the boundary value problem sketched in Fig. 4.4 are reported in Figs. 4.6 and 4.7.

In particular, Fig. 4.6 refers to a matrix with high plastic modulus, $E_p = 150000$ MPa, so that the material is far from the shear band formation threshold. The upper limit of the contour levels was set to the value $\sigma_{12} = 500/\sqrt{3} \backsimeq 288.68$ MPa, corresponding to the yielding stress of the matrix material. As a result, the grey zone in the figure represents the

[7] Note that, in the case of null hardening, mesh dependency may occur in the simulation of shear banding nucleation and propagation (Loret and Prevost, J.H., 1991; 1993; Needleman, 1988). This numerical issue can be avoided by improving classical inelastic models through the introduction of characteristic length-scales (Dal Corso and Willis, 2011; Lapovok et al. 2009).

material at yielding, whereas the material outside the grey zone is still in the elastic regime. Three stages of deformation are shown, corresponding to: the initial yielding of the matrix material (left), the yielding zone occupying approximately one half of the space between the shear band tip and the right edge of the domain (centre), and the yielding completely linking the tip of the shear band to the boundary (right). Note that the shear band, playing the role of a material imperfection, produces a stress concentration at its tip. However, the region of high stress level rapidly grows and diffuses in the whole domain. At the final stage, shown in Fig. 4.6c, almost all the matrix material is close to yielding.

Fig. 4.7 refers to a matrix with low plastic modulus, $E_p = 300$ MPa, so that the material is close (but still in the elliptic regime) to the shear band formation threshold ($E_p = 0$). Three stages of deformation are shown, from the condition of initial yielding of the matrix material near the shear band tip (left), to an intermediate condition (centre), and finally to the complete yielding of a narrow zone connecting the shear band tip to the right boundary (right). In this case, where the material is prone to shear band localization, the zone of high stress level departs from the shear band tip and propagates towards the right. This propagation occurs in a highly concentrated narrow layer, rectilinear, and parallel to the pre-existing shear band. At the final stage of deformation, shown in Fig. 4.7c, the layer of localized shear has reached the boundary of the block.

Results in terms of the shear strain component γ_{12}, for both cases of material far from, and close to shear band instability are reported in Figs. 4.8 and 4.9, respectively. In particular, Fig. 4.8 shows contour plots of the shear deformation γ_{12} for the case of a material far from the shear band instability ($E_p = 150000$ MPa) at the same three stages of deformation as those reported in Fig. 4.6. Although the tip of the shear band acts as a strain raiser, the contour plots show that the level of shear deformation is high and remains diffused in the whole domain.

Fig. 4.9 shows contour plots of the shear deformation γ_{12} for the case of a material close to the shear band instability ($E_p = 300$ MPa), at the same three stages of deformation as those reported in Fig. 4.7. It is noted that the shear deformation is localized along a rectilinear path ahead of the shear band tip, confirming results that will be reported later with the perturbation approach (Section 4.4).

The shear deformation γ_{12} and the shear stress σ_{12} along the x-axis

containing the pre-existing shear band for the case of a material close to strain localization, $E_p = 300$ MPa, are shown in Fig. 4.10, upper and lower parts, respectively. Results are reported for the three meshes, coarse, fine and ultra-fine (Fig. 4.5) and at the same three stages of deformation as those shown in Figs. 4.7 and 4.9. The results appear to be mesh independent, meaning that the solution converges as the mesh is more and more refined.

The deformation process reported in Figs. 4.7, 4.9, and 4.10 can be described as follows. After an initial homogeneous elastic deformation (not shown in the figure), in which the shear band remains neutral (since it shares the same elastic properties with the matrix material), the stress level reaches $\sigma_{12} = 400/\sqrt{3} \backsimeq 230.9$ MPa, corresponding to the yielding of the material inside the shear band. Starting from this point, the pre-existing shear band is activated, which is confirmed by a high shear deformation γ_{12} and a stress level above the yield stress inside the layer, -5 mm $< x < 0$ (left part of Fig. 4.10). The activated shear band induces a strain localization and a stress concentration at its tip, thus generating a zone of material at yield, which propagates to the right (central part of Fig. 4.10) until collapse (right part of Fig. 4.10).

In order to appreciate the strain and stress concentration at the shear band tip, a magnification of the results shown in Fig. 4.10 in the region -0.2 mm $< x < 0.2$ mm is presented in Fig. 4.11. Due to the strong localization produced by the shear band, only the ultra-fine mesh is able to capture accurately the strain and stress raising (blue solid curve), whereas the coarse and fine meshes smooth over the strain and stress levels (red dotted and green dashed curves, respectively). The necessity of a ultra-fine mesh to capture details of the stress/strain fields is well-known in computational fracture mechanics, where special elements (quarter-point or extended elements) have been introduced to avoid the use of these ultra-fine meshes at corner points.

For the purpose of a comparison with an independent and fully numerical representation of the shear band, a finite element simulation was also been performed, using standard continuum elements (CPE4R) instead of cohesive elements (COH2D4) inside the layer. This simulation is important to assess the validity of the asymptotic model of the layer presented in Sec. 4.2. In this simulation, reported in Fig. 4.12, the layer representing the shear band is a 'true' layer of a given and finite thickness,

thus influencing the results (while these are independent of the geometrical thickness $2h_g$ of the cohesive elements, when the constitutive thickness $2h$ is the same). Therefore, only the fine mesh, shown in Fig. 4.5b, was used, as it corresponds to the correct size of the shear band. The coarse mesh (Fig. 4.5a) and the ultra-fine mesh (Fig. 4.5c) would obviously produce different results, corresponding respectively to a thicker or thinner layer. Results pertaining to the asymptotic model, implemented into the traction-separation law for the cohesive elements COH2D, are also reported in the figure (red solid curve) and are spot-on with the results obtained with a fully numerical solution employing standard continuum elements CPE4R (blue dashed curve).

A mesh of the same size as that previously called 'fine' was used to perform a simulation of a rectangular block ($H = 10$ mm, $L = 4H = 40$ mm) made up of a material close to shear band instability ($E_p = 300$ MPa) and containing a shear band (of length $H/2 = 5$ mm and constitutive thickness $2h = 0.01$ mm). Results are presented in Fig. 4.13. In parts (a) and (b) (the latter is a detail of part a) of this figure the overall response curve is shown of the block in terms of average shear stress $\bar{\sigma}_{12} = T/L$ (T denotes the total shear reaction force at the upper edge of the block) and average shear strain $\bar{\gamma}_{12} = u_1/H$. In part (c) of the figure contour plots of the shear deformation γ_{12} are reported at different stages of deformation. It is clear that the deformation is highly focused along a rectilinear path emanating from the shear band tip, thus demonstrating the tendency of the shear band towards rectilinear propagation under shear loading.

Finally, the incremental shear strain (divided by the mean incremental shear strain) has been reported along the x-axis in Fig. 4.14, at the two stages of deformation considered in Fig. 4.10 and referred there as (a) and (c). These results, which have been obtained with the fine mesh, show that a strong incremental strain concentration develops at the shear band tip and becomes qualitatively similar to the square-root singularity found in the perturbative approach.

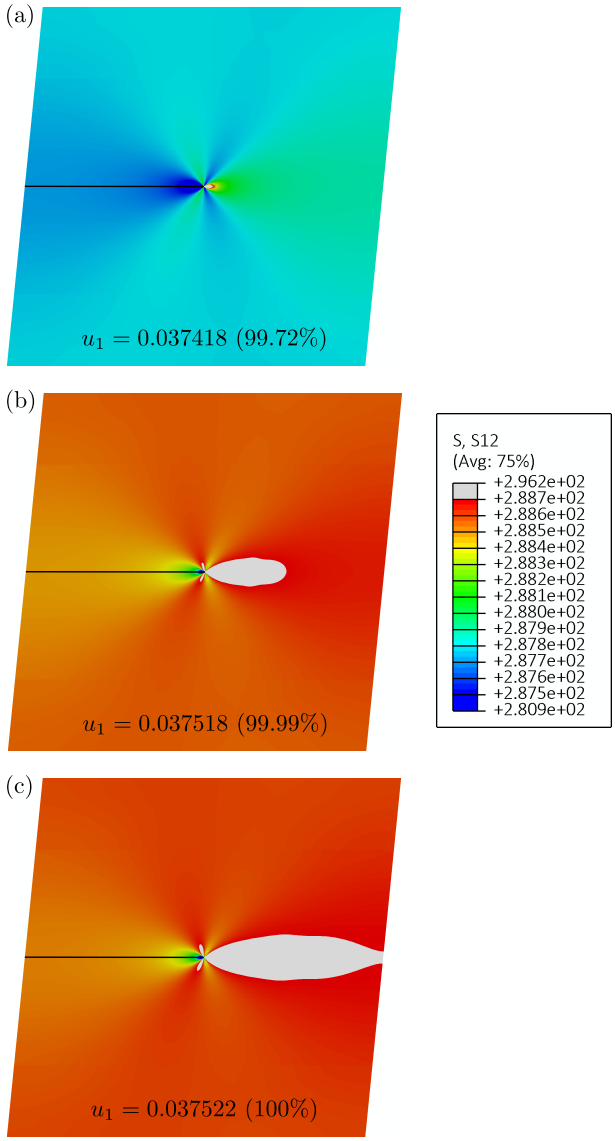

Figure 4.6: Contour plots of the shear stress σ_{12} for the case of material far from shear band instability ($E_p = 150000$ MPa). The grey region corresponds to the material at yielding $\sigma_{12} \geq 500/\sqrt{3} \backsimeq 288.68$ MPa. Three different stages of deformation are shown, corresponding to a prescribed displacement at the upper edge of the square domain $u_1 = 0.037418$ mm (a), $u_1 = 0.037518$ mm (b), $u_1 = 0.037522$ mm (c). The displacements in the figures are amplified by a deformation scale factor of 25 and the percentages refer to the final displacement.

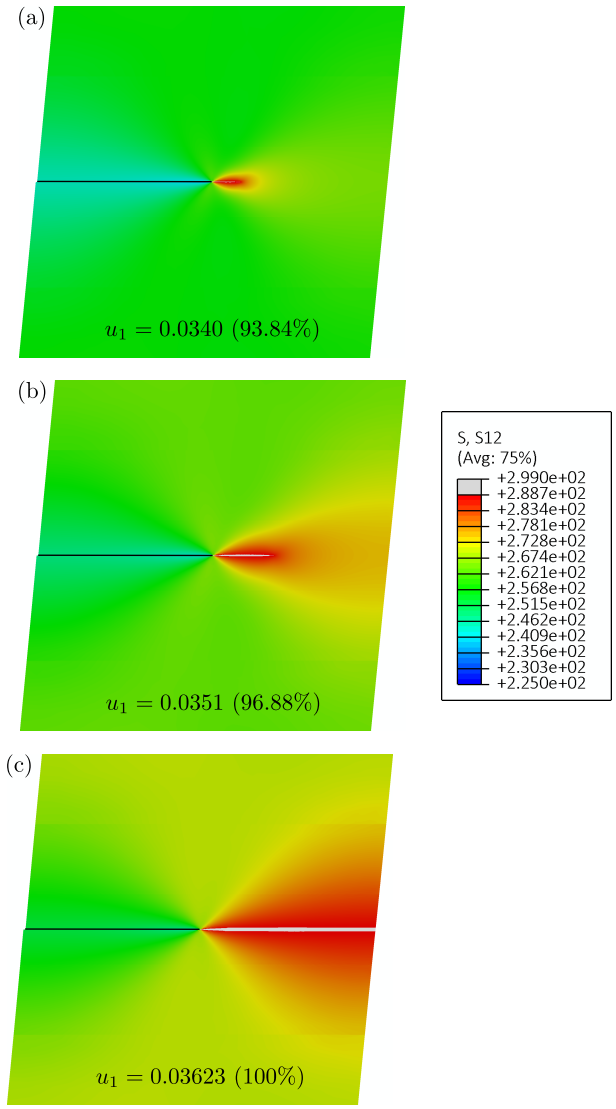

Figure 4.7: Contour plots of the shear stress σ_{12} for the case of material close to shear band instability ($E_p = 300$ MPa). The grey region corresponds to the material at yielding $\sigma_{12} \geq 500/\sqrt{3}$. Three different stages of deformation are shown, corresponding to a prescribed displacement at the upper edge of the square domain $u_1 = 0.0340$ mm (a), $u_1 = 0.0351$ mm (b), $u_1 = 0.03623$ mm (c). The displacements in the figures are amplified by a deformation scale factor of 27.

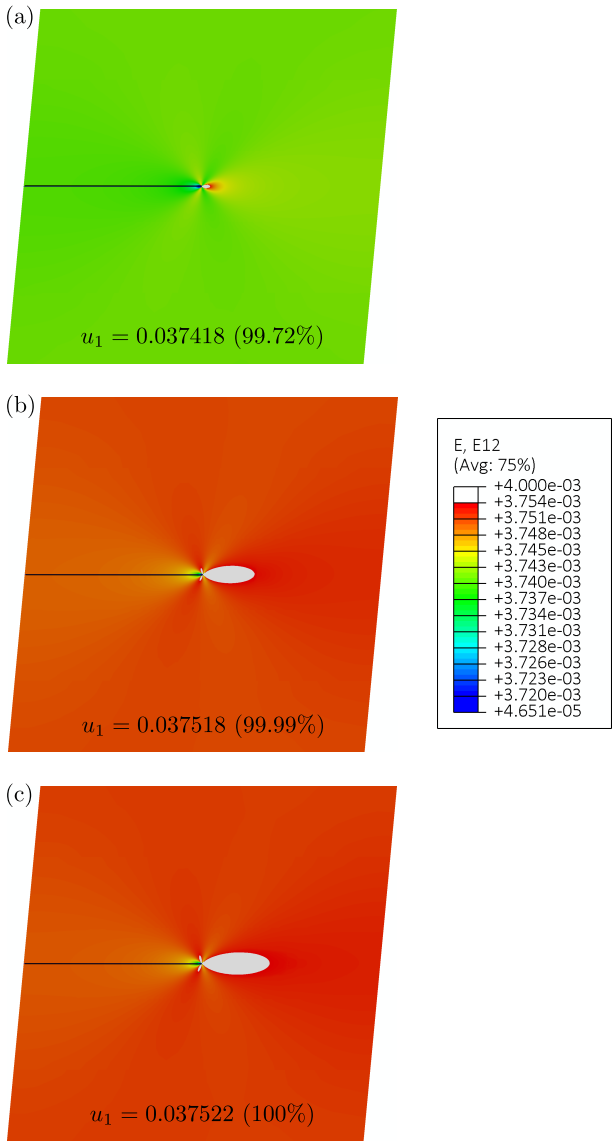

Figure 4.8: Contour plots of the shear deformation γ_{12} for the case of material far from shear band instability ($E_p = 150000$ MPa). Three different stages of deformation are shown, corresponding to a prescribed displacement at the upper edge of the square domain $u_1 = 0.037418$ mm (a), $u_1 = 0.037518$ mm (b), $u_1 = 0.037522$ mm (c). The displacements in the figures are amplified by a deformation scale factor of 25.

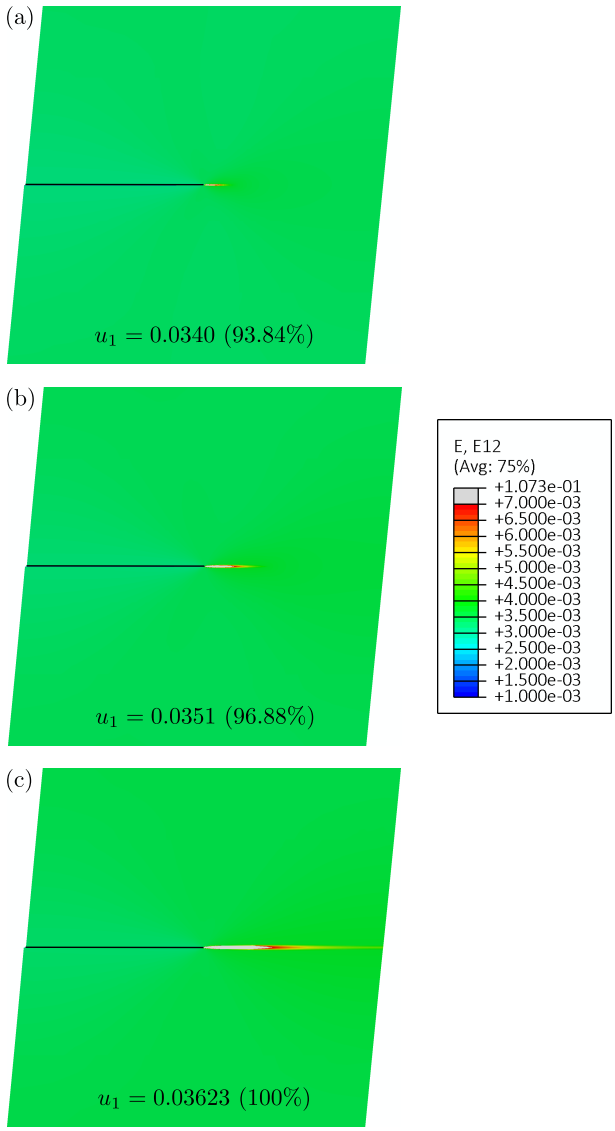

Figure 4.9: Contour plots of the shear deformation γ_{12} for the case of material close to shear band instability ($E_p = 300$ MPa). Three different stages of deformation are shown, corresponding to a prescribed displacement at the upper edge of the square domain $u_1 = 0.0340$ mm (a), $u_1 = 0.0351$ mm (b), $u_1 = 0.03623$ mm (c). The displacements in the figures are amplified by a deformation scale factor of 27.

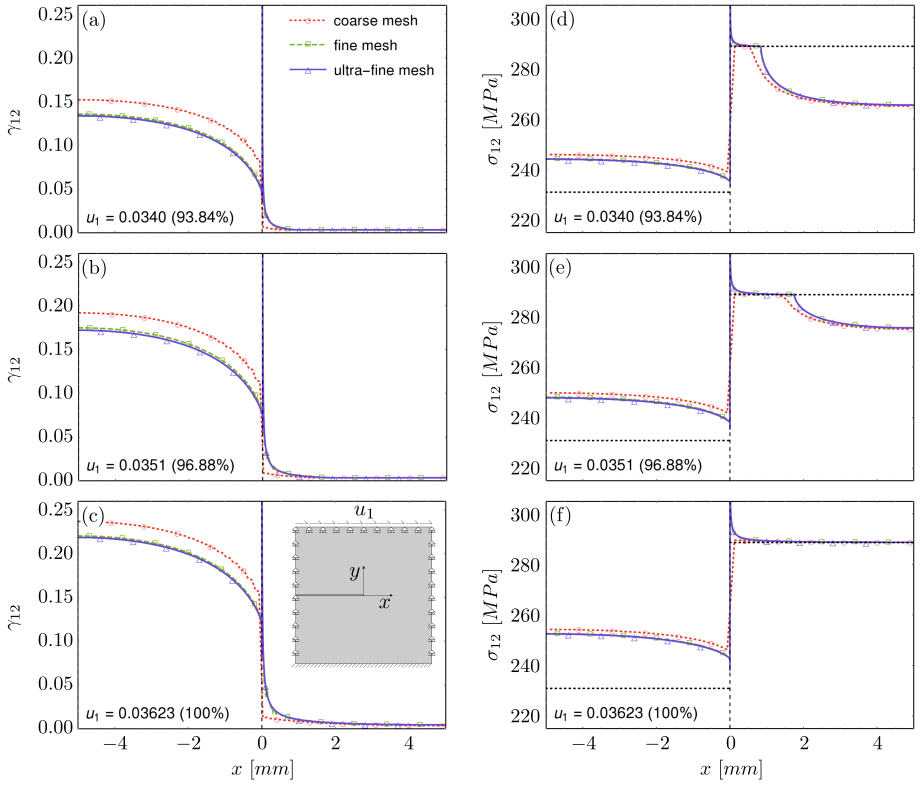

Figure 4.10: Shear deformation γ_{12} (upper part) and shear stress σ_{12} (lower part) along the x-axis containing the pre-existing shear band for the case of a material close to a shear band instability $E_p = 300$ MPa. The black dotted line, in the bottom part of the figure, indicates the yield stress level, lower inside the pre-existing shear band than that in the outer domain. Three different stages of deformation are shown, corresponding to a prescribed displacement at the upper edge of the square domain $u_1 = 0.0340$ mm (left), $u_1 = 0.0351$ mm (center), $u_1 = 0.03623$ mm (right).

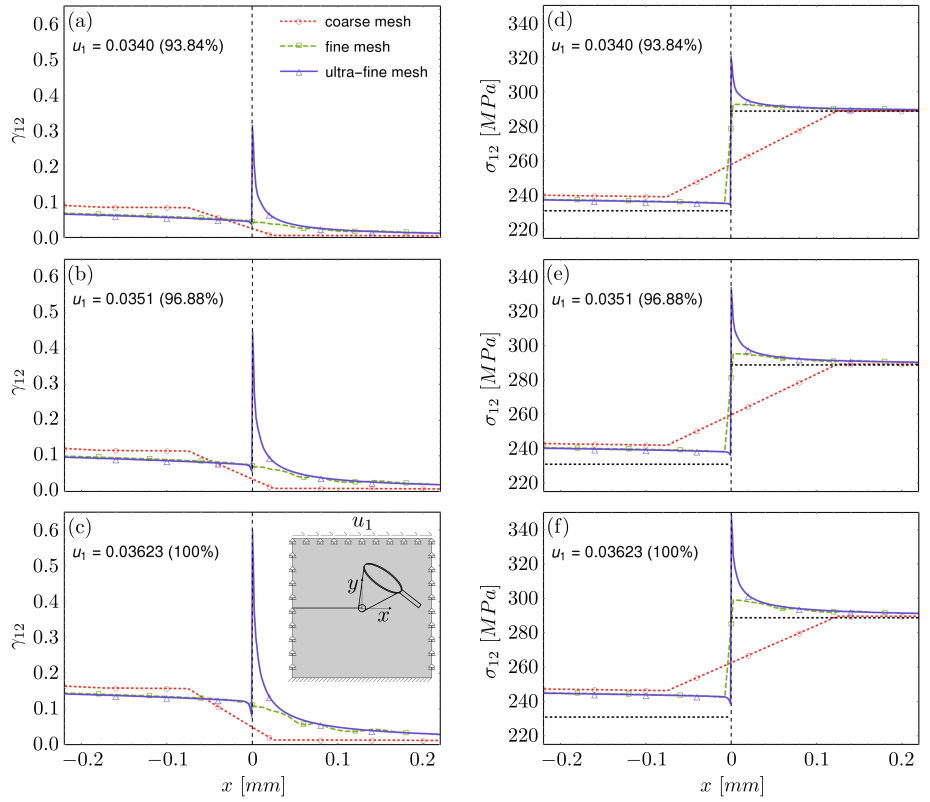

Figure 4.11: Shear and stress concentration at the shear band tip. Shear deformation γ_{12} (upper part) and shear stress σ_{12} (lower part) along the x-axis containing the pre-existing shear band for the case of a material close to a shear band instability $E_p = 300$ MPa. Three different stages of deformation are shown, corresponding to a prescribed displacement at the upper edge of the square domain $u_1 = 0.0340$ mm (left), $u_1 = 0.0351$ mm (center), $u_1 = 0.03623$ mm (right).

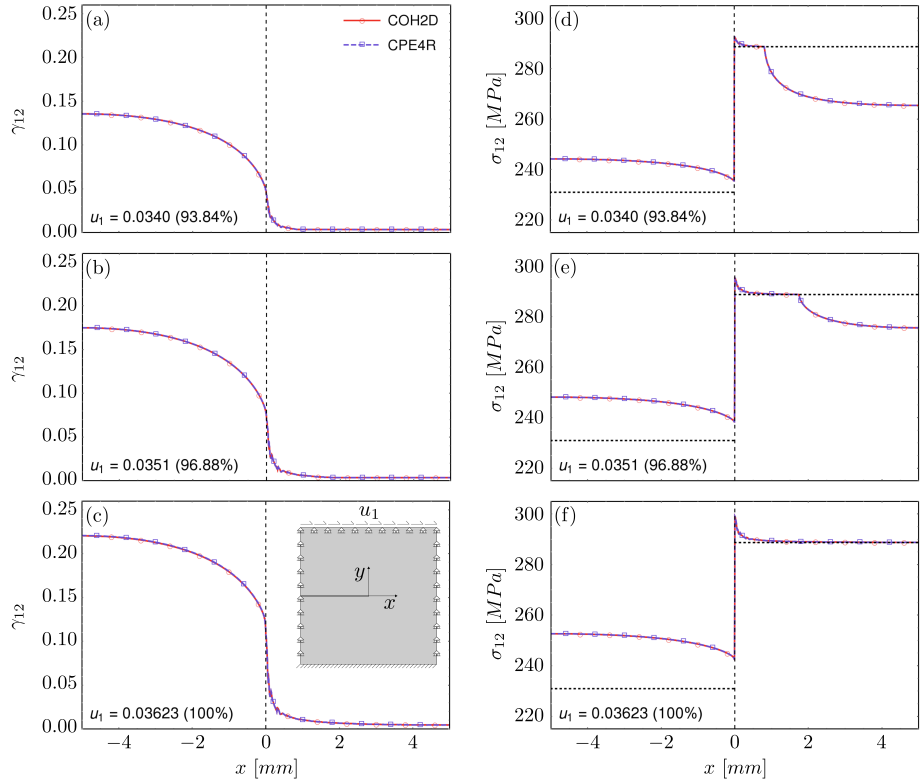

Figure 4.12: Results of simulations performed with different idealizations for the shear band: zero-thickness model (discretized with cohesive elements, COH2D) versus a true layer description (discretized with CPE4R elements). Shear deformation γ_{12} (upper part) and shear stress σ_{12} (lower part) along the horizontal line $y = 0$ containing the pre-existing shear band for the case of a material close to a shear band instability $E_p = 300$ MPa. Three different stages of deformation are shown, corresponding to a prescribed displacement at the upper edge of the square domain $u_1 = 0.0340$ mm (left), $u_1 = 0.0351$ mm (center), $u_1 = 0.03623$ mm (right).

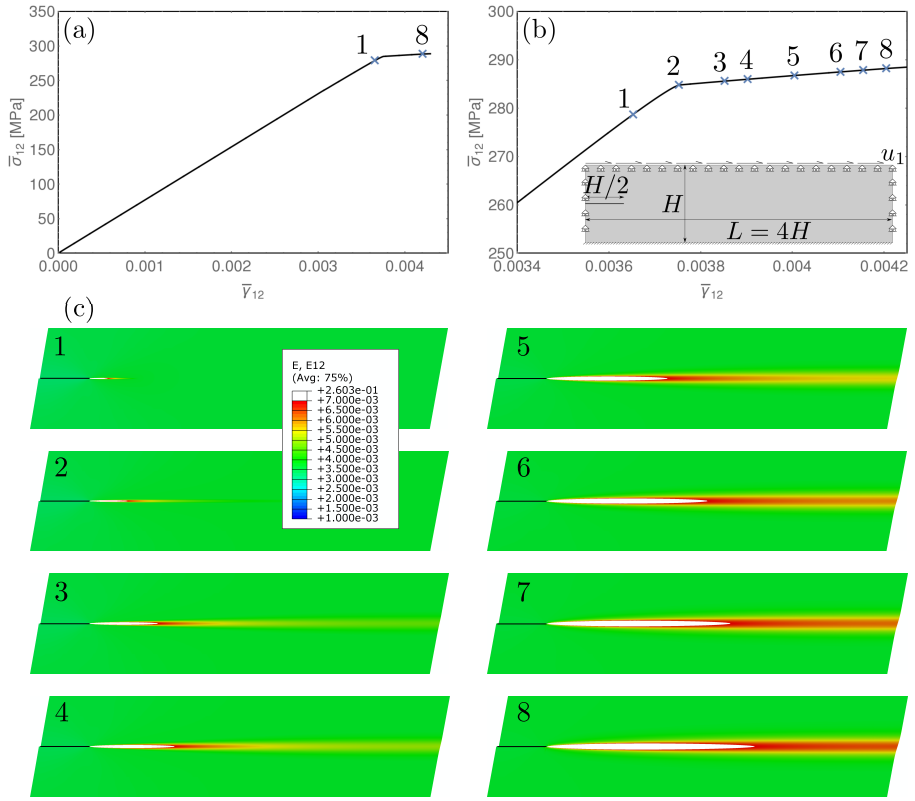

Figure 4.13: Results for a rectangular domain ($L = 40$ mm, $H = 10$ mm) of material close to shear band instability ($E_p = 300$ MPa) and containing a preexisting shear band (of length $H/2 = 5$ mm and constitutive thickness $2h = 0.01$ mm). (a) Overall response curve of the block in terms of average shear stress $\bar{\sigma}_{12} = T/L$, where T is the total shear reaction force at the upper edge of the block, and average shear strain $\bar{\gamma}_{12} = u_1/H$. (b) Magnification of the overall response curve $\bar{\sigma}_{12} - \bar{\gamma}_{12}$ around the stress level corresponding to the yielding of the shear band. (c) Contour plots of the shear deformation γ_{12} at different stages of deformation, corresponding to the points along the overall response curve shown in part (b) of the figure. The deformation is highly focused along a rectilinear path emanating from the shear band tip. The displacements in the figures are amplified by a deformation scale factor of 50.

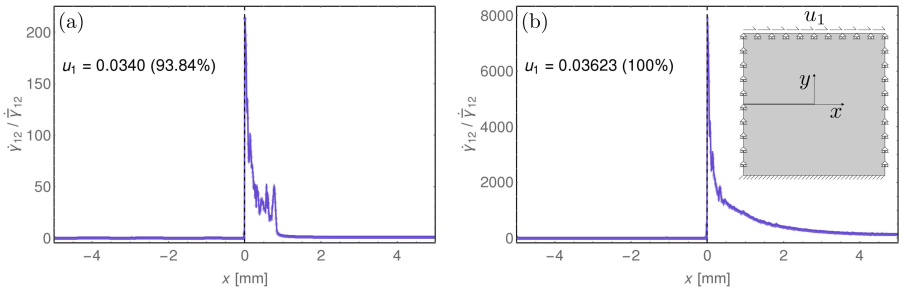

Figure 4.14: The incremental shear strain $\dot{\gamma}_{12}$ (divided by the mean incremental shear strain $\dot{\bar{\gamma}}_{12}$) along the x-axis at the two stages of deformation reported in in Fig. 4.10 and labeled there as (a) and (c). It is clear that a strong strain concentration develops at the tip of the shear band, which becomes similar to the square-root singularity that is found with the perturbative approach (Section 4.4 and Fig. 4.16.

4.4 The perturbative vs the imperfection approach

With the perturbative approach, a perturbing agent acts at a certain stage of uniform strain of an infinite body, while the material is subject to a uniform prestress. Here the perturbing agent is a pre-existing shear band, modelled as a planar slip surface, emerging at a certain stage of a deformation path (Bigoni and Dal Corso, 2008), in contrast with the imperfection approach in which the imperfection is present from the beginning of the loading.

With reference to a x_1–x_2 coordinate system (inclined at 45° with respect to the principal prestress axes x_I–x_{II}), where the incremental stress $\dot{t}_{ij}$ and incremental strain $\dot{\varepsilon}_{ij}$ are defined (i, j =1,2), the incremental orthotropic response under plane strain conditions ($\dot{\varepsilon}_{i3} = 0$) for incompressible materials ($\dot{\varepsilon}_{11} + \dot{\varepsilon}_{22} = 0$) can be expressed through the following constitutive equations (Bigoni, 2012)[8]

$$\dot{t}_{11} = 2\mu\dot{\varepsilon}_{11} + \dot{p}, \quad \dot{t}_{22} = -2\mu\dot{\varepsilon}_{11} + \dot{p}, \quad \dot{t}_{12} = \mu_*\dot{\gamma}_{12}, \tag{4.11}$$

where $\dot{p}$ is the incremental in-plane mean stress, while μ and μ_* describe the incremental shear stiffness, respectively, parallel and inclined at 45° with respect to prestress axes.

The assumption of a specific constitutive model leads to the definition of the incremental stiffness moduli μ and μ_*. With reference to the J_2–deformation theory of plasticity (Bigoni and Dal Corso, 2008), particularly suited to model the plastic branch of the constitutive response of ductile metals, the in-plane deviatoric stress can be written as

$$t_I - t_{II} = k\varepsilon_I|\varepsilon_I|^{(N-1)}. \tag{4.12}$$

In equation (4.12) k represents a stiffness coefficient and $N \in (0, 1]$ is the strain hardening exponent, describing perfect plasticity (null hardening) in the limit $N \to 0$ and linear elasticity in the limit $N \to 1$. For the J_2–deformation theory, the relation between the two incremental shear stiffness moduli can be obtained as

$$\mu_* = N\mu, \tag{4.13}$$

[8]Note that the notation used here differs from that adopted in (Bigoni and Dal Corso, 2008), where the principal axes are denoted by x_1 and x_2 and the system inclined at 45° is denoted by $\hat{x}_1$ and $\hat{x}_2$.

so that a very compliant response under shear ($\mu_* \ll \mu$) is described in the limit of perfect plasticity $N \to 0$.

The perturbative approach (Bigoni and Dal Corso, 2008) can now be exploited to investigate the growth of a shear band within a solid. To this purpose, an incremental boundary value problem is formulated for an infinite solid, containing a zero-thickness pre-existing shear band of finite length $2l$ parallel to the x_1 axis (see Fig. 4.15) and loaded at infinity through a uniform shear deformation $\dot{\gamma}_{12}^{\infty}$.

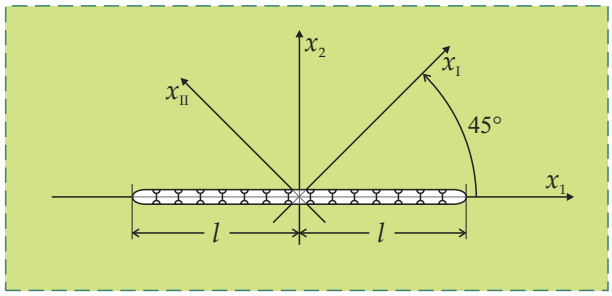

Figure 4.15: A perturbative approach to shear band growth: a pre-existing shear band, modelled as a planar slip surface, acts at a certain stage of uniform deformation of an infinite body obeying the J_2–deformation theory of plasticity

The incremental boundary conditions introduced by the presence of a pre-existing shear band can be described by the following equations:

$$\dot{t}_{21}(x_1, 0^{\pm}) = 0, \quad [\![\dot{t}_{22}(x_1, 0)]\!] = 0, \quad [\![\dot{u}_2(x_1, 0)]\!] = 0, \quad \forall |x_1| < l. \quad (4.14)$$

A stream function $\psi(x_1, x_2)$ is now introduced, automatically satisfying the incompressibility condition and defining the incremental displacements $\dot{u}_j$ as $\dot{u}_1 = \psi_{,2}$, and $\dot{u}_2 = -\psi_{,1}$. The incremental boundary value problem is therefore solved as the sum of $\psi^{\circ}(x_1, x_2)$, solution of the incremental homogeneous problem, and $\psi^{p}(x_1, x_2)$, solution of the incremental perturbed problem.

The incremental solution is reported in Fig. 4.16 for a low hardening exponent, $N = 0.01$, as a contour plot (left) and as a graph (along the x_1-axis, right) of the incremental shear deformation $\dot{\gamma}_{12}$ (divided by the applied remote shear $\dot{\gamma}_{12}^{\infty}$). Note that, similarly to the crack tip fields in fracture mechanics, the incremental stress and deformation display square root singularities at the tips of the pre-existing shear band. Evaluation of

the solution obtained from the perturbative approach analytically confirms the conclusions drawn from the imperfection approach (see the numerical simulations reported in Fig. 4.9 and 4.13), in particular:

- It can be noted from Fig. 4.16 (left) that the incremental deformation is highly focussed along the x_1 direction, confirming that the shear band grows rectilinearly;
- The blow-up of the incremental deformation observed in the numerical simulations near the shear band tip (Fig. 4.14) is substantiated by the theoretical square-root singularity found in the incremental solution (Fig. 4.16, right).

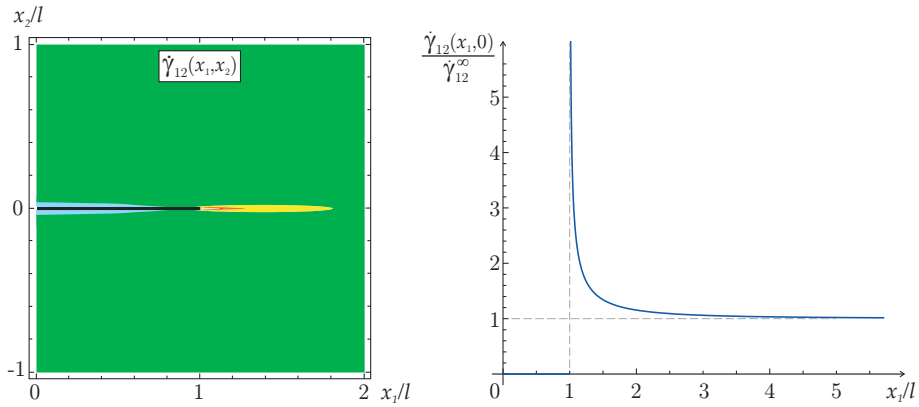

Figure 4.16: Incremental shear strain near a shear band obtained through the perturbative approach: level sets (left) and behaviour along the x_1-axis (right).

We finally remark that, although the tendency towards rectilinear propagation of a shear band has been substantiated through the use of a von Mises plastic material, substantial changes are not expected when a different yield criterion (for instance pressure-sensitive as Drucker-Prager) is employed.

Chapter 5

Sliding interface

Abstract Lubricated sliding contact between soft solids is an interesting topic in biomechanics and for the design of small-scale engineering devices. As a model of this mechanical set-up, two elastic nonlinear solids are considered jointed through a frictionless and bilateral surface, so that continuity of the normal component of the Cauchy traction holds across the surface, but the tangential component is null. Moreover, the displacement can develop only in a way that the bodies in contact do neither detach, nor overlap. Surprisingly, this finite strain problem has not been correctly formulated until now, so this formulation is the objective of the present paper. The incremental equations are shown to be non-trivial and different from previously (and erroneously) employed conditions. In particular, an exclusion condition for bifurcation is derived to show that previous formulations based on frictionless contact or 'spring-type' interfacial conditions are not able to predict bifurcations in tension, while experiments—one of which, ad hoc designed, is reported—show that these bifurcations are a reality and become possible when the correct sliding interface model is used. The presented results introduce a methodology for the determination of bifurcations and instabilities occurring during lubricated sliding between soft bodies in contact.

5.1 Introduction

Lubricated sliding along an interface between two deformable bodies is typically characterized by very low friction and arises, for instance,

in several biotribological systems (Dowson, 2012), such as the contact-lens/cornea (Dunn et al., 2013) and the articular cartilage (Ateshian, 2009) complexes, or in various engineering devices, such as windscreen wipers, aquaplaning tires, and elastomeric seals (Stupkiewicz and Marciniszyn, 2009). These soft and slipping contacts are often characterized by large elastic or viscoelastic deformations so that it is not obvious how to formulate the Reynolds equation to adequately model the fluid flow between two contact surfaces that undergo large time-dependent deformations (Temizer and Stupkiewicz, 2016). Moreover, a distinctive feature of lubricated soft contacts is that they are capable of sustaining *tensile contact tractions* during sliding, particularly in transient conditions, a phenomenon clearly visible when a suction cup is moved on a lubricated substrate. Indeed, as long as the pressure does not drop below the cavitation pressure, a soft contact can be loaded in tension, possibly imposing large deformations in a highly compliant solid. As an example of this situation, the sequence of photos shown in Fig. 5.1 refers to an experiment (performed at the Instabilities Lab of the University of Trento) on tensile buckling involving a sliding contact between two soft solids. This system has been designed and realized to obtain a compliant sliding element, and thus to buckle in tension, without using rigid parts such as rollers or sliding sleeves. In particular, a 'T-shaped' silicon rubber element is clamped at the lower end and connected at the upper flat end to a silicon rubber suction cup, which has been applied with a lubricant oil. The system is pulled in tension and displays a tensile bifurcation in which the 'T' bends while the suction cup slides along the upper flat end of the 'T'. This bifurcation resembles that analyzed in (Zaccaria et al. 2011), but involves here soft solids.

A bilateral and frictionless sliding contact condition has been often employed to model the above-mentioned problems (for instance, in geophysics, Leroy and Triantafyllidis, 1996, or for sliding inclusions, Tsuchida et al., 1986, or roll-bonding of metal sheets, Steif, 1990), where two bodies in a current configuration share a common surface along which shear traction and normal separation/interpenetration must both vanish, but free sliding is permitted.

Another model is based on a 'spring-like' interface, in which the incremental nominal traction is related to the jump in the incremental displacement across the interface (see Suo et al. 1992; Bigoni et al. 1997). This model, in the limit of null tangential stiffness and null normal compliance

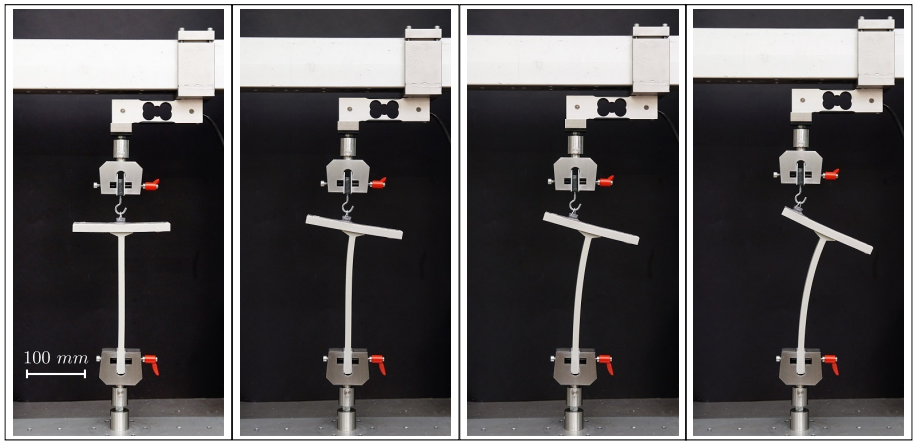

Figure 5.1: A sequence of photos showing a tensile bifurcation involving sliding contact between two soft solids. A silicon rubber suction cup is applied on a lubricant oil film to the upper part of a 'T-shaped' silicon rubber (gray in the photo), clamped at the lower end. The suction cup is pulled vertically, so that the straight configuration of the 'T' is a trivial equilibrium configuration (photo on the left) and a tensile bifurcation occurs when this element starts bending (second photo from the left) and the suction cup slips, as shown in the sequence of photos. Note that in this system rigid mechanical devices such as rollers or sliding sleeves are avoided.

should reduce to the sliding interface model. While these models are elementary within an infinitesimal theory, they become complex when the bodies in contact suffer large displacement/strain (and may evidence bifurcations, as in the case of the soft materials involved in the experimental set-up shown in Fig. 5.1). As a matter of fact, the freely sliding interface model has never been *even formulated* so far and the 'spring-like' model will be shown not to reduce to the freely sliding interface in the above-mentioned limit of vanishing tangential stiffness and normal compliance.

The correct formulation for a sliding interface, together with the derivation of incremental conditions, are the focus of the present article: the former turns out to be non-trivial and the latter corrects previously used conditions, which are shown to lead to incorrect conclusions. Moreover, a generalization of the Hill's exclusion condition for bifurcation (Hill, 1957; see Appendix B) to bodies containing interfaces, shows that the 'spring-like' interface cannot explain bifurcations which can in fact be obtained with the correct formulation of the sliding contact and which exist in reality, as the above-mentioned experiment shows.

The importance of the model derived in this paper is that it allows to obtain analytical solutions for incremental bifurcations of deformed elastic materials in contact with a frictionless planar interface. Several of these solutions, which are important for applications, are obtained, while other problems which do not admit an analytical solution are solved by employing the finite element method and a linear perturbation technique. The obtained solutions show that sliding conditions strongly affect bifurcation loads and promote tensile bifurcations (such as that visible in the experiment reported in Fig. 5.1), which are shown to remain usually undetected by employing previously used, but incorrect, conditions.

5.2 Sliding Interface Conditions

5.2.1 Problem formulation and kinematics of two bodies in frictionless contact

The formulations described in Chapter. (1) are now introduced for the specific mechanical system presented in Fig. 5.2, in which two nonlinear elastic bodies (denoted by '+' and '−') are considered in *plane-strain* conditions, jointed through a bilateral frictionless interface. Points in the reference configurations $\mathcal{B}_0^+$ and $\mathcal{B}_0^-$ are mapped to the current configurations $\mathcal{B}^+$ and $\mathcal{B}^-$ via the deformations $\boldsymbol{g}^\pm : \mathcal{B}_0^\pm \to \mathcal{B}^\pm$, so that

$$\boldsymbol{x}^+ = \boldsymbol{g}^+(\boldsymbol{x}_0^+, t), \qquad \boldsymbol{x}^- = \boldsymbol{g}^-(\boldsymbol{x}_0^-, t), \tag{5.1}$$

where t denotes the time, the subscript '0' is used to highlight the referential description. Therefore, the displacement vector $\boldsymbol{u}$ is related to the deformation through

$$\boldsymbol{u}^\pm = \boldsymbol{g}^\pm(\boldsymbol{x}_0^\pm, t) - \boldsymbol{x}_0^\pm \tag{5.2}$$

where '$\pm$' denotes that the equation holds for both quantities '+' and '−'.

The interface has the form of a regular surface Σ in the current configuration and is the image of another regular surface Σ_0 in the reference configuration, where it admits the arc-length parameterization

$$\boldsymbol{x}_0^+ = \boldsymbol{x}_0(s_0^+), \tag{5.3}$$

so that, since the parameter s_0^- can be expressed as function of s_0^+ and time, the following expression can be derived

$$\boldsymbol{x}_0^- = \boldsymbol{x}_0(s_0^-) = \boldsymbol{x}_0(s_0^-(s_0^+, t)). \tag{5.4}$$

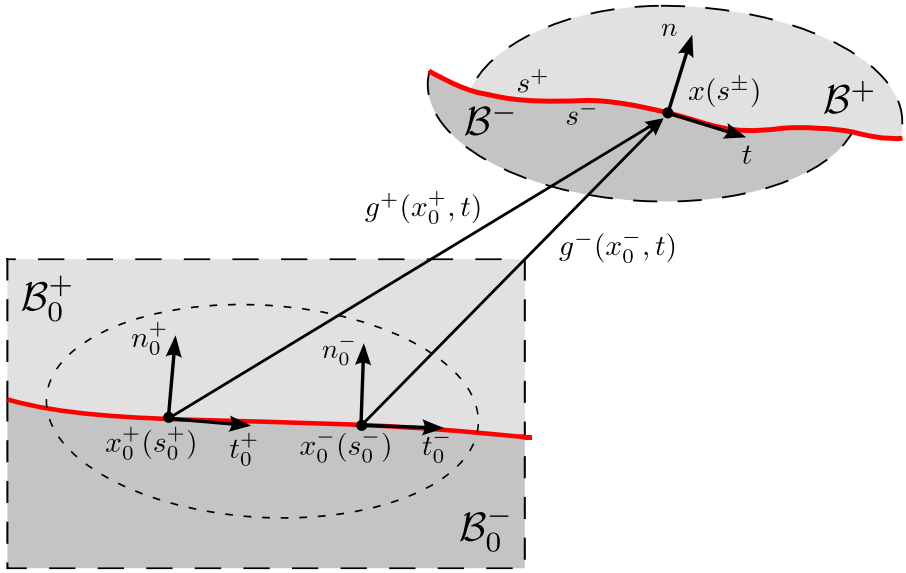

Figure 5.2: Deformation of two nonlinear elastic bodies under plane strain conditions and jointed through a frictionless and bilateral interface. The interface constitutive law enforces a bilateral constraint on the displacement (so that the two bodies can neither detach, nor interpenetrate, during deformation) and continuity of the Cauchy traction, but with the tangential component of the latter being null. A finite and unprescribed sliding of the two bodies can occur across the interface.

The unit tangent vectors to the surface in the reference configuration, Σ_0, can be expressed as

$$\boldsymbol{t}_0^+ = \frac{\partial \boldsymbol{x}_0^+}{\partial s_0^+} \frac{1}{|\frac{\partial \boldsymbol{x}_0^+}{\partial s_0^+}|}, \qquad \boldsymbol{t}_0^- = \frac{\partial \boldsymbol{x}_0^-}{\partial s_0^-} \frac{1}{|\frac{\partial \boldsymbol{x}_0^-}{\partial s_0^-}|}. \tag{5.5}$$

Note that a point $\boldsymbol{x}$ on the interface Σ in the current configuration is the image of two different points $\boldsymbol{x}_0^+$ and $\boldsymbol{x}_0^-$ on Σ_0. This condition, *representing the fact that the two bodies in contact can neither detach nor interpenetrate*, can be expressed as $\boldsymbol{x} = \boldsymbol{x}^+ = \boldsymbol{x}^-$ so that

$$\boldsymbol{g}^+(\boldsymbol{x}_0^+(s_0^+),t) = \boldsymbol{g}^-(\boldsymbol{x}_0^-(s_0^-(s_0^+,t)),t). \tag{5.6}$$

The above condition defines the implicit dependence of s_0^- on s_0^+ (and

time) that has already been exploited in Eq. (5.4). Introducing the deformation gradient

$$\boldsymbol{F}^{\pm} = \frac{\partial \boldsymbol{g}^{\pm}}{\partial \boldsymbol{x}_0^{\pm}}, \tag{5.7}$$

taking the derivative of Eq. (5.6) with respect to s_0^+ and applying the chain rule of differentiation yields

$$\boldsymbol{F}^{+}\frac{\partial \boldsymbol{x}_0^{+}}{\partial s_0^{+}} = \boldsymbol{F}^{-}\frac{\partial \boldsymbol{x}_0^{-}}{\partial s_0^{-}}\frac{\partial s_0^{-}}{\partial s_0^{+}}, \tag{5.8}$$

finally leading to the definition of the tangent vector $\boldsymbol{t}$ in the spatial configuration on Σ at $\boldsymbol{x}$

$$\boldsymbol{t} = \frac{\boldsymbol{F}^{+}\boldsymbol{t}_0^{+}}{|\boldsymbol{F}^{+}\boldsymbol{t}_0^{+}|} = \frac{\boldsymbol{F}^{-}\boldsymbol{t}_0^{-}}{|\boldsymbol{F}^{-}\boldsymbol{t}_0^{-}|}. \tag{5.9}$$

The unit normal at $\boldsymbol{x}$ on Σ can be obtained through the Nanson's rule of area transformation

$$A^{\pm}\boldsymbol{n}^{\pm} = A_0^{\pm} J((\boldsymbol{F}^{\pm})^{-T}\boldsymbol{n}_0^{\pm}), \tag{5.10}$$

$$\boldsymbol{n}^{\pm} = \frac{A_0^{\pm}}{A^{\pm}} J((\boldsymbol{F}^{\pm})^{-T}\boldsymbol{n}_0^{\pm}), \tag{5.11}$$

$$\boldsymbol{n}^{\pm} = \frac{\frac{A_0^{\pm}}{A^{\pm}} J((\boldsymbol{F}^{\pm})^{-T}\boldsymbol{n}_0^{\pm})}{\frac{A_0^{\pm}}{A^{\pm}} J|(\boldsymbol{F}^{\pm})^{-T}\boldsymbol{n}_0^{\pm}|}, \tag{5.12}$$

so that

$$\boldsymbol{n} = \frac{(\boldsymbol{F}^{+})^{-T}\boldsymbol{n}_0^{+}}{|(\boldsymbol{F}^{+})^{-T}\boldsymbol{n}_0^{+}|} = \frac{(\boldsymbol{F}^{-})^{-T}\boldsymbol{n}_0^{-}}{|(\boldsymbol{F}^{-})^{-T}\boldsymbol{n}_0^{-}|}. \tag{5.13}$$

A simple illustration of a kinematics involving sliding between two strained bodies is provided in Appendix 5.A. This can be useful to visualize the constraints imposed by the previously derived equations.

5.2.2 Tractions along the sliding interface

The interface is assumed to maintain a frictionless sliding contact, so that the normal component of the Cauchy traction has to be continuous and the tangential component null. These conditions can be written as follows

$$\boldsymbol{n} \cdot [\![\boldsymbol{T}]\!]\boldsymbol{n} = 0, \qquad \boldsymbol{t} \cdot \boldsymbol{T}^{+}\boldsymbol{n} = \boldsymbol{t} \cdot \boldsymbol{T}^{-}\boldsymbol{n} = 0, \tag{5.14}$$

where $\boldsymbol{T}$ is the Cauchy stress and $[\![\aleph]\!] = \aleph^+ - \aleph^-$ is the jump operator of the quantity $\aleph$ across Σ. On introduction of the first Piola–Kirchhoff stress $\boldsymbol{S} = J\boldsymbol{T}\boldsymbol{F}^{-T}$ (where $J = \det \boldsymbol{F}$) and using the Nanson's rule (5.11) yields

$$\boldsymbol{T}^{\pm}\boldsymbol{n}^{\pm} = \frac{\boldsymbol{S}^{\pm}\boldsymbol{n}_0^{\pm}}{\iota^{\pm}}, \tag{5.15}$$

where $\iota^{\pm} = A^{\pm}/A_0^{\pm}$ is the ratio between the spatial and referential area elements, so that Eqs. (5.14) can be transformed to

$$\boldsymbol{n} \cdot \left(\frac{\boldsymbol{S}^{+}\boldsymbol{n}_0^{+}}{\iota^{+}} - \frac{\boldsymbol{S}^{-}\boldsymbol{n}_0^{-}}{\iota^{-}} \right) = 0, \qquad \boldsymbol{t} \cdot \frac{\boldsymbol{S}^{+}\boldsymbol{n}_0^{+}}{\iota^{+}} = \boldsymbol{t} \cdot \frac{\boldsymbol{S}^{-}\boldsymbol{n}_0^{-}}{\iota^{-}} = 0. \tag{5.16}$$

5.2.3 Motion of two solids in frictionless contact

Before deriving the relations pertaining to the interface, the relations Eqs. (1.45) and (1.46) are now rewritten for the specific mechanical system presented in Fig. 4.3, which are standard for continua and still hold for points at the left and right limit of Σ:

- The material time derivative, denoted by a superimposed dot, of the tangent and normal unit vectors to the surfaces Σ at $\boldsymbol{x}$ are

$$\dot{\boldsymbol{n}}^{\pm} = -(\boldsymbol{I} - \boldsymbol{n}^{\pm} \otimes \boldsymbol{n}^{\pm})(\boldsymbol{L}^{\pm})^{T}\boldsymbol{n}^{\pm} \tag{5.17}$$

  and

$$\dot{\boldsymbol{t}}^{\pm} = (\boldsymbol{I} - \boldsymbol{t}^{\pm} \otimes \boldsymbol{t}^{\pm})\boldsymbol{L}^{\pm}\boldsymbol{t}^{\pm}, \tag{5.18}$$

  where $\boldsymbol{I}$ is the identity tensor, $\boldsymbol{L}^{\pm}$ is the gradient of the spatial description of velocity as reported in Chapter. (1) but now specific for the '+' and '−' parts of the body

$$\boldsymbol{L}^{\pm}(\boldsymbol{x}^{\pm}, t) = \operatorname{grad} \boldsymbol{v}^{\pm}, \tag{5.19}$$

  and $\boldsymbol{v}$ is the spatial description of the velocity of the two bodies

$$\boldsymbol{v}^{\pm}(\boldsymbol{x}^{\pm}, t) = \dot{\boldsymbol{x}}^{\pm}(\boldsymbol{x}_0^{\pm}(\boldsymbol{x}^{\pm}, t), t), \tag{5.20}$$

  where $\boldsymbol{x}_0^{\pm} = \boldsymbol{x}_0^{\pm}(\boldsymbol{x}^{\pm}, t)$ denotes the inverse of $\boldsymbol{x}^{\pm} = \boldsymbol{g}^{\pm}(\boldsymbol{x}_0^{\pm}, t)$.

- The ratio between the deformed and the undeformed area elements can be obtained from the Nanson's rule, Eq. (5.11), as

$$\iota^{\pm} = J^{\pm}|(\boldsymbol{F}^{\pm})^{-T}\boldsymbol{n}_0^{\pm}|, \tag{5.21}$$

from which its material time derivative can be obtained in the form

$$\dot{\iota^{\pm}} = J^{\pm}|(\dot{\boldsymbol{F}^{\pm}})^{-T}\boldsymbol{n}_0^{\pm}|, \tag{5.22}$$

$$\dot{\iota^{\pm}} = \dot{J^{\pm}}|(\boldsymbol{F}^{\pm})^{-T}\boldsymbol{n}_0^{\pm}| + J^{\pm}|\dot{(\boldsymbol{F}^{\pm})^{-T}}\boldsymbol{n}_0^{\pm}|, \tag{5.23}$$

and recalling that

$$\dot{\iota^{\pm}} = Jtr(\boldsymbol{L}), \tag{5.24}$$

and also

$$|\dot{(\boldsymbol{F}^{\pm})^{-T}}\boldsymbol{n}_0^{\pm}| = -(\boldsymbol{n}^{\pm}\cdot(\boldsymbol{L}^{\pm})^T\boldsymbol{n}^{\pm})|(\boldsymbol{F}^{\pm})^{-T}\boldsymbol{n}_0|, \tag{5.25}$$

$$\dot{\iota}^{\pm} = J^{\pm}(\operatorname{tr}\boldsymbol{L}^{\pm} - \boldsymbol{n}^{\pm}\cdot\boldsymbol{L}^{\pm}\boldsymbol{n}^{\pm})\,|(\boldsymbol{F}^{\pm})^{-T}\boldsymbol{n}_0^{\pm}|, \tag{5.26}$$

finally

$$\dot{\iota}^{\pm} = \iota^{\pm}(\boldsymbol{I} - \boldsymbol{n}^{\pm}\otimes\boldsymbol{n}^{\pm})\cdot\boldsymbol{L}^{\pm}, \tag{5.27}$$

as well as the following material time derivative

$$\left(\frac{1}{\iota^{\pm}}\right)^{\cdot} = \frac{-\operatorname{tr}\boldsymbol{L}^{\pm} + \boldsymbol{n}\cdot\boldsymbol{L}^{\pm}\boldsymbol{n}}{J^{\pm}|(\boldsymbol{F}^{\pm})^{-T}\boldsymbol{n}_0^{\pm}|} = -\frac{1}{\iota^{\pm}}(\boldsymbol{I} - \boldsymbol{n}^{\pm}\otimes\boldsymbol{n}^{\pm})\cdot\boldsymbol{L}^{\pm}. \tag{5.28}$$

A point on the sliding interface Σ has to be understood as the 'superposition' of the two points, one belonging to the body $\mathcal{B}^+$ and the other to the body $\mathcal{B}^-$, so that $\boldsymbol{x}^+ = \boldsymbol{x}^-$ along Σ. Taking the time derivative of the equation $\boldsymbol{x}^+ = \boldsymbol{x}^-$ at fixed s_0^+, the velocities of the two points $\boldsymbol{x}^+$ and $\boldsymbol{x}^-$ can be related to each other through

$$\dot{\boldsymbol{x}}^+ = \dot{\boldsymbol{x}}^- + \boldsymbol{F}^-\frac{\partial\boldsymbol{x}_0^-}{\partial s_0^-}\dot{s}_0^-. \tag{5.29}$$

The time derivative at fixed s_0^+ is in fact the material time derivative for the '+' part of the body, while it involves an additional term related to the variation of s_0^- for the '−' part of the body.

Equations (5.5) and (5.9) show that $\boldsymbol{F}^-\partial\boldsymbol{x}_0^-/\partial s_0^-$ is parallel to the tangent unit vector $\boldsymbol{t}$, so that the scalar product of the unit normal $\boldsymbol{n}$

with both sides of Eq. (5.29) yields the continuity condition across the interface Σ for the normal component of the velocity

$$[\![\dot{\boldsymbol{x}}]\!] \cdot \boldsymbol{n} = 0, \tag{5.30}$$

while the scalar product with the unit tangent $\boldsymbol{t}$ yields $\dot{s}_0^-$, thus

$$\dot{s}_0^- = \frac{(\dot{\boldsymbol{x}}^+ - \dot{\boldsymbol{x}}^-) \cdot \boldsymbol{t}}{|\boldsymbol{F}^- \frac{\partial \boldsymbol{x}_0^-}{\partial s_0^-}|}. \tag{5.31}$$

The time derivative of Eqs. (5.9) and (5.13) at fixed s_0^+ provides

$$\dot{\boldsymbol{t}}^+ = \dot{\boldsymbol{t}}^- + \frac{\partial \boldsymbol{t}^-}{\partial s_0^-}\dot{s}_0^-, \qquad \dot{\boldsymbol{n}}^+ = \dot{\boldsymbol{n}}^- + \frac{\partial \boldsymbol{n}^-}{\partial s_0^-}\dot{s}_0^-, \tag{5.32}$$

which using Eqs. (5.18) and (5.17) lead to

$$\frac{\partial \boldsymbol{t}^-}{\partial s_0^-}\dot{s}_0^- = (\boldsymbol{I} - \boldsymbol{t} \otimes \boldsymbol{t})[\![\boldsymbol{L}]\!]\boldsymbol{t}, \qquad \frac{\partial \boldsymbol{n}^-}{\partial s_0^-}\dot{s}_0^- = -(\boldsymbol{I} - \boldsymbol{n} \otimes \boldsymbol{n})[\![\boldsymbol{L}^T]\!]\boldsymbol{n}. \tag{5.33}$$

The scalar product of Eqs. (5.33) with $\boldsymbol{t}$ and $\boldsymbol{n}$ yields

$$\boldsymbol{t} \cdot \frac{\partial \boldsymbol{t}^-}{\partial s_0^-}\dot{s}_0^- = 0, \qquad \boldsymbol{n} \cdot \frac{\partial \boldsymbol{t}^-}{\partial s_0^-}\dot{s}_0^- = [\![L_{nt}]\!], \tag{5.34}$$

and

$$\boldsymbol{n} \cdot \frac{\partial \boldsymbol{n}^-}{\partial s_0^-}\dot{s}_0^- = 0, \qquad \boldsymbol{t} \cdot \frac{\partial \boldsymbol{n}^-}{\partial s_0^-}\dot{s}_0^- = -[\![L_{nt}]\!]. \tag{5.35}$$

The time derivative of Eq. $(5.16)_1$ at fixed s_0^+ allows to obtain

$$\begin{aligned} \boldsymbol{n} \cdot \frac{\dot{\boldsymbol{S}}^+ \boldsymbol{n}_0^+}{\iota^+} - \boldsymbol{n} \cdot \frac{\dot{\boldsymbol{S}}^- \boldsymbol{n}_0^-}{\iota^-} - \dot{s}_0^- \Bigg(& \boldsymbol{n} \cdot \frac{\partial \boldsymbol{S}^-}{\partial s_0^-}\frac{\boldsymbol{n}_0^-}{\iota^-} + \boldsymbol{n} \cdot \boldsymbol{S}^- \boldsymbol{n}_0^- \frac{\partial \left(\frac{1}{\iota^-}\right)}{\partial s_0^-} \\ & + \boldsymbol{n} \cdot \frac{\boldsymbol{S}^-}{\iota^-}\frac{\partial \boldsymbol{n}_0^-}{\partial s_0^-}\Bigg) = \boldsymbol{n} \cdot \boldsymbol{T}\boldsymbol{n}\, [\![L_{tt}]\!], \end{aligned} \tag{5.36}$$

while the time derivative of Eq. $(5.16)_2$ at fixed s_0^+ leads to

$$\boldsymbol{t} \cdot \dot{\boldsymbol{S}}^+ \boldsymbol{n}_0^+ = -\dot{\boldsymbol{t}} \cdot \boldsymbol{S}^+ \boldsymbol{n}_0^+ \tag{5.37}$$

and

$$\boldsymbol{t}\cdot\dot{\boldsymbol{S}}^{-}\boldsymbol{n}_0^{-}=-\dot{\boldsymbol{t}}^{-}\cdot\boldsymbol{S}^{-}\boldsymbol{n}_0^{-}-\dot{s}_0^{-}\frac{\partial\boldsymbol{t}^{-}}{\partial s_0^{-}}\cdot\boldsymbol{S}^{-}\boldsymbol{n}_0^{-}-\dot{s}_0^{-}\boldsymbol{t}^{-}\cdot\frac{\partial\boldsymbol{S}^{-}}{\partial s_0^{-}}\boldsymbol{n}_0^{-}-\dot{s}_0^{-}\boldsymbol{t}^{-}\cdot\boldsymbol{S}^{-}\frac{\partial\boldsymbol{n}_0^{-}}{\partial s_0^{-}},\tag{5.38}$$

so that, using Eqs. (5.34), (5.35), and (5.18), the following expressions are derived

$$\boldsymbol{t}\cdot\dot{\boldsymbol{S}}^{+}\boldsymbol{n}_0^{+}=-L_{nt}^{+}\boldsymbol{n}\cdot\boldsymbol{S}^{+}\boldsymbol{n}_0^{+},\tag{5.39}$$

and

$$\boldsymbol{t}\cdot\dot{\boldsymbol{S}}^{-}\boldsymbol{n}_0^{-}=-L_{nt}^{+}\boldsymbol{n}\cdot\boldsymbol{S}^{-}\boldsymbol{n}_0^{-}-\dot{s}_0^{-}\boldsymbol{t}^{-}\cdot\frac{\partial\boldsymbol{S}^{-}}{\partial s_0^{-}}\boldsymbol{n}_0^{-}-\dot{s}_0^{-}\boldsymbol{t}^{-}\cdot\boldsymbol{S}^{-}\frac{\partial\boldsymbol{n}_0^{-}}{\partial s_0^{-}}.\tag{5.40}$$

5.3 Planar Sliding Interface Conditions

The general interface conditions derived above are now simplified for the special case of a planar sliding interface that is assumed to satisfy the following conditions:

- the interface is planar both in the reference and in the current configurations (but can *incrementally* assume any curvature), so that:

$$\boldsymbol{n}=\boldsymbol{n}_0^{+}=\boldsymbol{n}_0^{-},\qquad\boldsymbol{t}=\boldsymbol{t}_0^{+}=\boldsymbol{t}_0^{-},\qquad\frac{\partial\boldsymbol{n}_0^{-}}{\partial s_0^{-}}=\boldsymbol{0};\tag{5.41}$$

- the Cauchy traction components are uniform at the interface and satisfy:

$$T_{nn}^{+}=T_{nn}^{-},\qquad T_{nt}^{+}=T_{nt}^{-}=0;\tag{5.42}$$

- a relative Lagrangian description is assumed in which the current configuration is assumed as reference (so that $\boldsymbol{F}^{+}=\boldsymbol{F}^{-}=\boldsymbol{I}$ and $\iota^{+}=\iota^{-}=1$ and $\boldsymbol{S}^{\pm}=\boldsymbol{T}^{\pm}$).

It follows from the above assumptions that

$$\frac{\partial\left(\frac{1}{\iota^{-}}\right)}{\partial s_0^{-}}=0,\qquad\frac{\partial\boldsymbol{S}^{-}}{\partial s_0^{-}}=\boldsymbol{0}.\tag{5.43}$$

Now, introducing a reference system x_1–x_2 aligned parallel respectively to the unit tangent $\boldsymbol{t}$ and normal $\boldsymbol{n}$ to the interface, the equations governing the *rate* problem across the above-introduced planar interface are the following:

- continuity of normal incremental displacements, from Eq. (5.30),

$$\dot{x}_n^+ (x_1, 0) = \dot{x}_n^- (x_1, 0) ; \tag{5.44}$$

- continuity of incremental nominal shearing accross the interface, from Eqs. (5.39) and (5.40),

$$\dot{S}_{tn}^+ (x_1, 0) = \dot{S}_{tn}^- (x_1, 0) ; \tag{5.45}$$

- dependence of the incremental nominal shearing on the Cauchy stress component orthogonal to the interface T_{nn} and incremental displacement gradient mixed component L_{nt}, from Eq. (5.39),

$$\dot{S}_{tn}^+ (x_1, 0) = -\alpha T_{nn} L_{nt} (x_1, 0) , \tag{5.46}$$

  where $\alpha = 1$;

- dependence of the jump in the incremental nominal stress orthogonal to the interface on the Cauchy normal component T_{nn} and the jump in the tangential component of the incremental displacement gradient L_{tt}, from Eq. (5.36),

$$\dot{S}_{nn}^+ (x_1, 0) - \dot{S}_{nn}^- (x_1, 0) = \alpha T_{nn} [\![L_{tt} (x_1, 0)]\!]. \tag{5.47}$$

  where, again, $\alpha = 1$.

The parameter α has been introduced in the above equations to highlight the difference with respect to the incorrect conditions sometimes assumed at the interface (for instance by Steif, 1990)

$$\dot{S}_{tn}^{\pm}(x_1, 0) = 0, \qquad \dot{S}_{nn}^+ = \dot{S}_{nn}^-, \tag{5.48}$$

which correspond to $\alpha = 0$. Note that the only possibility to obtain a coincidence between the correct $\alpha = 1$ and the incorrect $\alpha = 0$ conditions is when the stress normal to the interface vanishes, namely, when $T_{nn} = 0$.

The 'spring-type' interfacial conditions used by Suo et al. (1992), Bigoni et al. (1997) and Bigoni and Gei (2001) do not reduce (except when $T_{nn} = 0$) to the correct frictionless sliding conditions (5.46) and (5.47), in the limit when the stiffness tangential to the interface tends to zero and the normal stiffness to infinity. In this limit case, the 'spring-type'

conditions reduce to the incorrect equations obtained with $\alpha = 0$, so that they cannot properly describe slip without friction, unless when $T_{nn} = 0$. Note that the stress orthogonal to the interface, T_{nn} has been always assumed to be null by Bigoni et al. (1997) and Bigoni and Gei (2001); all bifurcation analyses reported in these papers are therefore different from those considered in the present paper, where the transverse stress is never null.

5.3.1 Plane strain bifurcation problems involving a planar interface

In the following, a series of incremental bifurcation problems are solved, involving two elastic nonlinear solids in contact through a sliding interface aligned parallel to the x_1–axis. This problem set-up is similar to various situations analyzed in the literature (Ottenio et al., 2007; Dowaikh and Ogden, 1991; Bigoni and Gei, 2001), with the variant that now the interfacial condtions are different. It is important to highlight that the two solids in contact may be characterized by different constitutive assumptions and may be subject to a different state of prestress in the x_1–direction. In fact, the possibility that the two bodies may freely slide across the interface allows to relax the usual compatibility restrictions.

The incremental constitutive equations are characterized by the parameters ξ,η and k, as shown in Chapter. (3), so that

$$\dot{S}_{11} = \mu(2\xi - k - \eta)L_{11} + \dot{p}, \qquad \dot{S}_{22} = \mu(2\xi + k - \eta)L_{22} + \dot{p},$$
$$\dot{S}_{21} = \mu[(1+k)L_{21} + (1-\eta)L_{12}], \qquad \dot{S}_{12} = \mu[(1-\eta)L_{21} + (1-k)L_{12}], \tag{5.49}$$

where $\dot{p}$ plays the role of a Lagrangean multiplier, because the body is assumed incompressible, $L_{kk} = 0$. For the sake of simplicity, a neo-Hookean material behaviour is assumed, $\xi = 1$, so that the material always lies in the elliptic imaginary (EI) regime and

$$-1 < k < 1, \qquad \Lambda = \sqrt{4\xi^2 - 4\xi + k^2} = |k|, \tag{5.50}$$

together with additional definitions to be used later,

$$\beta_1 = \sqrt{\frac{1+|k|}{1-|k|}} \quad \beta_2 = \sqrt{\frac{1-|k|}{1-|k|}}, \tag{5.51}$$

and

$$\Omega_1 = i\beta_1, \quad \Omega_2 = i\beta_2, \quad \Omega_3 = -i\beta_1, \quad \Omega_4 = -i\beta_2. \tag{5.52}$$

Two elastic prestressed half-spaces in contact through a planar sliding interface

Two elastic half-spaces are now considered in contact through a sliding interface, planar in the current configuration, which is assumed as reference configuration, see the inset in Fig. 5.3.

The upper (the lower) half-space $x_2 > 0$ ($x_2 < 0$) is denoted with '+' (with '−') and the incremental conditions at the interface are given by Eqs. (5.44)–(5.47), plus the condition of exponential decay of the solution in the limits $x_2 \to \pm\infty$. For simplicity the two half spaces are modelled with the same material and subject to the same prestress, so that bifurcations are possible only due to the presence of the interface.

Employing the representation

$$v_1^{\pm} = \widehat{v}_1^{\pm}(x_2) f(c_1, x_1), \qquad v_2^{\pm} = \widehat{v}_2^{\pm}(x_2) f^{'}(c_1, x_1), \tag{5.53}$$

$$f(c_1, x_1) = \exp(ic_1 x_1), \qquad f^{'}(c_1, x_1) = if(c_1, x_1), \tag{5.54}$$

$$\widehat{v}_1^{\pm}(x_2) = -b_1^{\pm}\Omega_1^{\pm} e^{ic_1\Omega_1^{\pm}x_2} - b_2^{\pm}\Omega_2^{\pm} e^{ic_1\Omega_2^{\pm}x_2} - b_3^{\pm}\Omega_3^{\pm} e^{ic_1\Omega_3^{\pm}x_2} - b_4^{\pm}\Omega_4^{\pm} e^{ic_1\Omega_4^{\pm}x_2}, \tag{5.55}$$

$$\widehat{v}_2^{\pm}(x_2) = -i\left[b_1^{\pm} e^{ic_1\Omega_1^{\pm}x_2} + b_2^{\pm} e^{ic_1 x_2} + b_3^{\pm} e^{ic_1\Omega_3^{\pm}x_2} + b_4^{\pm} e^{ic_1\Omega_4^{\pm}x_2}\right] \tag{5.56}$$

for the incremental displacements (Bigoni, 2012), where c_1 is the wavenumber of the bifurcated mode, the decaying condition implies

$$b_1^- = b_2^- = b_3^+ = b_4^+ = 0, \tag{5.57}$$

so that the eigenvalue problem governing incremental bifurcations can be written as

$$\left[\boldsymbol{M}\right] \begin{bmatrix} b_1^+ \\ b_2^+ \\ b_3^- \\ b_4^- \end{bmatrix} = 0, \tag{5.58}$$

where the matrix $[\boldsymbol{M}]$ is given by

$$\begin{bmatrix} 1 & 1 & -1 & -1 \\ 2-\eta+\Lambda & 2-\eta-\Lambda & -2+\eta-\Lambda & -2+\eta+\Lambda \\ 2-\eta+\Lambda+\frac{T_{nn}}{\mu}\alpha & 2-\eta-\Lambda+\frac{T_{nn}}{\mu}\alpha & 0 & 0 \\ \left(2-\eta-\Lambda+\frac{T_{nn}}{\mu}\alpha\right)\sqrt{\frac{1+\Lambda}{1-k}} & \left(2-\eta+\Lambda+\frac{T_{nn}}{\mu}\alpha\right)\sqrt{\frac{1-\Lambda}{1-k}} & \left(2-\eta-\Lambda+\frac{T_{nn}}{\mu}\alpha\right)\sqrt{\frac{1+\Lambda}{1-k}} & \left(2-\eta+\Lambda+\frac{T_{nn}}{\mu}\alpha\right)\sqrt{\frac{1-\Lambda}{1-k}} \end{bmatrix}. \tag{5.59}$$

Non-trivial solutions of the system (5.58) are obtained when $\det \boldsymbol{M} = 0$, to be solved for the bifurcation stress. Note that matrix $\boldsymbol{M}$ does not contain the wavenumber of the bifurcated mode, so that the critical load for bifurcation is independent of the wavelength of the bifurcation mode (even if the sliding interface is present).

The resulting bifurcation condition for a sliding interface ($\alpha = 1$) can be written as

$$\sqrt{1-\Lambda}\left(\frac{T_{nn}}{\mu}+2-\eta+\Lambda\right)^2-\sqrt{1+\Lambda}\left(\frac{T_{nn}}{\mu}+2-\eta-\Lambda\right)^2=0. \quad (5.60)$$

If, instead of the correct interface conditions, $\alpha = 1$, one assumes the incorrect condition $\alpha = 0$, bifurcation corresponds to

$$\sqrt{1-\Lambda}\,(2-\eta+\Lambda)^2-\sqrt{1+\Lambda}\,(2-\eta-\Lambda)^2=0. \quad (5.61)$$

Using Eqs. (3.30) and for given values of longitudinal T_{tt} and transverse T_{nn} prestresses, Eqs. (5.60) and (5.61) (which hold for a generic incompressible material, subject to generic prestress conditions) can be solved. Results are reported in Fig. 5.3 for a neo-Hookean material, $\xi = 1$, assuming both the correct condition $\alpha = 1$ (on the left) and the incorrect one $\alpha = 0$ (on the right). The red and blue zones identify in the figure the prestress combinations for which $\det \boldsymbol{M}$ assumes positive and negative values, respectively, so that the boundary between these zones (marked with red lines) corresponds to bifurcation. The dashed lines represent failure of ellipticity, so that points situated beyond this line do not represent states attainable through a smooth deformation path (because ellipticity loss corresponds to the emergence of discontinuous solution).

Note that in the case of null prestress normal to the interface, $T_{nn} = 0$, an interfacial bifurcation occurs for $T_{tt}/\mu \approx -1.679$, the same value which gives the surface instability of a half space, which is unaffected by the condition $\alpha = 1$ or $\alpha = 0$. This is the only situation in which the two conditions provide the same bifurcation stress.

An interesting case occurs when only a tensile prestress orthogonal to the interface T_{nn} is applied (and the transverse prestress is null, $T_{tt} = 0$), where a *tensile bifurcation* occurs for $T_{nn}/\mu \approx 1.679$, which is absent when the incorrect condition $\alpha = 0$ is used or also if the modelling would involve a perfectly bonded interface (in which case all bifurcations are excluded within the limits of ellipticity). This simple example reveals the importance of a correct definition of the interfacial conditions.

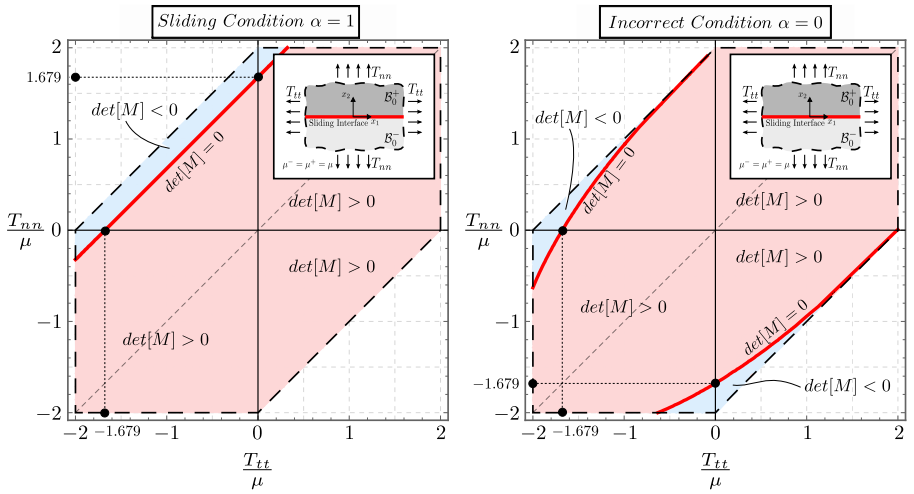

Figure 5.3: Interfacial bifurcation of two elastic incompressible half-spaces (made up of the same neo-Hookean material, subject to the same prestress) in contact through a planar sliding interface in the $T_{nn}-T_{tt}$ plane for a sliding interface $\alpha = 1$ (left). The incorrect condition $\alpha = 0$ is also included for comparison (right). The points corresponding to bifurcation are represented by red lines (at the boundary between the red and blue zones), while the dashed lines correspond to failure of ellipticity. Note that with $\alpha = 1$ bifurcation in pure tension occurs (i.e. with $T_{tt} = 0$), which is excluded for $\alpha = 0$. Therefore, the (correct) sliding interface condition explains tensile bifurcation. Note also that in this case bifurcations for both negative stresses T_{nn} and T_{tt} do not occur (except in the domain of slightly negative T_{nn}).

A comparison between the correct $\alpha = 1$ and incorrect $\alpha = 0$ conditions reveals a completely different bifurcation behaviour. In fact, for positive T_{nn} bifurcation is possible in the correct case for negative, null and slightly positive T_{tt}. These bifurcations do not occur in the incorrect situation. Moreover in the latter situation there is a zone of bifurcation occurring for negative T_{nn} which is excluded in the correct case. As an example, in the special, but interesting, case of uniaxial compression ($T_{nn} < 0$ with $T_{tt} = 0$), there is no bifurcation in the correct case $\alpha = 1$, while bifurcation occurs in the other case.

To better elucidate this situation, an exclusion condition of the Hill (1957) type is derived in Appendix 5.B. For $\alpha = 0$, this condition becomes completely insensible to the presence of the sliding interface (and reduces to the Hill's condition obtained without consideration of any interface),

so that bifurcation is always excluded when both conditions $T_{nn} \geq 0$ and $T_{tt} \geq 0$ hold true. Using the correct parameter $\alpha = 1$, the exclusion condition evidences a term pertaining to the interface, which allows the bifurcation to occur for both positive T_{nn} and T_{tt}.

Elastic layer on an elastic half-space, in contact through a planar sliding interface

An elastic layer (of current thickness H) is considered, connected to an elastic half-space through a planar sliding interface, see the inset in Fig. 5.4. Both the layer and the half-space are assumed to obey the same neo-Hookean material model. The system is subject to a uniform biaxial Cauchy prestress state with principal components T_{tt} and T_{nn}. A reference system x_1–x_2 is introduced aligned parallel respectively to the unit tangent $\boldsymbol{t}$ and normal $\boldsymbol{n}$ to the interface.

In addition to the incremental boundary conditions given by Eqs. (5.44)–(5.47) at the sliding interface ($x_2 = 0$), the decaying condition as $x_2 \to -\infty$, plus the condition holding at the free surface ($x_2 = H$), have to be enforced. The latter condition differs for dead or pressure loading as follows:

- for dead loading,

$$\dot{S}^{+}_{nn}(x_1, H) = \dot{S}^{+}_{tn}(x_1, H) = 0; \tag{5.62}$$

- for pressure loading,

$$\begin{aligned} \dot{S}^{+}_{nn}(x_1, H) &= -T_{nn} L_{nn}(x_1, H), \\ \dot{S}^{+}_{tn}(x_1, H) &= -T_{nn} L_{nt}(x_1, H). \end{aligned} \tag{5.63}$$

Imposing the above conditions, a linear homogeneous system is obtained for the bifurcation stress T_{nn}/μ, when the longitudinal prestress is assumed null ($T_{tt}/\mu = 0$). The bifurcation stress is reported in Fig. 5.4 as a function of the wavenumber of the bifurcated field, for both situations of dead loading and pressure loading and for both correct and incorrect conditions, respectively, $\alpha = 1$ and $\alpha = 0$.

For pressure loading, a tensile bifurcation is observed, which occurs for both the correct ($\alpha = 1$, left in the figure) and incorrect ($\alpha = 0$, right in the figure) conditions at the interface. A tensile bifurcation for dead loading

is possible only when the correct condition $\alpha = 1$ is employed, while in the other case the Hill's type condition (see Appendix 5.B) excludes bifurcations for tensile T_{nn} and null T_{tt}. In any case, results are strongly different for the correct and incorrect models of interface, showing once again the importance of a correct modelling of interfacial conditions.

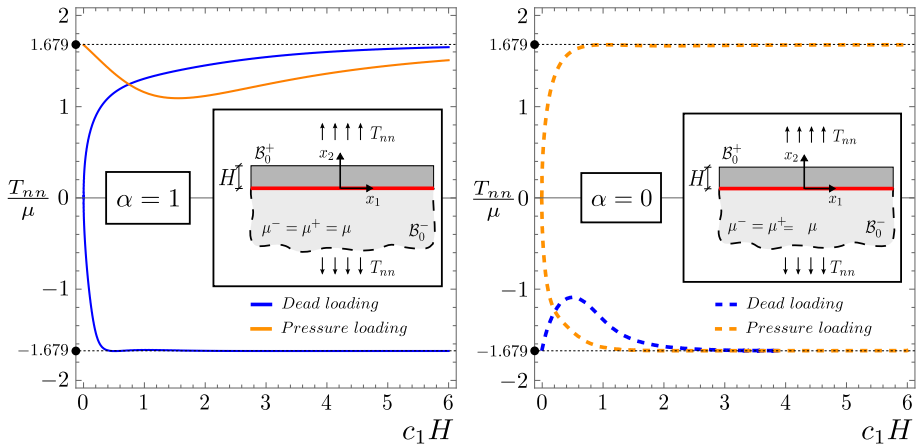

Figure 5.4: Bifurcation of a layer connected to an elastic incompressible half-space through a sliding interface. Both layer and half-space are modelled with the same neo-Hookean material and subject to the same prestress orthogonal to the interface. Both dead and pressure loadings are considered for the two interfacial conditions $\alpha = 1$ and $\alpha = 0$ (the latter condition is incorrect and included only for comparison). The normalized bifurcation stress T_{nn}/μ is reported versus the normalized wavenumber of the bifurcated field $c_1 H$. Note that for dead load bifurcation in tension is possible only when the correct interfacial condition, $\alpha = 1$, is considered.

Two elastic layers

Two layers (one denoted by '+' and the other by '−'), connected through a planar sliding interface are considered, subject to transverse and longitudinal prestresses T_{nn} and T_{tt}. The transverse stress is assumed to be generated by either a dead, Eqs. (5.62), or a pressure, Eqs. (5.63), loading (see the insets in Fig. 5.5). Now only the correct condition $\alpha = 1$ is considered, as for $\alpha = 0$ the Hill's type condition excludes bifurcation for positive dead loading T_{nn} and null transversal loading, see Appendix 5.B.

As in the case of a layer on a half-space ($H^-/H^+ \to \infty$), see Sec-

tion 5.3.1, compressive pressure loading, $T_{nn} < 0$, does not lead to buckling, and tensile dead loading yields a bifurcation. The results for $H^-/H^+ < 1$ are included in Fig. 5.5 for illustration purposes only, as they correspond to the respective results for the reciprocal value of $H^-/H^+ > 1$ upon adequate rescaling of cH^+.

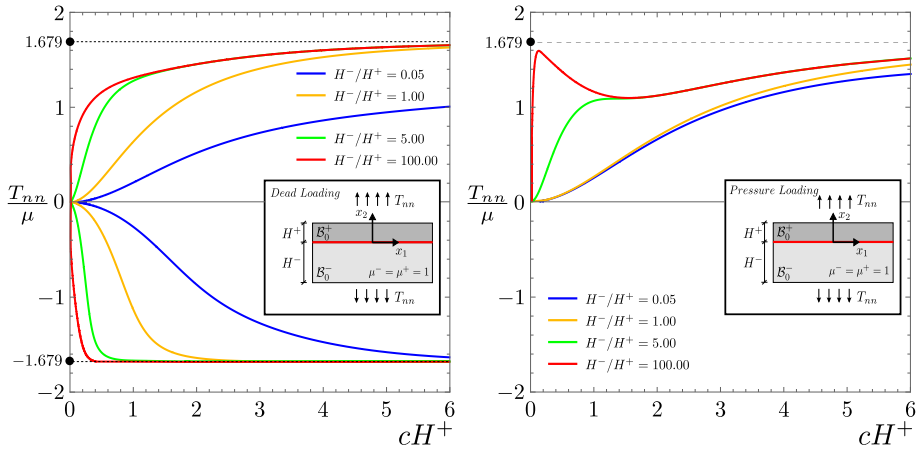

Figure 5.5: Bifurcation of two elastic incompressible layers in contact through a sliding interface. Both layers are modelled with the same neo-Hookean material and subject to the same prestress orthogonal to the interface. The normalized bifurcation stress T_{nn}/μ is reported versus the normalized wavenumber of the bifurcated field $c_1 H^+$, for different values of the thickness ratio H^-/H^+.

5.4 Bifurcations in Complex Problems Involving a Sliding Interface

A special feature characterizing the presence of sliding interfaces is the appearance of tensile bifurcations, often excluded for other models of interfaces (for instance in the perfectly bonded case). These bifurcations are usually hard to be obtained analytically (the simple cases reported in the previous section are of course exceptions), so that the aim of this section is to use a finite-element method combined with a linear perturbation analysis to analyze tensile bifurcations occurring under plane strain conditions in a system of two elastic slender blocks and a hollow cylinder with an internal coating, in both cases jointed through a sliding interface. The

former mechanical system is related to the problem of buckling in tension of two elastic rods (Zaccaria et al., 2011), while the latter is related to a problem of coating detachment.

5.4.1 Finite-element treatment

A mixed formulation is adopted in order to implement incompressible hyperelasticity in plane-strain conditions. Quadrilateral 8-node elements are used with quadratic (serendipity) interpolation of displacements and continuous bilinear interpolation of the pressure field that plays the role of a Lagrange multiplier enforcing the incompressibility constraint using the augmented Lagrangian method. Standard 3×3 Gaussian quadrature is applied. As in the analytical examples studied in the previous section, the constitutive response is modelled using the incompressible neo-Hookean model.

The sliding interface is modeled as a frictionless bilateral interface in the geometrically-exact finite-deformation setting. Quadratic interface elements are used for that purpose with each surface represented by three nodes, so that curved interfaces can be correctly represented. The closest-point projection is used to determine the points that are in contact, and the augmented Lagrangian method is used to enforce the bilateral (equality) constraint. Those aspects follow the standard concepts used in computational contact mechanics (Wriggers, 2006), except that here bilateral rather than unilateral contact is considered. The present implementation employing interface elements is suitable for relatively small, but finite relative sliding. This is sufficient for the purpose of bifurcation analysis that is carried out below.

The bifurcation analysis is performed using a linear perturbation technique. Specifically, a linear perturbation is applied in the deformed (prestressed) base state that corresponds to a gradually increasing load, and the bifurcation point is detected when the perturbation grows to infinity.

Implementation and computations have been performed using the *AceGen/AceFEM* system (Korelc, 2009). As a verification of the computational scheme, the problem of two elastic half-spaces (Section 5.3.1) and the problem of a layer on an elastic half-space (Section 5.3.1) have been analyzed, and a perfect agreement with the corresponding analytical solutions has been obtained.

5.4.2 Tensile bifurcation of two elastic slender blocks connected through a sliding interface

As the first numerical example, bifurcation in tension is studied for the problem of two identical elastic rectangular blocks jointed through a frictionless bilateral-contact interface, see the inset in Fig. 5.6. The axial displacements are constrained at one support and uniform axial displacement is prescribed at the other support. Additionally, in each block, the lateral displacement is constrained at one point in the middle of the support. In the base state, the rods are thus uniformly stretched, while the bifurcation mode in tension involves bending of both blocks accompanied by relative sliding at the interface, as shown in the inset of Fig. 5.6, where the problem scheme, together with the undeformed mesh and the deformed mesh at buckling are reported (the mesh used in the actual computations was finer than that shown in Fig. 5.6 as an illustration).

The present problem is, in fact, a continuum counterpart of the problem, studied by Zaccaria et al. (2011), of tensile bifurcation of two inextensible elastic Euler–Bernoulli beams clamped at one end and jointed through a slider. For that problem, the normalized critical tension force F_{cr} has been found equal to $4F_{cr}L^2/(\pi^2 B) = 0.58$, where L denotes the beam length and B the bending stiffness.

Figure 5.6 shows the normalized critical force as a function of the initial length-to-height ratio, L_0/H_0. For consistency, the force has been normalized using the current length $L = \lambda L_0$ and the bending stiffness $B = \mu H^3/3$ (per unit thickness) has been determined in terms of the current height $H = \lambda^{-1}H_0$ and current incremental shear modulus $\mu = \mu_0(\lambda^2 + \lambda^{-2})/2$, even though the critical stretch λ is close to unity (e.g., $\lambda = 1.006$ for $L_0/H_0 = 4$ and $\lambda = 1.002$ for $L_0/H_0 = 8$). The result in Fig. 5.6 shows that for slender blocks the critical force agrees well with the model of Zaccaria et al. (2011), which critical load is reported with a red straight line. For thick blocks, the two models differ, for instance, by 20% at $L_0/H_0 = 4$.

5.4.3 Hollow cylinder with internal coating

A hollow cylinder is now considered with an internal coating and loaded by a uniform external pressure. The cylinder and the coating interact through a frictionless contact interface. The geometry is specified by the

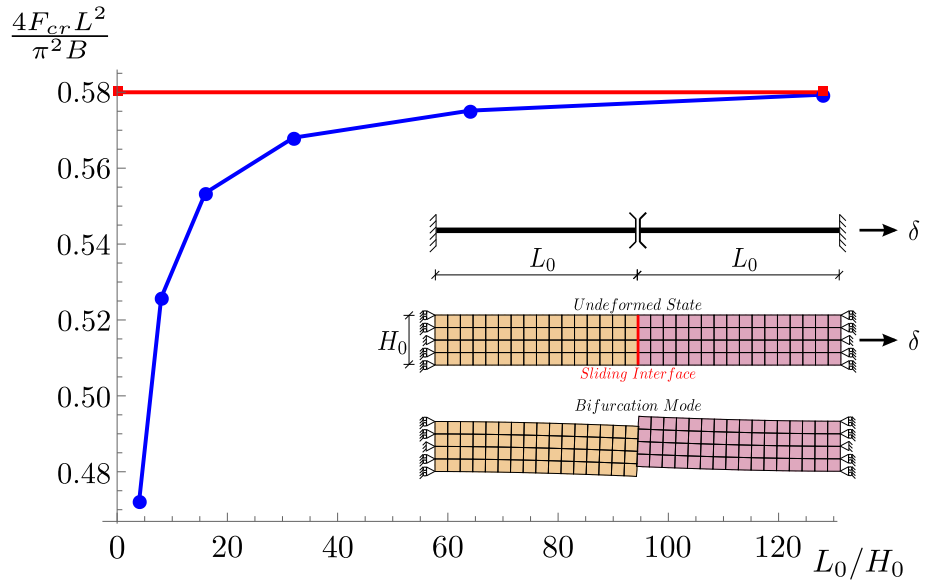

Figure 5.6: Two identical neo-Hookean rectangular blocks uniformly deformed in tension, jointed through a sliding interface. The blocks have initial length L_0, width H_0, and shear modulus $\mu_0 = \mu_0^+ = \mu_0^-$. The bifurcation force F_{cr} is made dimensionless through multiplication by the square of the current length L of the blocks and division by the bending stiffness B (per unit thickness) of the blocks calculated with reference to their current width L. Note that the bifurcation force tends, at increasing length of the block, to the value calculated for two elastic rods in tension of shear stiffness μ_0 (reported with a straight red line).

outer radius R_o, the inner radius R_i, and the coating thickness h that has been assumed equal to $h = 0.01R_o$, see the inset in Fig. 5.7. The shear moduli of the tube and coating are equal. The case where the coating is absent is also investigated for comparison.

Figure 5.7 shows the critical pressure p_{cr} normalized through division by the shear modulus μ_0 as a function of the inner-to-outer radius ratio, R_i/R_o. As a reference, the critical load of a hollow cylinder without coating is also included. The bifurcation modes are reported in Fig. 5.8 for the uncoated and in Fig. 5.9 for the coated case. In the case of coating, two buckling modes are observed depending on the wall thickness. For R_i/R_o greater than approximately 0.38, a global buckling mode occurs, as illustrated in Fig. 5.9. This mode is also characteristic for the uncoated hollow cylinder in the whole range of R_i/R_o. For the same ratio of R_i/R_o

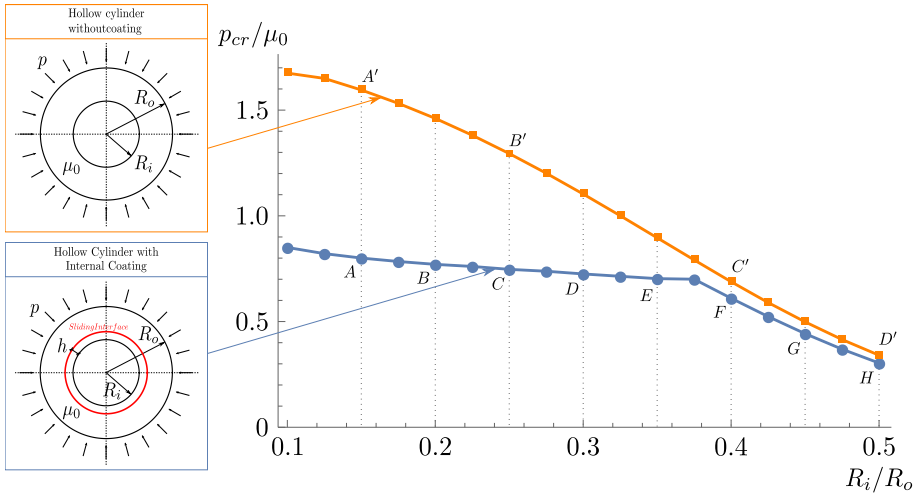

Figure 5.7: Bifurcation pressure p_{cr}, made dimensionless through division by the shear modulus μ_0, for a cylinder with (blue line) and without (orange line) internal coating, as a function of the ratio between the inner and outer radii of the cylinder, R_i/R_o. The coating is connected to the cylinder with a sliding interface. Note the strong decrease of the bifurcation pressure due to the presence of the coating.

and the same load p/μ_0, the base state is identical for the cylinder with coating and for the uncoated one. However, the critical load is different, and, in the global-mode regime, the sliding interface reduces the critical load by approximately 11%.

A local bifurcation mode is observed for the coated hollow cylinder when R_i/R_o is less than approximately 0.38, as illustrated in Fig. 5.9. In this buckling mode, the layer and the inner part of the tube deform in a wave-like fashion, while the outer part of the tube remains intact. This mode is thus similar to the buckling mode characteristic for the layer resting on an elastic half-space, see Section 5.3.1, with the difference that here the substrate is curved. In the local-mode regime, the critical load is significantly reduced with respect to the uncoated cylinder (which buckles in the global mode). For instance, for $R_i/R_o = 0.1$, the critical load is reduced by 50%.

As a conclusion, the presence of a coating connected with a sliding interface is detrimental to the stability of the system, so that the coating tends to slide and the bifurcation load is strongly lower than that calculated in the case when the coating is absent.

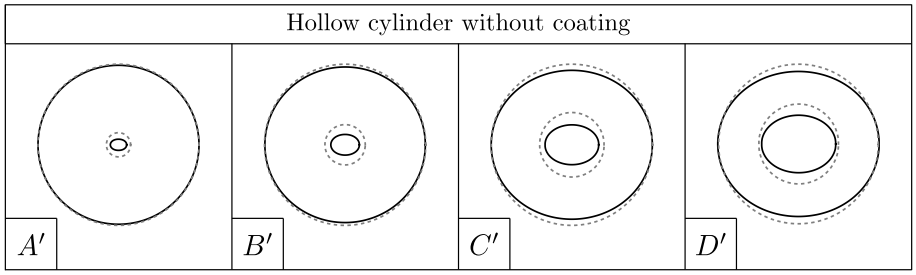

Figure 5.8: Bifurcation modes for a hollow cylinder (without coating) subjected to an external pressure (dashed lines denote the undeformed configuration, solid lines denote the bifurcation mode in the deformed configuration). The bifurcation modes correspond to the loads indicated in Fig. 5.7, to which the letters are referred.

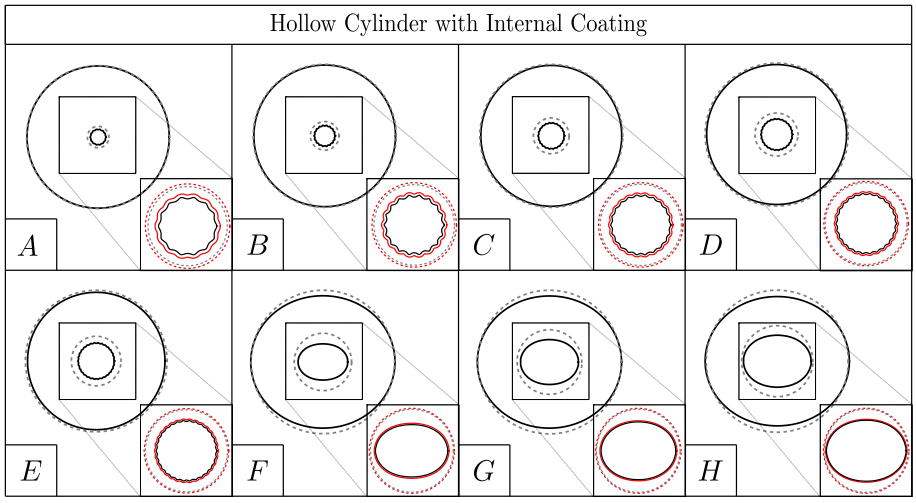

Figure 5.9: Bifurcation modes for a hollow cylinder with an internal coating jointed through a sliding interface. The cylinder is subjected to an external pressure. Bifurcation modes correspond to the loads indicated in Fig. 5.7, to which the letters are referred. Note that an enlarged detail of the inner, coated surface is reported for each geometry (dashed lines denote the undeformed configuration, solid lines denote the bifurcation mode in the deformed configuration, the sliding interface is denoted in red).

5.5 Experimental Evidence of Tensile Bifurcation and Sliding Between Two Soft Solids in Contact Through a Sliding Interface

As mentioned in the introduction, experiments have been designed and realized (in the 'Instabilities Lab' of the University of Trento), showing a tensile bifurcation which involves two soft solids connected through a sliding interface, Fig. 5.10.

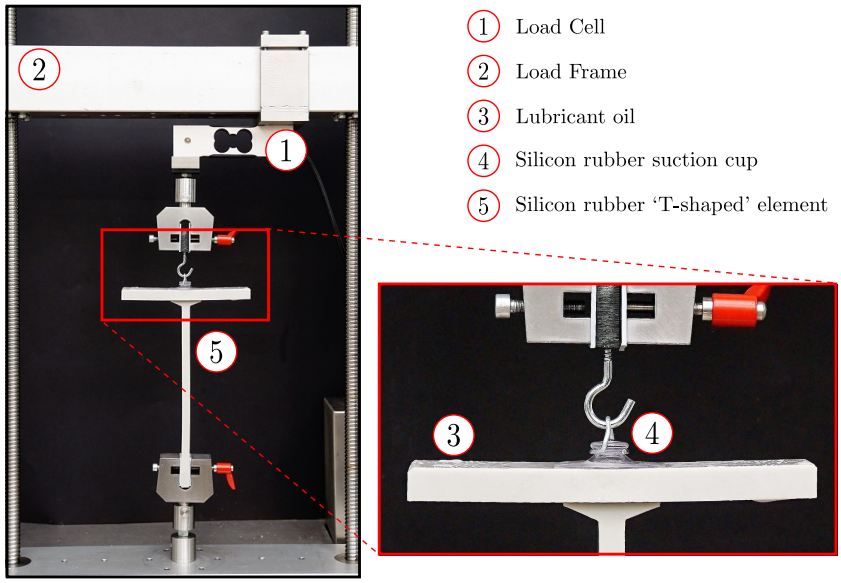

Figure 5.10: The set-up of an experiment showing a tensile bifurcation involving two soft solids connected trough a sliding interface. A vertical displacement (rotations are left free) is imposed to the head of a suction cup connected to a 'T-shaped' silicon rubber element. A lubricant oil is applied, so that the suction cup can slide along the upper edge of the 'T' element.

In particular, a 'T-shaped' silicon rubber element has been manufactured with a 'stem' having rectangular cross section 10 mm × 30 mm (RBSM from Misumi, with 7.4 MPa ultimate tensile strength) and an upper end of dimensions 160 mm × 10 mm × 40 mm. Three different lengths of the stem have been tested, namely, $L_1 = 210$ mm, $L_2 = 180$ mm, and $L_3 = 150$ mm. The upper flat part of the 'T' has been attached (through a lubricant oil, Omala S4WS 460) to a silicon rubber suction

cup. The suction cup has been pulled in tension (by imposing a vertical displacement at a velocity of 0.7 mm/s, with a uniaxial testing machine, Messphysik midi 10). The load and displacement have been measured respectively with a load cell (a MT1041, RC 20kg, from Metler Toledo) and the potentiometric transducer inside the testing machine. Data have been acquired with a system NI CompactDAQ, interfaced with Labview (National Instruments).

The oil used at the suction cup contact allows the suction cup to slide along the upper part of the 'T' element. Therefore, when the suction cup is pulled, the system initially remains straight and the stem deforms axially. However, at a sufficiently high load, a critical condition is reached and the system buckles. Consequently, the stem of the 'T' element bends and the suction cup slides along its upper flat end, see Fig. 5.1.

This is a simple experiment showing a tensile bifurcation of two soft elastic materials (the 'T' element and the suction cup), when they are connected through a sliding interface, a phenomenon which is predicted by the model developed in the present paper, in particular by the use of the correct interface conditions (5.44)–(5.47).

Note, however, that the oil does not allow a completely free sliding of the suction cup, so that an initial relative movement at the suction cup–rubber element interface requires the attainment of an initial force, which suddenly decreases when the relative displacement increases and eventually becomes negligible, thus realizing the sliding interfacial conditions analyzed in the present paper. This is evident in the load-displacement curves, shown in Fig. 5.11, two for each tested length. The curves are marked blue for $L = 210$ mm, green for $L = 180$ mm and red for $L = 150$ mm. The curves show a peak in the force, followed by steep softening and the final attainment of a steady sliding state, where the junction behaves as a sliding interface. The peak forces exhibit a significant scatter which is related to the transition from sticking friction, through mixed lubrication at the onset of sliding, to hydrodynamic lubrication during developed sliding, the latter exhibiting much smaller scatter.

The interest in the developed soft system is that it allows the realization of an element buckling in tension, which is essentially similar to the structural system designed by Zaccaria et al. (2011), but now obtained without the use of rollers or other mechanical devices.

5.5.1 Finite element simulations

Two-dimensional plane-stress finite element simulations have been performed with Abaqus to validate the model of a sliding interface between two soft materials against the experimental results presented in the previous section.

The geometry is shown in the inset of Fig. 5.11 and consists in a rectangular block of edges $B = 10$ mm and $L = \{210, 180, 150\}$ mm. The lower edge of the elastic block is clamped, whereas the upper edge is in contact with a rigid plane which can freely rotate and is connected to an elastic spring which models the stiffness of the suction cup. Contact conditions at the interface between the elastic block and the rigid plane (shown as a red line in the inset of Fig. 5.11) are prescribed such that a bilateral and frictionless interaction is realized. An initial imperfection has been introduced, that consists in a rotation of the rigid plane by an angle of 0.5°. The rigid plane is modelled using a two-dimensional 2-node rigid element (R2D2), while the rectangular block is modelled using 4-node bilinear elements with reduced integration and hourglass control (CPS4R element in Abaqus). The material of the elastic block is a neo-Hookean hyperelastic material characterized by a shear modulus $\mu_0 = 7$ MPa. The spring describing the suction cup is a linear elastic spring with stiffness $k_s = 4.25$ MPa. Displacement boundary conditions (vertical displacement $\delta = 15$ mm) are prescribed at the upper end of the elastic spring.

The results of the finite element simulations are shown in Fig. 5.11 as solid lines with markers. It is shown that the finite element model is able to predict correctly the post-critical behaviour. The peak load is not predicted by the model because the effects of the lubricant at the interface (which produces an increase of the load before buckling) are not taken into account.

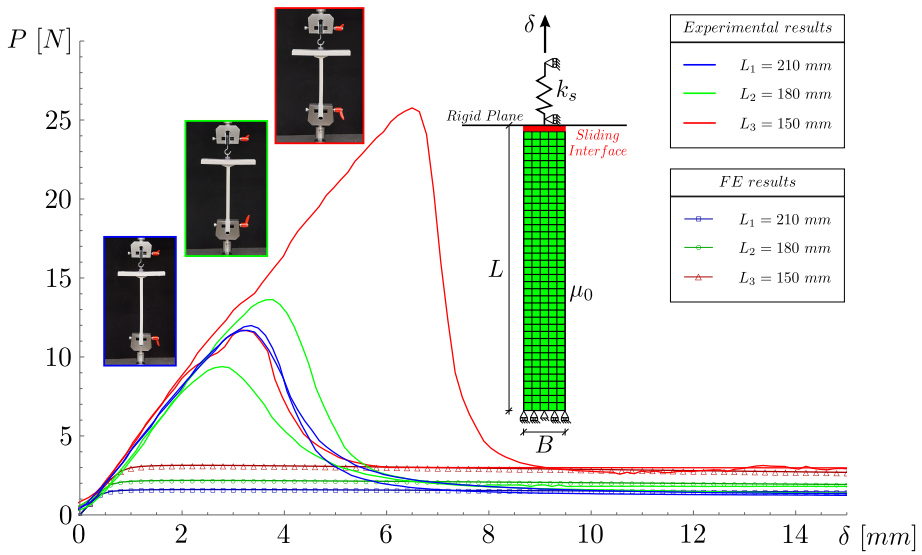

Figure 5.11: Experimental and simulated load–displacement curves of the structure sketched in the inset for three different lengths of the vertical stem, $L_1 = 210$ mm (red lines), $L_2 = 180$ mm (green lines) and $L_3 = 150$ mm (blue lines). The model of sliding interface correctly captures the post-critical behaviour, where the lubricated contact realized a low friction sliding condition.

Appendices

5.A An example of a finite kinematics involving a sliding interface

To clarify the conditions imposed on the kinematics of finite frictionless sliding between deformable bodies in contact, a simple illustration is provided below. The two bodies in contact (identified with '+' and '−') are assumed to be compressible and subject to a large strain of bending and sliding defined by the motion

$$g_\alpha^\pm = \sqrt{\frac{r_e^{\pm 2} - r_i^{\pm 2}}{h_0^\pm} x_1 + \frac{r_e^{-2} + r_i^{-2}}{2}} \cos\left(\frac{\theta_+^\pm - \theta_-^\pm}{l_0^\pm} x_2 + \frac{\theta_+^\pm + \theta_-^\pm}{2} + \frac{\pi}{2}\delta_{\alpha 2}\right) - \left(\frac{l_0^-}{2\theta_+^-} + \frac{h_0^-}{2}\right)\delta_{\alpha 1}, \quad (5.64)$$

$$g_3^\pm = x_3 \quad (5.65)$$

where:

$$\theta_+^- (t) = \theta_+^{f^-} t, \quad (5.66a)$$

$$\theta_-^- (t) = -\theta_+^{f^-} t + t^2 \left(\theta_-^{f^-} + \theta_+^{f^-}\right), \quad (5.66b)$$

$$r_i^- (t) = \frac{l_0^-}{2\theta_+^{f^-} t} + t\left(r_i^{f^-} - \frac{l_0^-}{2\theta_+^{f^-}}\right), \quad (5.66c)$$

$$r_e^- (t) = \frac{l_0^-}{2\theta_+^{f^-} t} + h_0^- + t\left(r_e^{f^-} - \frac{l_0^-}{2\theta_+^{f^-}} - h_0^-\right), \quad (5.66d)$$

$$\theta_+^+(t) = \theta_+^{f^+} t \left(\left(1 - \frac{l_0^+ \theta_+^{f^-}}{l_0^- \theta_+^{f^+}} \right) t + \frac{l_0^+ \theta_+^{f^-}}{l_0^- \theta_+^{f^+}} \right), \tag{5.67a}$$

$$\theta_-^+(t) = -\theta_+^{f^+} t \left(\left(1 - \frac{l_0^+ \theta_+^{f^-}}{l_0^- \theta_+^{f^+}} \right) t + \frac{l_0^+ \theta_+^{f^-}}{l_0^- \theta_+^{f^+}} \right) + t^2 \left(\theta_-^{f^+} + \theta_+^{f^+} \right), \tag{5.67b}$$

$$r_i^+(t) = \frac{l_0^-}{2\theta_+^{f^-} t} + t \left(r_i^{f^+} - \frac{l_0^-}{2\theta_+^{f^-}} \right), \tag{5.67c}$$

$$r_e^+(t) = \frac{l_0^-}{2\theta_+^{f^-} t} + h_0^+ + t \left(r_e^{f^+} - \frac{l_0^-}{2\theta_+^{f^-}} - h_0^+ \right), \tag{5.67d}$$

in which the suffix f indicates the value of the parameter in the final configuration and t is a time-like, dimensionless, parameter governing the motion. When $t = 0$ and $t = 1$ the initial and final dimensionless parameters are set in the way shown in Tables 5.A.1 and 5.A.2 to generate the results shown in Fig. 5.A.1, where the reference configuration B_0 at $t = 0$ is reported together with three configurations corresponding to $t = \{0.33, 0.66, 1\}$. It can be observed from the figure that two different points, lying along the sides + and − of the surface in the reference configuration B_0, move toward each other and momentarily coincide at $t = 0.66$, to eventually separate again in the final configuration at $t = 1.00$.

Parameter	h_0^-	l_0^-	$\theta_p^{f^-}$	$\theta_m^{f^-}$	$r_i^{f^-}$	$r_e^{f^-}$
t = 0	1	3	-	-	-	-
t = 1	-	-	$\frac{\pi}{8}$	$-\frac{\pi}{5}$	4	6

Table 5.A.1: Dimensionless parameters defining the initial ($t = 0$) and final ($t = 1$) configurations of the two bodies in contact shown in Fig. 5.A.1.

Parameter	h_0^+	l_0^+	θ_p^{f+}	θ_m^{f+}	r_i^{f+}	r_e^{f+}
$t = 0$	2	5	-	-	-	-
$t = 1$	-	-	$\frac{\pi}{3}$	$-\frac{\pi}{4}$	6	8

Table 5.A.2: Dimensionless parameters defining the initial ($t = 0$) and final ($t = 1$) configurations of the two bodies in contact shown in Fig. 5.A.1.

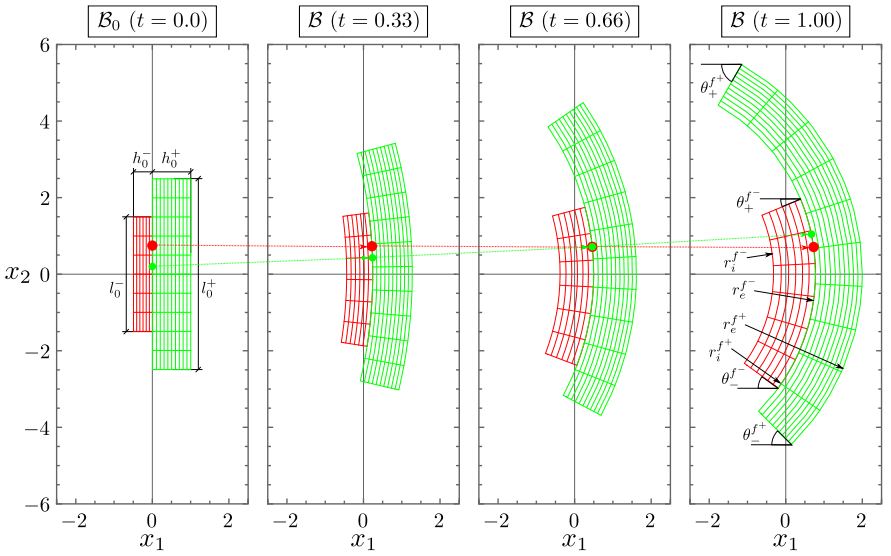

Figure 5.A.1: A series of three deformations at various instants (the time-like, dimensionless, parameter $t = \{0, 0.33, 0.66, 1\}$ is an increasing 'ordering' parameter) showing a finite kinematics involving bending and sliding of two blocks jointed through a sliding bilateral interface. Two points located on the sliding interface but belonging to different blocks, marked red and green, are shown in the reference configuration B_0. These points change the relative position, so that they momentarily coincide in the third sketch from the left. The deformation $g_\alpha^\pm : \mathcal{B}_0 \to \mathcal{B}$ is given by equations (5.64) and (5.65) .

5.B An exclusion condition for bifurcation of two solids in contact with a sliding interface

Following the Hill (1957) generalization of the Kirchhoff proof of uniqueness of the linear theory of elasticity, two incremental solutions are postulated, for the problem sketched in Fig. 5.B.1, $\dot{\boldsymbol{x}}_\alpha^\pm$, $\dot{\boldsymbol{S}}_\alpha^\pm$ (with $\alpha = 1, 2$), so

that the difference fields $\Delta\dot{\boldsymbol{x}}^{\pm}$, $\Delta\dot{\boldsymbol{S}}^{\pm}$ are in equilibrium with homogeneous boundary conditions and null body forces.

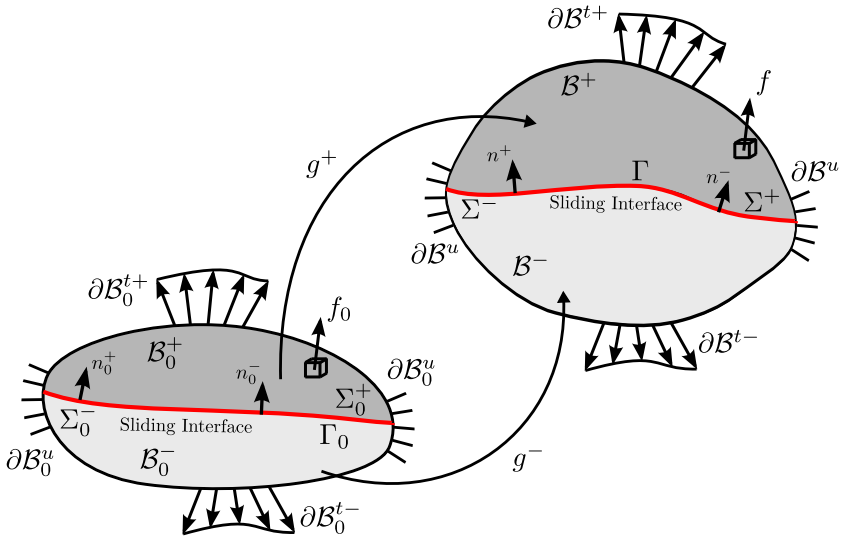

Figure 5.B.1: Deformation of a solid containing a sliding interface. $\mathcal{B}_0$ and $\mathcal{B}$ denote the reference and current configuration, respectively.

Integration of the equilibrium equations for both bodies yields

$$\int_{\mathcal{B}_0^{\pm}} \left(\mathrm{Div}\,\Delta\dot{\boldsymbol{S}}^{\pm}\right)\cdot\Delta\dot{\boldsymbol{x}}^{\pm} = \int_{\mathcal{B}_0^{\pm}} \mathrm{Div}\left(\Delta\dot{\boldsymbol{S}}^{\pm T}\Delta\dot{\boldsymbol{x}}^{\pm}\right) - \int_{\mathcal{B}_0^{\pm}} \Delta\dot{\boldsymbol{S}}^{\pm}\cdot\Delta\dot{\boldsymbol{F}}^{\pm} = 0, \tag{5.68}$$

so that the divergence theorem provides

$$\int_{\mathcal{B}_0^{\pm}} \Delta\dot{\boldsymbol{S}}^{\pm}\cdot\Delta\dot{\boldsymbol{F}}^{\pm} = \mp\int_{\Sigma_0^{\pm}} \Delta\dot{\boldsymbol{x}}^{\pm}\cdot\Delta\dot{\boldsymbol{S}}^{\pm}\boldsymbol{n}_0^{\pm}. \tag{5.69}$$

A sum of the two Eqs. (5.69) yields the following Hill's type exclusion condition for bifurcation

$$\int_{\mathcal{B}_0} \Delta\dot{\boldsymbol{S}}\cdot\Delta\dot{\boldsymbol{F}} > -\int_{\Sigma_0}\left(\Delta\dot{\boldsymbol{x}}^{+}\cdot\Delta\dot{\boldsymbol{S}}^{+}\boldsymbol{n}_0^{+} - \Delta\dot{\boldsymbol{x}}^{-}\cdot\Delta\dot{\boldsymbol{S}}^{-}\boldsymbol{n}_0^{-}\right) \qquad \forall\Delta\dot{\boldsymbol{S}}^{\pm},\Delta\dot{\boldsymbol{x}}^{\pm}. \tag{5.70}$$

Before proceeding with the assumptions employed in the present article, the exclusion condition (5.70) is specialized to the case of the 'spring-type' interface introduced by Suo et al. (1992) and employed also by Bigoni

et al. (1997). This interface is charaterized by: (i.) full continuity of the nominal incremental tractions across the interface and (ii.) a linear interfacial constitutive law of the type

$$\dot{\boldsymbol{S}}^{-}\boldsymbol{n}_0^{-} = \boldsymbol{H}[\![\dot{\boldsymbol{x}}]\!], \tag{5.71}$$

where $\boldsymbol{H}$ is a constitutive tensor (note that in the notation of the present paper and differently form Suo et al. (1992), it is $\boldsymbol{n}_0^{+} = \boldsymbol{n}_0^{-}$). Using the two above conditions (i.) and (ii.) in equation (5.70), the exclusion condition becomes

$$\int_{\mathcal{B}_0} \Delta\dot{\boldsymbol{S}} \cdot \Delta\dot{\boldsymbol{F}} + \int_{\Sigma_0} [\![\Delta\dot{\boldsymbol{x}}]\!] \cdot \boldsymbol{H}[\![\Delta\dot{\boldsymbol{x}}]\!] > 0 \qquad \forall \Delta\dot{\boldsymbol{S}}^{\pm}, \Delta\dot{\boldsymbol{x}}^{\pm}. \tag{5.72}$$

Equation (5.72) shows that for a positive-definite interfacial tensor $\boldsymbol{H}$ (in other words excluding softening interfaces) the term pertaining to the interface is always positive. It may be easily concluded that:

> When the incremental constitutive response of a solid is governed by a positive definite tensor (as for instance for a Mooney–Rivlin material subject to non-negative principal stresses) bifurcation is always excluded for mixed boundary conditions of dead loading and imposed displacements *even in the presence of positive-definite interfaces of the type introduced by Suo et al. (1992).*

For instance, in a case in which all principal stresses are positive or null (as it happens in a tensile problem of the type experimentally investigated in this paper) bifurcations are excluded. In order to substantiate the above statement with an example, consider two elastic blocks made up of Mooney–Rivlin material connected through a planar interface of the type proposed by Suo et al. (1992) without softening. If these blocks will be pulled in tension with a dead loading, the condition (5.72) excludes all possible bifurcations. But the bifurcation will occur in reality, as the T-problem shows. This bifurcation is found if the interface is replaced with a sliding interface of the type described by equations (5.44)–(5.47).

The following assumptions are now introduced:

- a Lagrangean formulation is assumed with the current state taken as reference, so that $\mathcal{B}_0 \equiv \mathcal{B}$ and $\Sigma_0 \equiv \Sigma$;

- plane strain deformation in the plane x_1–x_2 prevails;
- a planar interface is assumed, so that $\boldsymbol{n}_0^+ = \boldsymbol{n}_0^- = \boldsymbol{n}$ and $\boldsymbol{t}_0^+ = \boldsymbol{t}_0^- = \boldsymbol{t}$;
- the material is prestressed by a uniform Cauchy stress with principal components T_{tt} and T_{nn};
- the constitutive equation of the material is incrementally linear

$$\dot{\boldsymbol{S}} = \boldsymbol{\mathcal{E}}[\dot{\boldsymbol{F}}] \quad \text{for compressible material,} \tag{5.73}$$

$$\dot{\boldsymbol{S}} = \boldsymbol{\mathcal{E}}[\dot{\boldsymbol{F}}] + \dot{p}\boldsymbol{I} \quad \text{for incompressible material.} \tag{5.74}$$

Then Eq. (5.70) becomes

$$\int_{\mathcal{B}} \Delta\dot{\boldsymbol{S}} \cdot \Delta\boldsymbol{L} > -\int_{\Sigma} \left(\Delta v_t^+ \Delta\dot{S}_{tn}^+ + \Delta v_n^+ \Delta\dot{S}_{nn}^+ - \Delta v_t^- \Delta\dot{S}_{tn}^- - \Delta v_n^- \Delta\dot{S}_{nn}^- \right), \tag{5.75}$$

where $\boldsymbol{v}$ is the incremental displacement and $\boldsymbol{L}$ its gradient and repeated indices are not summed.

Introducing the fourth-order elastic tensor $\boldsymbol{\mathcal{E}}$ and using Eqs. (5.44) and (5.45), Eq. (5.75) can be rewritten as

$$\int_{\mathcal{B}} \Delta\boldsymbol{L} \cdot \boldsymbol{\mathcal{E}}[\Delta\boldsymbol{L}] > -\int_{\Sigma} \left(\left(\Delta v_t^+ - \Delta v_t^- \right) \Delta\dot{S}_{tn} + \Delta v_n \left(\Delta\dot{S}_{nn}^+ - \Delta\dot{S}_{nn}^- \right) \right). \tag{5.76}$$

Finally, using Eqs. (5.46) and (5.47), the condition for excluding bifurcation in an elastic solid containing a sliding interface becomes

$$\int_{\mathcal{B}} \operatorname{grad} \boldsymbol{v} \cdot \boldsymbol{\mathcal{E}}[\operatorname{grad} \boldsymbol{v}] - \alpha T_{nn} \int_{\Sigma} (v_n [\![v_{t,t}]\!] - [\![v_t]\!] v_{n,t}) > 0, \tag{5.77}$$

holding for all (not identically zero) continuous and piecewise continuously twice differentiable velocity fields $\boldsymbol{v}$ satisfying homogeneous conditions on the part of the boundary where incremental displacements are prescribed and assuming arbitrary values on Σ, but with the normal component satisfying $v_n^+ = v_n^-$.

The parameter α in Eq. (5.77) highlights the difference between the correct interface conditions ($\alpha = 1$) derived in the present work and the incorrect interface conditions ($\alpha = 0$) assumed by Steif (1990).

In the special case in which $T_{nn} = 0$, Eq. (5.77) reduces to the Hill exclusion condition

$$\int_{\mathcal{B}} \operatorname{grad} \boldsymbol{v} \cdot \boldsymbol{\mathcal{E}}[\operatorname{grad} \boldsymbol{v}] > 0, \tag{5.78}$$

showing that for a positive definite incremental elastic tensor $\boldsymbol{\mathcal{E}}$ the incremental solution is unique, whenever the sliding interface is free of normal prestress, otherwise bifurcation is not a-priori excluded. When the incorrect assumption $\alpha = 0$ is made, condition (5.78) is obtained independently of the value of T_{nn}, thus excluding bifurcation for positive definite $\boldsymbol{\mathcal{E}}$. Positive definiteness of $\boldsymbol{\mathcal{E}}$ is equivalent to the requirement that the principal prestresses T_1, T_2, and T_3 (which enter in the definition of $\boldsymbol{\mathcal{E}}$) satisfy all the inequalities $T_1 + T_2 > 0$, $T_1 + T_3 > 0$, $T_2 + T_3 > 0$ or, for uniaxial tension $T_1 > 0$ with $T_2 = T_3 = 0$ (Hill, 1967; Bigoni, 2012).

Chapter 6

Conclusions

Two models for shear band propagation have been described, one in which the shear band is represented through an imperfection embedded in a material and another in which the shear band is viewed as a perturbation which emerges during a homogeneous deformation process of an infinite material. These two models may explain how shear bands tend to propagate rectilinearly under continuous shear loading, a feature not observed for fracture trajectories in brittle materials. In different words, our results substantiate the fact that, while a crack propagates following a maximum tensile stress criterion, a shear band grows according to a maximum Mises stress, a behaviour representing a basic micromechanism of failure for ductile materials. The developed models for shear bands display also a strong stress concentration at the shear band tip, which concurs to shear band growth.

A problem involving sliding interfaces has been addressed by developing a new model for soft solids in sliding contact, an approach of interest in various technologies, exemplified through the design and experimentation on a soft device, which realizes a compliant slider. The derived incremental equations are not trivial and differ from previously (and erroneously) employed interface conditions. A fundamental simplifying assumption in the model is the bilaterality of the contact, which on the other hand is the key to obtain analytical solutions for several bifurcation problems. Some of these solutions have been obtained, which show that: (i.) the interface plays a strong role in the definition of critical conditions, (ii.) the interface promotes tensile bifurcations, one of which has been experimen-

tally verified, which cannot be detected if previously used (and erroneous) interfacial conditions are used.

Bibliography

[1] Abeyaratne, R., Triantafyllidis, N. (1981) On the Emergence of Shear Bands in Plane Strain. *Int. J. Solids Struct.* 17, 1113–1134.

[2] Antipov, YA; Avila-Pozos, O; Kolaczkowski, ST., Movchan A.B. (2001) Mathematical model of delamination cracks on imperfect interfaces *Int. J. Solids Struct.* 38, 6665–6697.

[3] Argani, L., Bigoni, D., Capuani, D. and Movchan, N.V. (2014) Cones of localized shear strain in incompressible elasticity with prestress: Green's function and integral representations Proceedings of the Royal Society A, 470, 20140423.

[4] Argani, L., Bigoni, D. and Mishuris, G. (2013) Dislocations and inclusions in prestressed metals. Proceedings of the Royal Society A, 469, 2154 20120752.

[5] Bacigalupo, A., Gambarotta, L. (2013) A multi-scale strain-localization analysis of a layered strip with debonding interfaces. *Int. J. Solids Struct.* , 50, 2061–2077.

[6] Bigoni, D. (2012) Nonlinear Solid Mechanics Bifurcation Theory and Material Instability. Cambridge University Press, ISBN:9781107025417.

[7] Bigoni, D. and Dal Corso, F. (2008) The unrestrainable growth of a shear band in a prestressed material. Proceedings of the Royal Society A, 464, 2365–2390.

[8] Bigoni, D. and Capuani, D. (2005) Time-harmonic Green's function and boundary integral formulation for incremental nonlinear elasticity: dynamics of wave patterns and shear bands. *J. Mech. Phys. Solids* 53, 1163–1187.

[9] Bigoni, D. and Capuani, D. (2002) Green's function for incremental nonlinear elasticity: shear bands and boundary integral formulation. *J. Mech. Phys. Solids* 50, 471–500.

[10] Bigoni, D., Dal Corso, F. and Gei, M. (2008) The stress concentration near a rigid line inclusion in a prestressed, elastic material. Part II. Implications on shear band nucleation, growth and energy release rate. *J. Mech. Phys. Solids* , 56, 839–857.

[11] Bigoni, D. Serkov, S.K., Movchan, A.B. and Valentini, M. (1998) Asymptotic models of dilute composites with imperfectly bonded inclusions. *Int. J. Solids Struct.* , 35, 3239–3258.

[12] Boulogne, F., Giorgiutti-Dauphine, F., Pauchard, L. (2015) Surface patterns in drying films of silica colloidal dispersions. *Soft matter*, 11, 102.

[13] Ciarletta, P., Destrade, M., Gower, A.L. (2013) Shear instability in skin tissue, *Quart. J .Mech. Appl. Math.*, 66, 273–288.

[14] Dal Corso, F. and Willis, JR. (2011) Stability of strain-gradient plastic materials. *J. Mech. Phys. Solids* , 59, 1251–1267.

[15] Dal Corso, F. and Bigoni, D. (2010) Growth of slip surfaces and line inclusions along shear bands in a softening material. *Int. J. Fracture* , 166, 225–237.

[16] Dal Corso, F. and Bigoni, D. (2009) The interactions between shear bands and rigid lamellar inclusions in a ductile metal matrix. Proceedings of the Royal Society A, 465, 143–163.

[17] Dal Corso, F., Bigoni, D. and Gei, M. (2008) The stress concentration near a rigid line inclusion in a prestressed, elastic material. Part I. Full field solution and asymptotics. *J. Mech. Phys. Solids* , 56, 815–838.

[18] Danas, K., Ponte Castaneda, P. (2012) Influence of the Lode parameter and the stress triaxiality on the failure of elasto-plastic porous materials. *Int. J. Solids Struct.* , 49, 1325–1342.

[19] Destrade, M., Merodio, J. (2011) Compression instabilities of tissues with localized strain softening. *Int. J. Appl. Mech.* , 3, 69–83.

[20] Destrade, M., Gilchrist, M., Prikazchikov, D., Saccomandi, G. (2008) Surface instability of sheared soft tissues. *J. Biomech. Eng., Am. Soc. of Mech. Eng. (ASME)*, 130, 061007.

[21] Gajo, A., Bigoni, D. and Muir Wood, D. (2004) Multiple shear band development and related instabilities in granular materials. *J. Mech. Phys. Solids* , 52, 2683–2724.

[22] Hill, R. (1962) Acceleration waves in solids. J. Mech. Phys. Solids 10, 1–16.

[23] Hutchinson, J.W., Tvergaard, V. (1981) Shear band formation in plane strain. *Int. J. Solids Struct.* 17, 451–470.

[24] Kirby, S.H. (1985) Rock mechanics observations pertinent to the rheology of the continental lithosphere and the localization of strain along shear zones. Tectonophysics, 119, 1–27.

[25] Lapovok, Rimma; Toth, Laszlo S.; Molinari, Alain; Estrina, Y. (2009) Strain localisation patterns under equal-channel angular pressing. *J. Mech. Phys. Solids* , 57, 122–136.

[26] Loret, B., Prevost, J.H. (1991). On the Existence of Solutions in Layered Elasto-(Visco-)Plastic Solids with Negative Hardening. *Eur. J. Mechanics-A/Solids* 10, 575–586.

[27] Loret, B. and Prevost, J.H. (1993). On the Occurrence of Unloading in 1D Elasto- (Visco-)plastic Structures with Softening. *Eur. J. Mechanics-A/Solids* 12, 757–772.

[28] Mandel, J. (1962) Ondes plastiques dans un milieu indéfini à trois dimensions. *J. Mécanique* 1, 3-30.

[29] Merodio, J., Ogden, RW. (2005) On tensile instabilities and ellipticity loss in fiber-reinforced incompressible non-linearly elastic solids. *Mech. Res. Commun.* , 32, 290–299.

[30] Miehe, C., Hofacker, M., Welschinger, F. (2010) A phase field model for rate-independent crack propagation: robust algorithmic implementation based on operator splits, *Comput. Methods Appl. Mech. Eng.* 199, 2765?-2778.

[31] Mishuris, G. (2004) Imperfect transmission conditions for a thin weakly compressible interface. 2D problems. Arch. Mech., 56, 103–115.

[32] Mishuris, G., Ochsner, A. (2005) Transmission conditions for a soft elasto-plastic interphase between two elastic materials. Plane strain state. Arch. Mech., 57, 157–169.

[33] Mishuris, G., Ochsner, A. (2007) 2D modelling of a thin elasto-plastic interphase between two different materials: Plane strain case. Compos. Struct., 80, 361–372.

[34] Mishuris, G. (2001) Interface crack and nonideal interface concept (Mode III). *Int. J. Fracture* , 107, 279–296.

[35] Mishuris, G., Kuhn, G. (2001) Asymptotic behaviour of the elastic solution near the tip of a crack situated at a nonideal interface. *Z. Angew. Math. Mech.* , 81, 811–826.

[36] Mishuris, G., Miszuris, W., Ochsner, A. and Piccolroaz, A. (2013). Transmission conditions for thin elasto-plastic pressure-dependent interphases. In: Plasticity of Pressure-Sensitive Materials. Altenbach, H., Ochsner, A., Eds., Springer-Verlag, Berlin.

[37] Nadai, A. (1950) *Theory of flow and fracture of solids.* McGraw-Hill, New York.

[38] Needleman, A. (1988). Material rate dependence and mesh sensitivity in localization problems. *Comput. Method. Appl. M.* 67 (1), 69–75.

[39] Needleman, A. and Tvergaard, V. (1983) Finite elements: special problems in solid mechanics, vol. V (eds J.T. Oden and G.F. Carey), 94–157.

[40] Peron, H., Laloui, L., Hu, LB., Hueckel, T. (2013) Formation of drying crack patterns in soils: a deterministic approach. *Acta Geotech.* 8, 215–221.

[41] Petryk, H. (1997) Plastic instability: criteria and computational approaches. *Arch. Comput. Meth. Eng.* 4, 111?-151.

[42] Piccolroaz, A., Bigoni, D. and Willis, J.R. (2006) A dynamical interpretation of flutter instability in a continuous medium. *J. Mech. Phys. Solids* 54, 2391–2417.

[43] Puzrin, A. M. and Germanovich, L.N. (2005) The growth of shear bands in the catastrophic failure of soils. *Proc. R. Soc. A* 461, 1199–1228.

[44] Rice, J.R. (1973) The initiation and growth of shear bands. In Plasticity and soil mechanics (ed. A. C. Palmer), p. 263. Cambridge, UK: Cambridge University Engineering Department.

[45] Rice, J.R. (1977) The localization of plastic deformation. In Koiter, W.T., ed., Theoretical and Applied Mechanics. Amsterdam, North-Holland, 207.

[46] Sonato, M., Piccolroaz, A., Miszuris, W. and Mishuris, G. (2015) General transmission conditions for thin elasto-plastic pressure-dependent interphase between dissimilar materials. arXiv:1501.02919 [cond-mat.mtrl-sci].

[47] Prager, W. (1954) Discontinuous fields of plastic stress and flow. In *2nd Nat. Congr. Appl. Mech.*, Ann Arbor, Michigan, 21-32.

[48] Thomas, T.Y. (1961) *Plastic flows and fracture of solids*. Academic Press, New York.

[49] Tvergaard, V. (2014) Bifurcation into a localized mode from non-uniform periodic deformations around a periodic pattern of voids. *J. Mech. Phys. Solids* 69, 112–122.

[50] Yang, B., Morrison, M.L., Liaw, P.K., Buchanan, R.A., Wang, G., Liu C.T. and Denda, M. (2005) Dynamic evolution of nanoscale shear bands in a bulk-metallic glass. *Applied Phys. Letters* 86, 141904.

[51] Zheng, GP., Li, M. (2009) Mesoscopic theory of shear banding and crack propagation in metallic glasses. *Phys. Rev. B* 80, 104201.

[52] Ateshian, G.A., 2009. The role of interstitial fluid pressurization in articular cartilage lubrication. J. Biomech. 42, 1163?1176.

[53] Bigoni, D., 2012. Nonlinear Solid Mechanics. Cambridge University Press, New York.

[54] Bigoni, D. and Gei, M., 2001. Bifurcations of a coated, elastic cylinder. Int. J. Solids Struct., 38, 5117-5148.

[55] Bigoni, D., Ortiz, M. and Needleman, A., 1997. Effect of interfacial compliance on bifurcation of a layer bonded to a substrate. J. Mech. Phys. Solids 34, 4305-4326.

[56] Ciarletta, P. and Destrade, M. 2014. Torsion instability of soft solid cylinders. IMA J. Appl. Math. 79, 804-819.

[57] Cristescu, N.D., Craciun, E.M. and Soos, E., 2004. Mechanics of elastic composites. Boca Raton. Chapman & Hall/CRC.

[58] deBotton, G., Bustamante, R. and Dorfmann, A. 2013. Axisymmetric bifurcations of thick spherical shells under inflation and compression. *Int. J. Solids Struct.* 50, 403-413.

[59] Destrade, M., Fu, Y. and Nobili, A. 2016. Edge wrinkling in elastically supported pre-stressed incompressible isotropic plates. Proc. Royal Soc. A 472, 20160410.

[60] Destrade, M. and Merodio, J. 2011. Compression instabilities of tissues with localized strain softening. Int. J. Applied Mechanics 3, 69-83.

[61] De Tommasi, D., Puglisi, G., Saccomandi, G. and Zurlo, G. 2010. Pull-in and wrinkling instabilities of electroactive dielectric actuators. J. Physics D 43, 325501.

[62] Dowaikh, M.A. and Ogden, R.W., 1991. Interfacial waves and deformations in prestressed elastic media. Proc. Roy. Soc. A 433, 313-328.

[63] Dowson, D., 2012. Bio-tribology. Faraday Discuss. 156, 9-30.

[64] Dunn, A.C., Tichy, J.A., Uruena, J.M. and Sawyer, W.G., 2013. Lubrication regimes in contact lens wear during a blink. Tribol. Int. 63, 45-50.

[65] Fu, Y.B. and Cai, Z.X. 2015. An asymptotic analysis of the period-doubling secondary bifurcation in a film/substrate bilayer. SIAM J. Appl. Math. 75, 2381-2395.

[66] Fu, Y.B. and Ciarletta, P. 2015. Buckling of a coated elastic half-space when the coating and substrate have similar material properties Proc. Royal Soc. A 471, 20140979.

[67] Hill, R., 1957. On uniqueness and stability in the theory of finite elastic strain. J. Mech. Phys. Solids 5, 229-241.

[68] Hill, R., 1967. Eigenmodal deformations in elastic/plastic continua. J. Mech. Phys. Solids 15, 371-386.

[69] Korelc, J., 2009. Automation of primal and sensitivity analysis of transient coupled problems. Comput. Mech. 44, 631-649.

[70] Leroy, Y.M. and Triantafyllidis, N., 1996. Stability of a frictional, cohesive layer on a viscous substratum: variational formulation and asymptotic solution. J. Geophys. Res. 101, B8 795-811.

[71] Liang, X. and Cai, S. (2015) Gravity induced crease-to-wrinkle transition in soft materials. Appli. Phys. Letters 106, 041907.

[72] Ottenio, M., Destrade, M. and Ogden, R.W., 2007. Acoustic waves at the interface of a pre-stressed incomplessible elastic solid and a viscous fluid. Int. J. Non-linear Mech. 42, 310-320.

[73] Riccobelli, D. and Ciarletta, P. 2017. Rayleigh-Taylor instability in soft elastic layers. Phil. Trans. Royal Soc. A 375, 20160421.

[74] Steif, P.S., 1990. Interfacial instabilities in an unbonded layered solid. Int. J. Solids Struct. 26, 915-925.

[75] Steigmann, D.J. and Ogden, R.W. 2014. Classical plate buckling theory as the small-thickness limit of three-dimensional incremental elasticity. ZAMM 94, 7-20.

[76] Stupkiewicz, S. and Marciniszyn, A., 2009. Elastohydrodynamic lubrication and finite configuration changes in reciprocating elastomeric seals. Tribol. Int. 42, 615-627.

[77] Suo, Z., Ortiz, M. and Needleman, A., 1992. Stability of solids with interfaces. J. Mech. Phys. Solids 40, 613-640.

[78] Temizer, I. and Stupkiewicz, S., 2016. Formulation of the Reynolds equation on a time-dependent lubrication surface. Proc. Roy. Soc. A. 472, 20160032.

[79] Tsuchida, E., Mura, T. and Dundurs, J., 1986. The elastic field of an elliptic inclusion with a slipping interface. J. Appl. Mech. 53, 103-107.

[80] Wriggers, P., 2006. Computational Contact Mechanics. Springer-Verlag, Berlin Heidelberg.

[81] Zaccaria, D., Bigoni, D., Noselli, G. and Misseroni, D., 2011. Structures buckling under tensile dead load. Proc. Roy. Soc. A. 467, 1686-1700.

Nicola Bordignon - Born in Marostica (VI) in 1988, he graduated from the University of Trento at the Department of Civil, Environmental and Mechanical Engineering in Structural Civil Engineering in 2014. He then started a Ph.D. at the University of Trento, focusing on the instability phenomenon of mechanical systems.